A Microfluidic Reactor for Time and Spatially Resolved *in situ* Spectroscopic Studies on Nanoparticles During Synthesis

zur Erlangung des akademischen Grades eines

DOKTORS DER NATURWISSENSCHAFTEN
(Dr. rer. nat.)

der Fakultät für Chemie und Biowissenschaften
des Karlsruher Instituts für Technologie (KIT)

genehmigte

DISSERTATION

von

M. Sc. Ghazal Tofighi

aus Teheran, Iran

Dekan: Prof. Dr. Reinhard Fischer
Referent: Prof. Dr. Jan-Dierk Grunwaldt
Korreferent: PD Dr. Silke Behrens
Tag der mündlichen Prüfung: 11.12.2017

Dedicated to my parents and family.

And if whatever trees upon the earth were pens and the sea [was ink], replenished thereafter by seven [more] seas, the words of Allah would not be exhausted. Indeed, Allah is Exalted in Might and Wise.

(Holy Quran: Luqman, verse 27)

Abstract

The vast majority of production processes in chemical industry is based on catalysts, providing energetically favorable mechanisms with high activity and selectivity towards the desired products. Besides their commercial relevance for efficient production and economic profit, catalysts are of vital importance for a more environmentally friendly, sustainable economy (green technology), for example by preventing the production of hazardous byproducts, transforming toxic reaction products into less harmful compounds (e.g. in exhaust gas catalysis) or by transforming energy from renewable sources into chemical energy.

The design of nanoparticles has played an important role in improving the performance of catalysts. A high fraction of atoms in these systems are located at the interfaces or on the particle surfaces leading to high surface to volume ratios. Due to the large surface areas and interfaces, these structures are out of equilibrium and considered thermodynamically unstable. Compared to bulk materials, nanoparticles exhibit unique chemical, physical, magnetic and electronic properties, opening new windows to the world of materials engineering, which is essential for achieving superior performance in many applications, for example in gas sensing and especially in catalysis. Within this regard, understanding the kinetics and mechanisms of nucleation and growth of monodisperse nanoparticles during formation is crucial to optimize their morphology and structure, and for obtaining unique tailored properties. Advanced characterization techniques, especially spectroscopic methods, are powerful tools to explore such phenomena.

This thesis reports on a series of studies using a novel home-built microfluidic setup providing high and pulsation-free flow rates of reactants to synthesize advanced nanostructured materials and study their formation in a continuous turbulent flow (Reynolds number of about 2400). A microfluidic chip designed for this purpose consists of three cyclone micromixers allowing for homogeneous mixing of the reactants in a very short time (< 2 ms at flow rate 2.6 L h^{-1}) for fast reduction reactions, followed by a meandering channel. The setup enables X-ray based *in situ* characterization of the particles during flow synthesis, giving access to information about the kinetics and mechanisms of the reactions. The microfluidic reactor provides plug flow conditions for precise correlation of reaction time and X-ray beam position along the microchannel to enhance time resolution. In this context, the cyclone micromixers play an essential role by reducing the

dead time, i.e. the time required for homogeneous mixing of reactants, to approximately 2 ms. Thus, the combination of advanced micro-process engineering and spectroscopic cell design gives the opportunity to observe the reduction reaction kinetics at previously unavailable time resolution. As a case study within this thesis, the early reaction stages (2-20 ms) of ultrasmall Au nanoparticle formation from Au (III) in the presence of a strong reducing agent ($NaBH_4$) and surfactant (polyvinylpyrrolidone) were monitored *in situ* by synchrotron based X-ray absorption spectroscopy (XAS) at high flow rates of reactants approaching turbulent mixing conditions.

Ultrasmall gold, palladium and homogeneous AuPd alloy nanoparticles with ~ 1 nm average diameter and a very narrow size distribution were synthesized using $NaBH_4$ as reducing agent and polyvinylpyrrolidone (PVP) as surfactant. These nanoparticles in colloidal solutions, and also supported on titania, were characterized by various bulk and surface-sensitive characterization techniques including UV-vis spectroscopy, electron microscopy, energy-dispersive X-ray spectroscopy (EDX), X-ray-absorption near edge spectroscopy (XANES), extended X-ray absorption fine structure (EXAFS), X-ray diffraction (XRD), X-ray photoelectron spectroscopy (XPS) and ultra-high vacuum Fourier transform infrared spectroscopy (UHV-FTIR). The results revealed a remarkable influence of the molar Au:Pd ratio on the crystallographic and electronic structures of AuPd nanoalloys. The size of the particles increased during immobilization. Nevertheless, the produced nanomaterials which were tested in catalytic (CO oxidation) and gas sensing applications show high potential both in sensing and catalysis.

The potential of the microfluidic reactor was finally evaluated in a co-precipitation reaction. $CuO/ZnO/Al_2O_3$ catalysts synthesized in the microfluidic reactor and in a batch reactor were compared. The preparation in the microreactor resulted in $CuO/ZnO/Al_2O_3$ NPs with smaller nanoparticle sizes, thus higher surface-to-volume ratio and more uniform distribution of Cu/Zn in the nanoparticles compared to the material synthesized using a conventional stirred batch reactor. In the future, the microreactor can be used to investigate precipitation reactions using X-ray techniques such as XAS, small angle X-ray scattering and XRD.

Kurzfassung

Der weitaus überwiegende Teil der Produktionsprozesse in der chemischen Industrie läuft in Gegenwart von Katalysatoren ab, die Geschwindigkeiten und Selektivität der beteiligten Reaktionen erheblich beeinflussen. Neben ihrer großen Bedeutung für Produktionseffizienz und ökonomischen Profit spielen Katalysatoren eine entscheidende Rolle beim Übergang zu einer umweltfreundlicheren, nachhaltigeren Wirtschaft, indem sie z. B. die Freisetzung gesundheits- und umweltschädlicher Nebenprodukte vermindern, die Umwandlung giftiger Substanzen in weniger gefährliche Verbindungen vorantreiben (z.B. in der Abgaskatalyse) oder die Speicherung elektrischer Energie aus erneuerbaren Quellen in Form von chemischer Energie ermöglichen.

Nanopartikel und deren Präparation spielen in vielen heterogen-katalysierten Prozessen eine Schlüsselrolle. Ein großer Anteil der Atome in diesen Systemen befindet sich an Grenzflächen oder auf Oberflächen, entsprechend hoch ist das Oberflächen-Volumen-Verhältnis. Aufgrund der großen Oberflächen und ausgeprägten Grenzflächen (z.B. Nanopartikel/Support) befinden sich diese Strukturen nicht im Gleichgewichtszustand und gelten als thermodynamisch instabil. Ihre Eigenschaften unterscheiden sich signifikant von denen der Bulkmaterialien. Nanopartikel zeigen einzigartige chemische, physikalische, magnetische und elektronische Eigenschaften, die im Bereich der Materialforschung neue Perspektiven eröffnen und zu bemerkenswerten Fortschritten beim Design von Funktionsmaterialien für diverse Anwendungen beitragen, neben Katalyse z. B. auch in der chemischen Sensorik. In diesem Zusammenhang ist ein tiefgreifendes Verständnis der für Keimbildung und Wachstum monodisperser Nanopartikel maßgeblichen Kinetik und Reaktionsmechanismen von entscheidender Bedeutung für eine Optimierung von Morphologie und Struktur und maßgeschneiderte Eigenschaften. Moderne Charakterisierungsmethoden, insbesondere spektroskopische Techniken, leisten dazu entscheidende Beiträge.

Für die im Rahmen dieser Dissertation durchgeführten experimentellen Studien wurde eine Mikrofluidik-Apparatur aufgebaut, die speziell auf kolloidale Synthese nanostrukturierter Materialien bei pulsationsfreier Dosierung von Reaktanden und hohen Durchflussraten in kontinuierlicher turbulenter Strömung (Reynolds-Zahl von etwa 2400) ausgelegt ist. Drei in den Mikrofluidik-Chip integrierte Zyklonmischer ermöglichen homogenes Mischen der Reaktanden in kurzer Zeit (< 2 ms bei einem Durchfluss von 2.6 L h^{-1}) für schnelle

Reduktionsprozesse, gefolgt von einem Mäanderkanal. Der Mikrofluidik-Aufbau ermöglicht darüber hinaus eine Röntgen-basierte Charakterisierung der Partikel während der Synthese und damit unmittelbaren Zugang zu Informationen bzgl. der maßgeblichen Reaktionsmechanismen und Kinetik. Im Mikrofluidikreaktor herrscht eine ideale Strömung vor, um die seit Beginn der Reaktion verstrichene Zeit mit der Position des Röntgenstrahls entlang des Mikrokanals mit hoher zeitlicher Auflösung direkt korrelieren zu können. Die Zyklonmischer im Mikrofluidik-Chip reduzieren hierbei die Totzeit, d.h. die für homogenes Mischen der Reaktanden erforderliche Zeit, auf 2 ms. Das Zusammenwirken von Mikroverfahrenstechnik und *In-Situ*-XAS-Messzellendesign ermöglicht so eine Untersuchung der Reaktionskinetik mit bislang nicht verfügbarer zeitlicher Auflösung. Als Fallstudie im Rahmen dieser Arbeit wurden frühe Reaktionsstadien (2 -20 ms) der Bildung von Gold-Nanopartikeln aus Au(III) in Gegenwart eines starken Reduktionsmittels ($NaBH_4$) und einer oberflächenaktiven Komponente (PVP als Surfactant) *in situ* mittels Röntgenabsorptionsspektroskopie mit Synchrotronlicht bei hohem Reaktandendurchfluss im Bereich turbulenter Mischbedingungen verfolgt.

Gold-, Palladium- und homogene Gold-Palladium-Legierungs-Nanopartikel mit mittleren Durchmessern von ca. 1 nm und schmalen Größenverteilungen wurden in diesem Mikroreaktor mit $NaBH_4$ als Reduktionsmittel und Polyvinylpyrrolidone (PVP) als oberflächenaktiver Komponente (Surfactant) synthetisiert. Die Struktur dieser Nanopartikel, sowohl in Kolloidlösung als auch geträgert auf Titanoxid, wurde mittels verschiedener volumen- und oberflächenempfindlicher Charakterisierungstechniken wie UV/Vis-Spektroskopie, Elektronenmikroskopie, Energiedispersiver Röntgenspektroskopie (EDX), Röntgenabsorptionsspektroskopie (XAS), Röntgendiffraktion (XRD), Röntgenphotoelektronenspektroskopie (XPS) und Ultrahochvakuum-Fourier-Transform-Infrarotspektrometrie (UHV-FTIR) analysiert. Die Ergebnisse dieser Untersuchungen weisen auf einen bemerkenswerten Einfluss des molaren Au:Pd-Verhältnisses auf die kristallographische und elektronische Struktur der Gold-Palladium-Legierungs-Nanopartikel hin. Die Größe der Partikel nahm während der Aufbringung auf das Trägermaterial zu. Gleichwohl zeigten die hergestellten Nanomaterialien bei Aktivitätsmessungen ein hohes Potential als Katalysatoren für die CO-Oxidation und im Hinblick auf Anwendungen in der chemischen Sensorik.

Der Mikrofluidikreaktor konnte auch erfolgreich für eine Cofällungsreaktion genutzt werden. Ein Vergleich von mikrofluidisch und in einem diskontinuierlichen Rührreaktor

(Batch-Reaktor) synthetisierten $CuO/ZnO/Al_2O_3$–Katalysatoren zeigte, dass die im Mikrofluidikreaktor hergestellten Materialien kleinere mittlere Partikeldurchmesser, entsprechend größere spezifische Oberflächen und eine gleichmäßigere Verteilung von Cu und Zn in den Partikeln aufwiesen. Zukünftig kann der Mikrofluidikreaktor auch zur Untersuchung von Präzipitationsreaktionen mittels röntgenbasierter Methoden wie XAS, Röntgenkleinwinkelstreuung und Röntgendiffraktion genutzt werden.

Contents

List of Figures

List of Tables

List of Abbreviations

ANKA	Angströmquelle Karlsruhe (synchrotron light source in Karlsruhe)
BET	Brunauer–Emmett–Teller
BMBF	Bundesministerium für Bildung und Forschung (Federal Ministry of Education and Research)
CFD	Computational Fluid Dynamics
CN	Coordination Number
DESY	Deutsches Elektronen Synchrotron (synchrotron radiation facility in Hamburg)
EDX	Energy Dispersive X-ray Spectroscopy
EXAFS	Extended X-ray Absorption Fine Structure
FT	Fourier Transform
GHSV	Gas Hourly Space Velocity
HAADF	High Angle Annular Dark-Field
HC	Hydroxycarbonate
HERFD-XAS	High-Energy-Resolution Fluorescence Detected X-ray Absorption Spectroscopy
HRTEM	High Resolution Transmission Electron Microscopy
ICP-OES	Inductively Coupled Plasma-Optical Emission Spectrometry
IFG	Institute of Functional Interfaces (KIT)
IHM	Institute of Semiconductors and Microsystems (TUD)
IKFT	Institute of Catalysis Research and Technology (KIT)
INT	Institute for Nanotechnology (KIT)
IMVT	Institute for Micro Process Engineering (KIT)
IRRAS	Infrared Reflection-Absorption Spectroscopy
ITCP	Institute for Chemical Technology and Polymer Chemistry (KIT)
KIT	Karlsruhe Institute of Technology
KNMF	Karlsruhe Nano Micro Facility
MISR	Microimpinging Stream Reactor

MOS	Metal Oxide Semiconductor
MS	Mass Spectrometer
NC	Nanocrystal
NP	Nanoparticle
PVP	Polyvinylpyrrolidone
SA	Surface Area
SAXS	Small Angle X-ray Scattering
SLS	Swiss Light Source (synchrotron radiation source)
SNR	Signal to Noise Ratio
SPR	Surface Plasmon Resonance
STEM	Scanning Transmission Electron Microscopy
TBAB	Tetrabutylammonium Borohydride
TCD	Thermal Conductivity Detector
TEM	Transmission Electron Microscopy
THPC	Tetrakis (Hydroxymethyl) Phosphonium Chloride
TG	Thermogravimetry
TOF	Turnover Frequency
TPR	Temperature-Programmed Reduction
TUD	Technische Universität Dresden
UHV-FTIR	Ultra-High Vacuum-Fourier-Transform Infrared
UV-vis	Ultraviolet and Visible light
VOC	Volatile Organic Compound
WGS	Water-Gas Shift
Wt.%	Weight percent
XANES	X-ray Absorption Near-Edge Structure
XAS	X-ray Absorption Spectroscopy
XPS	X-ray Photoemission Spectroscopy
XRD	X-Ray Diffraction

1. Introduction

1.1. Nanoparticles for Catalysis

Catalysts are essential in the production of bulk/fine chemicals, fuels and for chemical transformations in the industry as well as in automotive and stationary exhaust gas after treatment systems to decrease emission of pollutants. In the chemical industry catalytic processes are responsible for about 85-90% of the products. Catalysts accelerate chemical reactions (in some cases make them even possible) by providing energetically favorable alternative reaction pathways with significantly lower activation energy compared to uncatalyzed reactions. Catalysis research is a vast and highly multi-disciplinary field, challenging scientists and engineers[1].

For highly efficient catalysts, a high number of active sites and for heterogeneous catalysts a large surface area are beneficial. This can be achieved by using nanoparticles (NPs) which exhibit unique physical and chemical properties different from the corresponding bulk materials due to lower coordinated atoms on the surface with altered physical and electronic properties and due to quantum confinement effects. In this context, heterogeneous catalysis offers unprecedented opportunities to improve the catalytic activity and selectivity compared to (quasi-)homogeneous catalysis, especially considering the fact that the recovery of metal NPs after heterogeneous catalytic tests is possible and agglomeration can be drastically reduced. For catalytic applications, metal NPs are immobilized on a solid support and/or isolated by using porous support materials. The latter can potentially reduce or prevent sintering of the NPs at high temperatures. For preparation of supported NPs various techniques such as impregnation, co-precipitation, deposition-precipitation, adsorption of colloids, sol immobilization and physical vapor deposition have been used[1-7]. In some cases supported nanoparticles showed activity and selectivity for specific reactions for which the corresponding unsupported NPs were not considered active before, e.g. for a long time, gold was considered the noblest metal and not anticipated to exhibit significant catalytic activity[8-11]. However, in the early 1990s Haruta et al.[2, 12, 13] demonstrated that supported Au nanoparticles (1-5 nm) are active for low temperature CO oxidation (role of metal support interface and small metal NP size) and also for propene oxidation from propene, oxygen and hydrogen. Since then, application of gold nanoparticles in catalysis has been a hot topic with respect to many reactions such as water-gas shift (WGS), reduction of nitrogen oxides, oxidation of alcohols, H_2O_2 synthesis,

selective hydrogenation of alkenes, etc[9, 14-17]. Therefore, the optimization of NP preparation and adsorption on supports are a promising approach.

A greater variety of catalytic properties can be achieved by mixing different metals to create intermetallic compounds and nanoalloys. In many cases synergistic effects lead to improved performance of the catalysts upon alloying, and the multitude of possible alloys with different compositions, structures and properties provides many degrees of freedom to tailor bimetallic or trimetallic catalysts for specific applications. The homogeneity of the alloyed structure or the degree of segregation depends very much on the synthesis method, and conditions applied e.g. precursor, temperature, pressure, etc and also the nanoalloy composition. In principle, various mixing patterns are possible such as core-shell, segregated subcluster, mixed and multi shell structures (more details in chapter 4 and 5)[18].

Colloidal chemistry is an interdisciplinary field, allowing synthesis of NPs with specific physical and chemical properties deriving from the particle size (1-100 nm) and shape. The colloidal approach allows synthesis of 'Ultrasmall NPs' which is a widely used term in the materials science community, referring to NPs with 1-3 nm core size, bridging the gap between single molecules and classical larger sized NPs, with 70% of the atoms located on the surface and physiochemical properties uniquely differing from the corresponding bulk materials[19-21].

There are two main approaches to synthesize metal NPs: physical or "top down" methods by mechanically crushing metallic aggregates in the bulk state to smaller particles, and chemical or "bottom up" methods via nucleation and successive growth of NPs from the precursors and individual molecules in which a chemical or biological reduction occurs. However, the top down method is limited regarding the control of particle size, shape and further functionalization of the surface and therefore leads to poor synthesis reproducibility. Such drawbacks are compensated in the case of the bottom up method[5, 22]. The main chemical routes are (1) chemical reduction; (2) thermal, photochemical, or sonochemical decomposition; (3) ligand reduction and displacement from organometallics; (4) metal vapor synthesis and (5) electrochemical reduction[5]. The most common method among these techniques is chemical reduction, resulting in narrow size distributions, higher production yield (multigram) and reproducibility[23, 24]. This method is described in more detail in chapter 3 of this thesis. After the reduction of metal ions the formed nuclei join together to form clusters which, after reaching a critical amount, can grow due to the autocatalytic

reaction occurring on their surfaces until all free atoms/nuclei in the solution are consumed. Some nuclei can still dissolve and join the already existing NPs resulting in larger particles and broader size distributions (Ostwald ripening). The Brownian motion and Van der Waals forces trigger growth processes and further coagulation[25]. Hence, colloidal metal NPs should be kept well dispersed in water (hydrosols) or organic solvents (organosols) to prevent agglomeration[23]. This can be achieved by using protecting shells or stabilizers. There are four main mechanisms to stabilize colloidal NPs in the dispersion media and prevent agglomeration: (1) electrostatic stabilization; (2) steric stabilization; (3) electrosteric stabilization; and (4) stabilization by ligand or solvent[5, 25]. In the case of electrostatic stabilization, the stabilizing compounds and their counterions are adsorbed on the metal surface. The double electric layer around the NPs causes the Coulombic forces repelling the particles from each other. This process can occur in halides, carboxylates or polyoxoanions in e.g. Au and Pd colloids synthesized using sodium citrate[26, 27]. During steric stabilization the NPs are covered by bulky layers of materials such as polymers or surfactants. Electrosteric stabilization is a combination of both mechanisms (1) and (2), while stabilization by ligand or solvent introduces stabilization of colloidal transition metal NPs by coordination, using traditional ligands e.g. phosphines, thiols, amines, etc[5]. Some common stabilizers are linear polymers, dendrimers, surfactants, micelles, ligands etc. Polyvinylpyrrolidone (PVP) is one of the most popular polymer stabilizers since it allows to a high degree control of noble metal NP size. A higher PVP concentration leads to better stabilization and smaller NPs[28, 29]. Moreover, the morphology of particles can be tailored by key parameters such as pH, reducing agent, stabilizers, concentrations of reactants, temperature, etc. For example, Au NPs stabilized with PVP are active in aerobic oxidation of benzylic alcohols in such a way that smaller Au NPs show higher catalytic activity[30].

Co-precipitation of two or more metal salts simultaneously from a solution is another popular chemical approach to synthesize catalytically active materials (the support materials can also precipitate during this procedure). In this process, which is described in more detail in chapter 6, hydroxides precipitate in presence of precipitation agents such as NaOH, Na_2CO_3 or $NaHCO_3$ under specific reaction conditions to form a homogeneous mixture, which in the next step is separated, washed and subjected to post-treatments such as drying and calcination[1, 24, 31]. One popular example for co-precipitated products in industry is $Cu/ZnO/Al_2O_3$ (Cu:Zn:Al ~ 60:30:10 composition) for methanol synthesis, containing active Cu NPs dispersed by ZnO and stabilized by Al_2O_3 (nitrates of Cu, Zn and

Al as metal precursors and alkali bicarbonates or alkali carbonates as precipitating agents), where the co-precipitation process results in the formation of various hydroxy carbonates such as aurichalcite, zincian malachite, etc[32-35]. The phase, structure and catalytic properties of the products strongly rely on the synthesis parameters such as the precipitation temperature, the composition of the metal components, pH, ageing time and temperature, stirring rate, etc. Afterwards, calcination of the products leads to nano-structuring and high dispersion of the metal oxide phases[33, 36, 37]. The most efficient catalysts applied for methanol synthesis were reported to be produced under constant pH (6 or 7) with Na_2CO_3 as precipitating agent and at temperatures around 60-70 °C[33, 38]. The ageing time ranged from 30 min to several hours while the calcination procedure was applied at about 326-426 °C[31]. However, it should be noted that the co-precipitation via traditional batch reactors is difficult to control, i.e. good immediate mixing, maintaining a constant pH throughout the solution and achieving a homogeneous crystallization of the two components to precipitate simultaneously are both essential and challenging[1].

Besides conventional stirred batch reactor techniques, microfluidic reactors have attracted attention in recent years as promising tools to synthesize NPs in a highly controlled way in order to tailor particle sizes and achieve narrow size distributions for the desired catalytic properties[39-41]. The size, distribution and shape of NPs and supports play an important role in increasing the surface area and the contact between catalytic sites and reactants, which can lead to tunable physical and chemical properties and hence to high performance catalytic materials[1, 3, 4, 42].

Moreover, the effects of different NP synthesis methods (e.g. different reduction and co-precipitation reactions in batch reactors or different flow conditions in microfluidic reactors) on nanomaterial properties resulting from their structure, phase, morphology, size distribution and interparticle interactions should be closely investigated. Within this regard, understanding and controlling the intermediate processes occurring during synthesis is highly important. This highlights the necessity for *in situ* and *operando* studies and the combination of different spectroscopic or scattering characterization techniques. Suitable *in situ* reaction cells are an essential prerequisite to observe intermediate compounds on-line and investigate the kinetics of the reactions at their early stages with high spatial and time resolution[43-47]. In this context, modified batch reactors combined with peristaltic pumps and stopped-flow reactors have been used to study slow reactions (second to minute range) *in situ* by spectroscopic techniques such as UV-visible spectroscopy, X-ray

absorption spectroscopy (XAS) and small/wide angle X-ray scattering (SAXS/WAXS), while faster reactions (millisecond regime down to 100 ms) were investigated in stopped-flow[46-48] as well as continuous-flow apparatus[45, 49]. Yao et al. determined the initial kinetics of nucleation of Au nanocrystals (NCs) with citric acid as reducing agent and PVP as surfactant by pumping the reactants from a flask into an *in situ* XAS cell in a continuous flow and then back again to the flask (20-60 min) to investigate the complexes formed during the Au reduction in a slow reaction[49]. Abécassis et al. studied nucleation and growth of Au NPs in the presence of different ligands (alkanoic acid and alkylamine) *in situ* by synchrotron SAXS/WAXS and UV-visible spectroscopy and found out that ligands affect the nucleation rate significantly[47].

In the following, the principles of NP synthesis in batch and microfluidic reactors are explained in detail. The fluid mechanical factors relevant for the synthesis as well as different flow types are shortly described. Moreover, selected case studies of recent microfluidic reactors from literature are discussed to show the various designs and capabilities of microfluidic reactors. Since X-ray absorption spectroscopy is one of the main advanced characterization techniques used in this thesis work, the principles of this powerful analytic tool are explained in more detail in section 1.5.

1.2. Microfluidic Reactor vs. Batch Reactor

Due to unique physical and chemical properties, metal NPs have attracted considerable attention for various applications, in which the preparation method play a main role in product properties. From the synthesis method point of view, the production of metal NPs can be categorized into two different methods: the traditional batch reactor and in microfluidic reactor. The disadvantages of using batch reactors are heterogeneous flow and non-efficient mixing conditions, which results in reactants concentration gradient and random nucleation and growth of NPs. Finally, this effect leads to polydispersity in size and shape of NPs and deviations from desired physical and chemical properties. Additionally, batch reactor provides limited control over temperature profiles during synthesis (Fig. 1a)[50, 51].

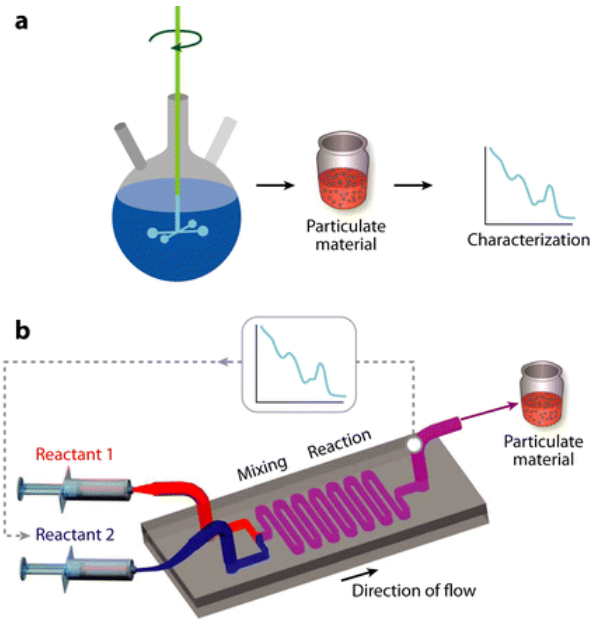

Fig. 1 Materials synthesis technique a) in a conventional batch reactor and b) in a microfluidic reactor (reprinted with permission from reference[50]).

On the other hand, microfluidic is the science and technology of manipulating and controlling fluids with a small volumes (10^{-9}-10^{-18} L) flowing in networks of channels with tens to hundreds micron range dimensions[52]. Production of NPs in such a continuous flow microreactor is a promising method, offering several benefits such as easier process handling, better mixing, higher mass and heat transport and process parameters within a wide range of operating conditions as well as a significant decrease in reagent consumption. Compared to conventional batch processes, this can lead to a narrower size distribution of NPs with a desired particle size and fine-tuning the desired properties (Fig. 1b)[41, 50, 53-55].

1.3. Microfluidic Synthesis of Materials

The flow type and microchannel dimensions also have an effect on properties of NPs. Microfluidic synthesis can be divided into two major groups:

(a) Single phase microfluidic synthesis, i.e. a continuous flow consists of only one phase (Fig. 2a). This type of flow can be laminar or turbulent. In the case of a laminar flow, there is a limited mixing across the channel by diffusion mechanism. Therefore, it is suggested to achieve convective mixing by using micromixers[50].

(b) Multiphase microfluidic synthesis in which the flow is segmented using different phases. The first phase is usually a liquid of miscible reactants. The other phase can consist either of gas/bubbles or liquid which is immiscible with the first phase (Fig.

2b). The reaction might happen inside the phase or at the interface of two phases. The advantages of this system in comparison with single phase flow are effective mixing and fast heat and mass transfer. Moreover, axial dispersion can be decreased or completely eliminated[50]. Furthermore, direct contact of liquid with channel walls can be avoided which leads to no or less clogging of microchannels[56].

(c)

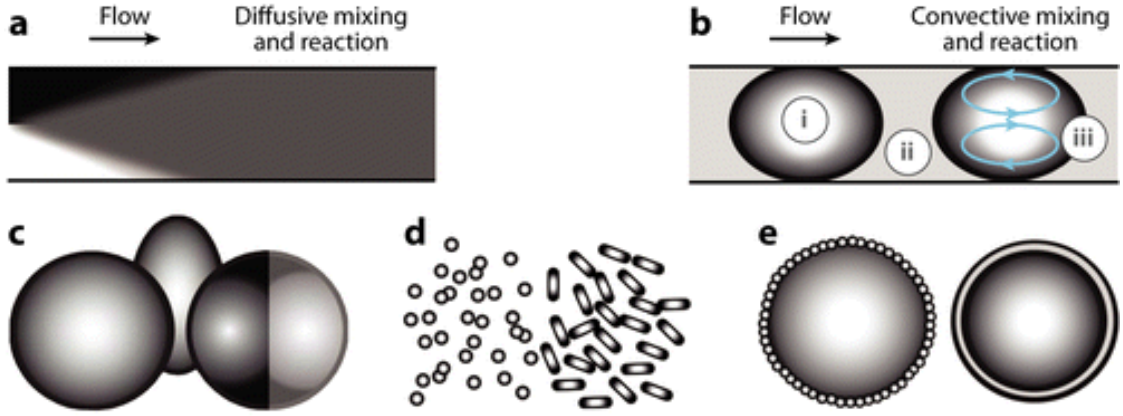

Fig. 2 Microfluidic synthesis of polymer and inorganic particles using a) single-phase and b) multiphase methods, c) in droplets, d) in continuous-phase-separating droplets and e) at the interphase between the two phases (reprinted with permission from reference[50]).

Microfluids are affected by gravitational, interfacial, inertia and viscous forces. The combination of these forces determines the instabilities, dynamics and fluid phase distributions. Under static conditions (when the flow conditions are steady and gravitational acceleration (g) and temperature gradients are insignificant), and in the case of homogeneous pressure distribution in both phases, but with different capillary pressures[56], therefore according to Young-Laplace equation:

$$\Delta p_{cap} = \gamma\, k$$

Where γ is the interfacial tension and k is the local mean curvature at the interface. Such a static fluid interface shows two behaviors with respect to the channel walls; it either makes a contact line between two fluid phases (phase 1, 2 here) and the solid wall (phase s) which is given by (Fig. 3a) or it forms a film which inhibits the contact between one of the fluid phases and the wall (Fig. 3b). In the first situation, the contact angle θ defined according to Young's equation depends on wettability of the matters:

$$\gamma_{12} \cos\theta = \gamma_{1s} - \gamma_{2s}$$

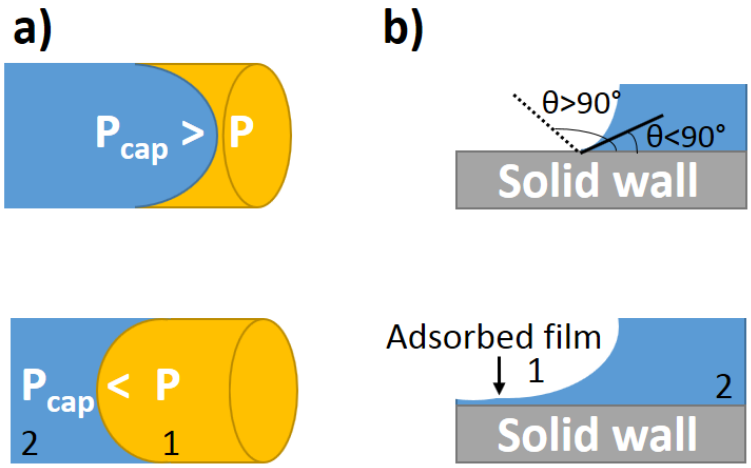

Fig. 3 a) Positive or negative curvature of the air–liquid interface causes positive and negative differences between the capillary pressure (P_{cap}) and ambient pressure (P); b) Local configuration in a three phase region: Top: a contact line between two fluid phases and the solid wall with angle θ, bottom: the fluid phases are separated by an adsorbed film (adapted from reference[56]).

Fluids with small contact angle (near 0°) can wet the surface and are called “wetting liquids” whereas fluids with larger contact angle (near 180°) are called “non wetting liquids”. Chemical modification of the surface properties or differences in surface roughness on the micro or nanoscale, can lead to changes in wetting characteristics. To understand the relations between interfacial and gravitational forces, the Bond number was defined as:

$$B_0 = \frac{(\Delta\rho)\, g\, d_h^2}{\sigma}$$

Where, Δρ is the density difference between the two phases (gas-liquid or liquid-liquid), σ the surface tension measured against a gas phase, and d_h the characteristic channel dimension or the channel hydraulic diameter:

$$d_h = \frac{4A}{\tau}$$

In the latter equation, A is the channel cross sectional area and τ is the wetted perimeter. It is mentioned in the literature that interfacial forces prevail the gravitational forces on the microscale in most cases ($B_0 << 1$). Addition of surfactants or an increase in temperature shifts the band towards higher B_0 values[56].

On the other hand, under flow conditions (dynamic conditions), the characteristic velocity of the dispersed phase U_d needs to be taken into account (Fig. 4). As mentioned before, different flow patterns and phase distributions can be created by the interactions between interfacial, gravitational, viscous and inertia forces in a flowing system, which makes it complicated. Here other parameters in fluid mechanics are defined, which help to understand and predict the flow behavior in microchannel systems. The capillary number (Ca) is defined as the ratio of viscous to surface forces and as the ratio of fluid viscosities:

$$Ca = \frac{\mu U_d}{\sigma} , \frac{\mu}{\hat{\mu}}$$

Where, μ and $\hat{\mu}$ are the viscosities of the continuous and dispersed phases, respectively.

The Weber number is the ratio of inertia to surface forces:

$$We = \frac{\rho \, U_d^2 d_h}{\sigma}$$

In the case of single phase flows, if We and Ca numbers are known, another parameter the so-called Reynolds number which is related to viscous and inertial forces, can be determined[56].

Re = We / Ca

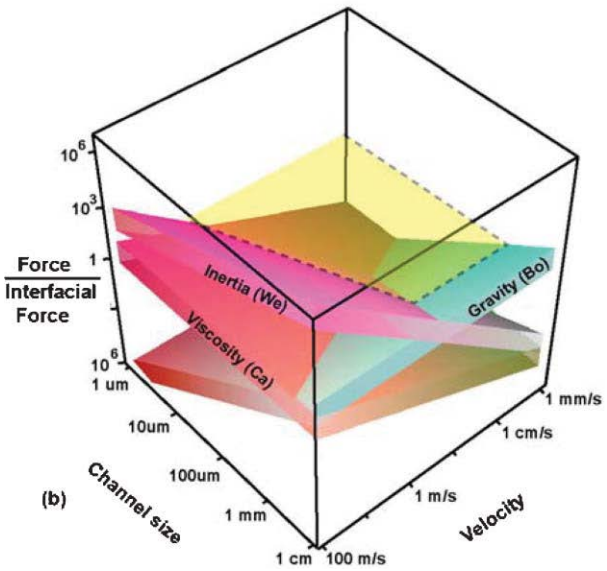

Fig. 4 Effect of inertia, viscous and gravity forces with respect to interfacial forces in multiphase microfluidic systems declared by We, Ca and B_0 numbers. In yellow plane all the forces are in balance, i.e. We = Ca = B_0 = 1 (reprinted with permission from reference[56]).

1.4. A Glance at Microfluidic Reactors for Metallic NP Synthesis

Gold NP synthesis in a microfluidic reactor was pioneered by Wagner et al. in 2004[40]. The microfluidic chip was made of Pyrex glass by wet etching and consisted of two micromixers and a serpentine channel for synthesizing Au NPs using with or without preformed seeds, using different reducing agents (ascorbic acid, sodium borohydride and sodium citrate) and applying different flow rates, pH and concentration ratios of Au precursor to reducing agents[40, 57, 58]. During several studies, the microfluidic chip designs were optimized for different reactions to produce narrow size distributed materials such as metal NPs, polymer particles, semiconductor NPs and core/shell structures with static chip micromixers based on the mechanism of splitting-and-recombination units[50, 58-60]. A schematic drawing of one such microfluidic chip is shown in Fig. 5.

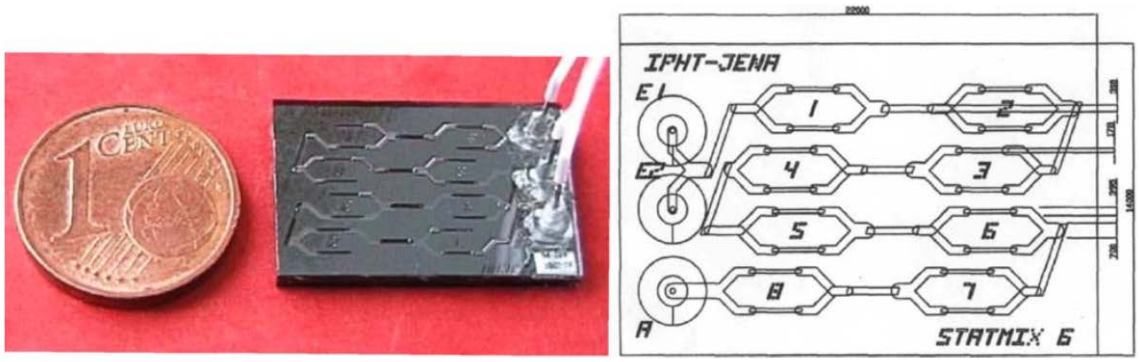

Fig. 5 Optical image and schematic of the static chip micromixer with eight splitting-and-recombination units (reprinted with permission from reference[58]).

For synthesis of Au/Ag core/shell structures, the microfluidic chip was modified with an additional residence loop and a T-junction (Fig. 6 - left). In the first step Au NPs were synthesized with ascorbic acid in a continuous flow and in the next step, the reduction of Ag in the presence of Au NPs was achieved after a specific time using a residence loop attached to the outlet of the chip. It is known that the reduction of Ag ions to form Ag NPs in liquid phase can be catalyzed by noble metal cores which makes the gold NPs a good candidate for synthesizing bimetallic and core-shell structures in microreactors. Moreover, it was shown that the optical and catalytic properties of the colloidal solution strongly depend on the mixing order and flow rate which determines the residence time between mixing units[59].

Fig. 6 (right) schematically shows a microfluidic device operating in a segmented flow. First the aqueous solution of a reducing agent is injected into the stream of an inert carrier liquid (tetradecane) which is immiscible in water. The second injector brings gold precursor solution in contact with the prior reducing agent and then both are well mixed using the shear forces and the induced segment internal convection through the tube coil mixer. Finally, the third injector adds the second metal precursor solution to the produced gold NPs and again mixing is achieved by a tube coil mixer. The same process is repeated for adding the third metal solution in order to prepare double shell compositions like Au/Ag/Au. This method is applied in such a way that all microsegmented volumes of liquid experience equal residence time by a plug flow mechanism in a liquid/liquid two phase system. The flow rate in the range of 5 µL min^{-1} – 5 mL min^{-1} leads to a mean residence time of 12 s and 15 ms in such systems[59].

The Au/Ag core/shell and Au/Ag/Au double shell structures synthesized in such microfluidic setups had average diameters of 20 nm and 46 nm with distribution half widths of 3.8 nm and 7.4 nm, respectively. These NPs showed a narrower size distribution and smaller average NP diameters compared to those synthesized in batch, which is a proof of superiority of microfluidic synthesis to batch techniques[60].

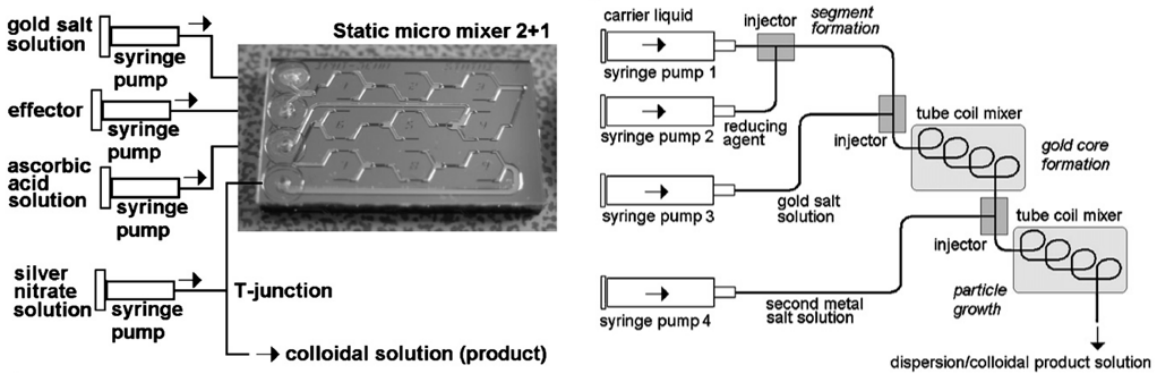

Fig. 6 microfluidic device for NP synthesis: (Left) A two-step mixer, a residence loop and a third mixing unit built by a T-junction (2+1) are used to produce Au/Ag core/shell composition in a continuous flow, (right) modular design of PTFE T-junctions and residence loop for use in a segmented flow regime (reprinted with permission from reference[59]).

A special class of NPs is “ultrasmall NPs” with diameters between 1 and 3 nm, i.e. sizes ranging between free molecules and larger-sized NPs which show unique characteristic properties suitable for various applications. In the case of gold NPs, such nanoclusters with

diameters of ca. 1 nm diameter have attracted growing attention especially from a catalytic point of view. In order to study such ultrasmall metal clusters, achieving narrow size distributions is of paramount importance[20, 51]. Tsunoyama et al. used a SIMM-V2 micromixer to synthesize narrow size distributed ultrasmall gold nanoclusters with diameters of 1 nm which are highly active as catalysts in numerous organic reactions. Sodium borohydride was used as a strong reducing agent and polyvinylpyrrolidone (PVP) for NP stabilization. The microreactor (Fig. 7) consists of 32 parallel channels: 16 substream channels for the $NaBH_4$/PVP solution and 16 for the $HAuCl_4$/PVP solution with thickness of <100 µm laminated in an interdigital arrangement (zone I). Afterwards, the multilamellar flow is compressed into a narrower stream (zone II), and finally Au NPs are collected at the outlet to be stirred for 1 h in an ice bath[29].

The results show that higher flow rates and higher concentration of $AuCl_4^-$ and BH_4^- lead to production of smaller particles. The TEM images showed that the Au NPs synthesized in micromixer had narrower size distribution compared to those produced in a batch reactor. Furthermore, the authors speculated that the microbubbles released during the decomposition of sodium borohydride had influence on the mass transport by promoting the breaking of lamellar configurations into smaller fragments[29].

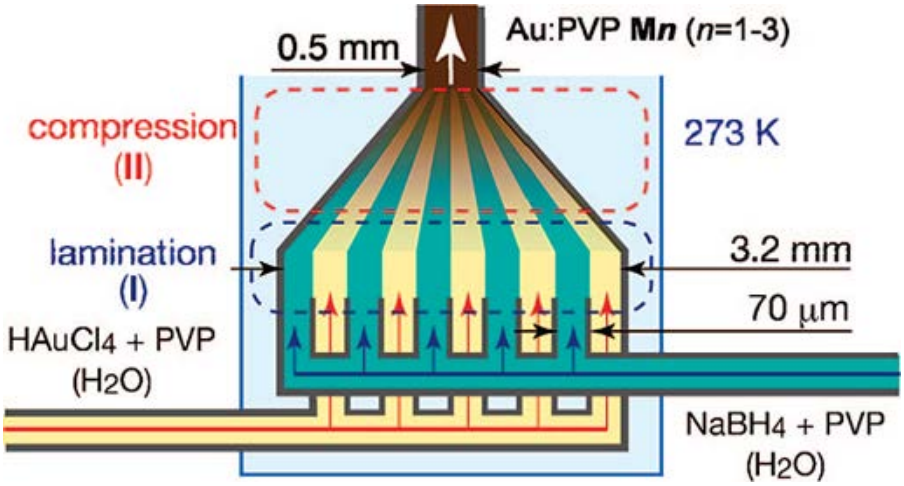

Fig. 7 SIMM-V2 micromixer made of Hastelloy C-22 for synthesis of ultrasmall PVP-stabilized Au NPs. The mechanism of the microreactor was based on multilamination and mixing of reactants (reprinted with permission from reference[29]).

One important challenge to be overcome in Au NP synthesis using microfluidic reactors is precipitation of Au NPs on the channel walls and finally fouling of the channel. Several

approaches has been suggested in literature to reduce/inhibit fouling of the microreactor channel, some of which are summarized below for devices made of Si-based materials and using aqueous solutions[40, 51, 55]:

1) Increasing pH value of the fluid inside the microreactor (pH 10),
2) pK_a of the channel surface OH group,
3) reducing the wetting ability of the channel walls (hydrophobic surfaces) e.g. by silanization of the walls with perfluorosilane,
4) using capping agents with appropriate charges e.g. PVP or citrate ions,
5) increasing the flow rate,
6) operating in segmented flow (described below).

Another class of microfluidic reactors is based on the multiphase flow mechanism. This method overcomes the drawbacks of single phase synthesis: first, in a laminar flow axial diffusion occurs, leading to a wide residence time distribution resulting in uncontrollable mixing and polydispersity of products and byproducts. Second, in continuous laminar flow, mixing and diffusion can be improved by generating a convective flux which requires lithographic techniques to incorporate additional structural elements e.g. splitting-and-recombination units (discussed earlier). Third, the deposited Au NPs on the channel occur in continuous flow acts as nucleation sites reducing the efficiency of the desired products. Moreover, after long experiments, the channel will finally be blocked. Introducing a second immiscible phase in the multiphase flows, the long diffusion time and dispersion limitations can be overcome. The mixing improves via transverse convection by inducing a recirculation motion in the liquid slug (Fig. 8). Additionally, the segmented flow inhibits contact between the slug containing Au NPs and the channel walls thereby preventing Au deposition on the walls and clogging of the channel[51, 61].

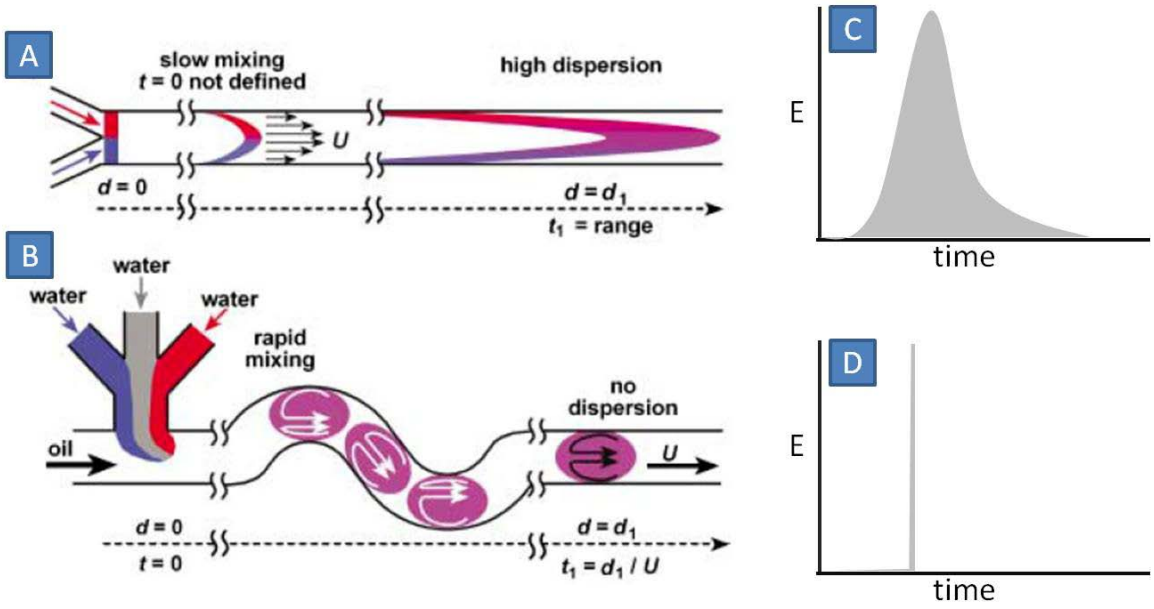

Fig. 8 Comparison of continuous laminar flow (one phase flow) with segmented flow (multiphase flow) considering the residence time distribution (reprinted with permission from reference[51, 61]).

1.5. X-ray Absorption Spectroscopy (XAS)

Synchrotron radiation is emitted by relativistic electrons circulating in storage rings. Compared to radiation provided by conventional light sources (e.g. X-ray tubes) synchrotron radiation exhibits several unique properties beneficial for scientific applications such as spectroscopic, diffraction and imaging techniques in a broad variety of research fields, e.g. materials science and biology. These properties include: High intensity, a high degree of collimation and polarization, continuous smooth photon flux distribution over a wide range of photon energies reaching from the infrared to the hard X-ray regime and a well defined pulsed time structure[62]. One specific synchrotron based method which has evolved into a powerful tool in materials science and nanotechnology and has become a well-established technique is X-ray absorption spectroscopy (XAS). XAS has several advantages with respect to the studies described in this thesis: XAS is a non-destructive, local probing technique and therefore unlike other characterization techniques not restricted to (crystalline) materials with long range order but also applicable to the analysis of amorphous systems, small nanoparticles[63-66] as well as samples in liquid or gas phase. Furthermore, the penetration depth of X-rays allow for *in situ* characterization of materials in catalytic reactors under working conditions or during synthesis in

microreactor channels (with X-ray transparent windows). XAS beamlines are available at the vast majority of synchrotron light sources around the world. Synchrotron beamlines branch off the storage ring and guide the synchrotron beam to the end stations where the samples are mounted for characterization. One essential optical element of an XAS beamline is the (mostly double crystal) monochromator which based on Bragg reflection (and higher harmonic rejection by a mirror or crystal detuned out of the parallel arrangement) slices a narrow photon energy band out of the broad synchrotron spectrum. The absorption coefficient of the sample at a specific photon energy is then determined by measuring the incoming monochromatic intensity and the monochromatic intensity transmitted through the sample. According to Lambert Beer´s law the absorption is proportional to the logarithmic ratio of these two intensities. For these transmission mode measurements in most cases ionization chambers are used. Alternatively, XAS can be collected in the fluorescence mode (Fig. 9). In this case, the absorption is correlated to the ratio of the intensity of a specific X-ray emission line from the chemical element under investigation (e.g. K_α), measured using a fluorescence detector (e.g. LN_2 cooled Ge detector), and the incoming intensity. X-ray absorption spectra, showing the absorption behavior of the sample as a function of the photon energy, are then recorded by scanning the monochromator (i.e. by stepwise or continuously varying the Bragg angle). Once the photon energy is sufficiently high to eject electrons from atoms in the sample material, an abrupt increase in absorption, a so-called absorption edge, is observed in the XAS spectra. Since the energetic positions of these absorption edges are characteristic for a specific chemical element in the sample, and since absorption edges of different chemical elements in most cases do not significantly overlap, XAS is an element specific method. The fine structure in XAS spectra is extremely sensitive to the atomic environment of the absorbing atoms. Commonly two energy regions are distinguished: The X-ray absorption near edge structure (XANES, region approx. ± 50 eV relative to the absorption edge) and the extended X-ray absorption fine structure (EXAFS, up to approx. 1000 eV beyond the edge). XANES features originate from electronic transitions into unoccupied orbitals and multiscattering processes of the ejected photoelectrons. They contain information about coordination geometry and oxidation state of the absorber atoms. The EXAFS oscillations at higher energies arise from interference effects of outgoing photoelectron waves and those backscattered by the neighbors of the absorber atoms. From EXAFS data information about coordination numbers, bond lengths as well as the degree of structural and statistical disorder in the sample material can be extracted[67].

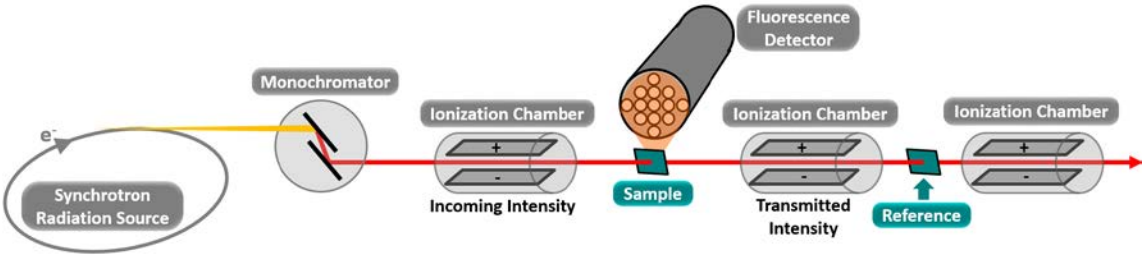

Fig. 9 Principle setup of an XAS experiment at a synchrotron light source. The incoming and transmitted intensities of the monochromatic X-ray beam are measured with ionization chambers. Alternatively, the intensity of a specific fluorescence line is monitored with a florescence detector. In parallel transmission data of a reference sample (e.g. metal foil) is acquired.

1.6. Motivation and Aim of the Thesis

The focus of this PhD work was laid on establishing a novel microfluidic setup, based on a reactor prototype[68] designed in a collaboration of TU Dresden, GeSiM, KIT-IMVT and KIT-ITCP (Grunwaldt group), for X-ray based *in situ* characterization by spectroscopic and scattering techniques in order to investigate the early stages of particle formation for catalysis. As a first case study, Au NP formation - a fast reduction reaction requiring a high time resolution (down to 2-20 ms) - was selected. The cyclone micromixers in the microfluidic chip are ideal for homogeneous mixing of the reactants within 2 ms at a flow rate of 2.6 L h^{-1}. In this device a continuous turbulent flow of reactants can be realized. This allows not only synthesizing advanced materials with specific properties, i.e. ultrasmall Au and Pd as well as homogeneous alloyed Au_xPd_y NPs with narrow size distributions, but especially pushing the time resolution limits for XAS analysis of Au NP formation in fast reactions. In this thesis, the application of the microfluidic setup for *in situ* XAS studies, preparation of monometallic Au/Pd and bimetallic AuPd nanoparticles as well as their in-depth characterization are reported. Finally, the potential of the microreactor in the field of precipitation reactions is investigated. The course of the thesis is as follows:

In chapter 2 (Experimental) the novel microfluidic setup specifically developed and built for this PhD work is explained in detail. XAS is a powerful characterization tool to determine the oxidation state and coordination environment of metal atoms in nanoparticles, especially since as a local technique it is not restricted to systems with long range order, but also applicable to X-ray amorphous materials. Since XAS was extensively

utilized for this thesis, the potential of this technique is explained in greater detail in section 1.5.

Chapters 3-6 show how the microfluidic setup can be employed to synthesize and to study high-quality NPs, which were afterwards characterized by various techniques. Each of these chapters feature specific introductions to the different synthesized materials and corresponding preparation pathways. Chapter 3 highlights an experimental study during which the microfluidic reactor was successfully used for synchrotron based *in situ* X-ray absorption spectroscopic measurements to investigate early stage kinetics of fast reactions at previously unavailable time resolution. Moreover, the NPs were tested as catalysts for CO oxidation (chapter 3-5) and as potential sensors. A $Cu/ZnO/Al_2O_3$ system for methanol synthesis was produced by co-precipitation in the microreactor and characterized by various methods (chapter 6).

2. Experimental

2.1. Microfluidic Setup

A novel microfluidic setup was built based on a previous prototype[68] in a collaboration of TU Dresden (Prof. Bartha), GeSiM, KIT-IMVT (Dr. G. Rinke, Prof. R. Dittmeyer and co-workers) and KIT-ITCP (Dr. G. Hofmann and Prof. J. -D. Grunwaldt) with infrastructure providing pulsation-free flow at high flow rates for the synthesis of NPs (Fig. 10). The reactants stored in ca. 4 L stainless steel corrosion-resistant vessels (polyethylene inner surface for gold vessel) were pressurized by N_2 and delivered to the microfluidic chip. All chemicals involved were handled in a closed system and pumped from the vessels through the microreactor to the exhaust container in a controlled way. Separate flowmeters were used for gold precursor and reducing agent solution (ENDRESS+HAUSER promag H with polyvinylidene fluoride inert parts and promass A models) to avoid decomposition of the precursors prior to entering the microreactor. Needle valves (IDEX and Swagelok) allowed for precise adjustment of each reactant flow individually. For safety, a fast shut down control system was installed and the entire setup housed in poly (methyl methacrylate) (PMMA).

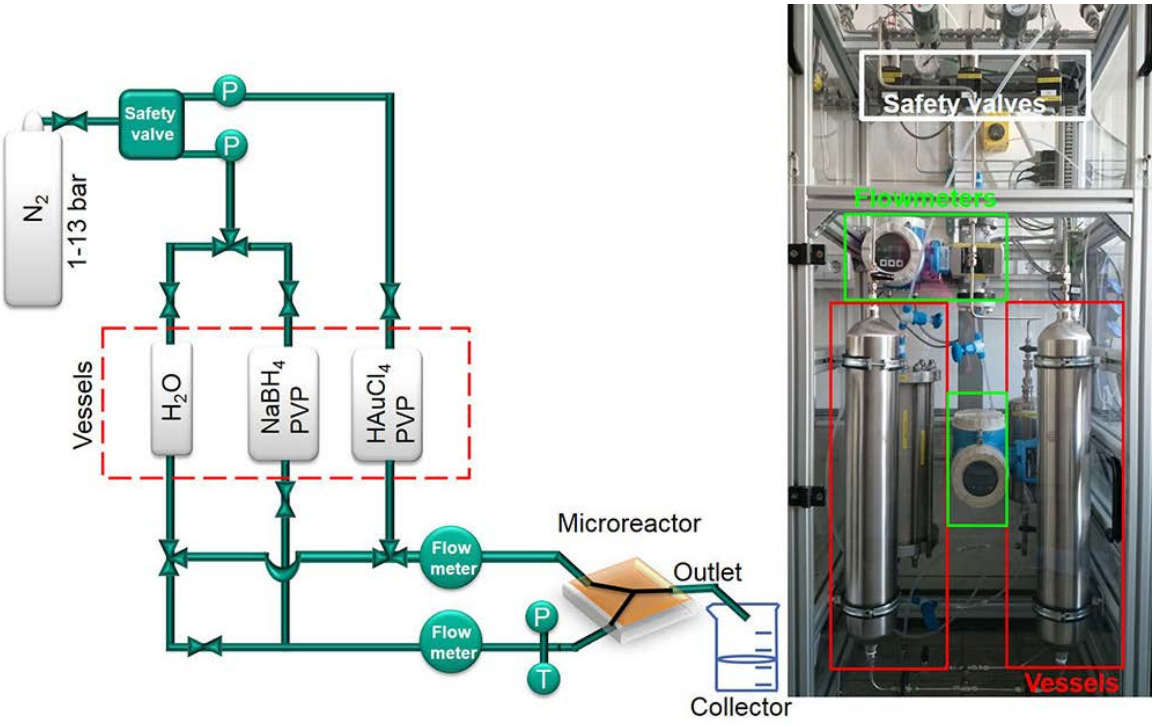

Fig. 10 Schematic of microfluidic setup for fast continuous flow synthesis of PVP-stabilized Au NPs (P: pressure transducer, T: temperature sensor)[39].

The microfluidic reactor was fabricated in collaboration with GeSiM GmbH and the Institute of Semiconductors and Microsystems at Technische Universität Dresden (TUD-IHM). It is made of Si-bonded glass with inlet and outlet ports produced by laser drilling in the glass part. This technique was also used for carving the cylinders for the cyclone micromixers in the Si chip. The microfluidic chip was specifically designed for X-ray based *in situ* characterization of NPs using spectroscopic and scattering techniques. It consists of 3 cyclone micromixers (based on a concept developed in collaboration between KIT-ITCP and KIT-IMVT[69]) followed by a meandering microchannel (300 × 300 μm^2) serving as the observation line. In the observation area, the thickness of the chip was reduced to 800 µm by Si etching (300 µm Si, 300 µm fluid channel and 200 µm glass) for X-ray-based experiments. The microfluidic chip and the supporting frame are shown in Fig. 11.

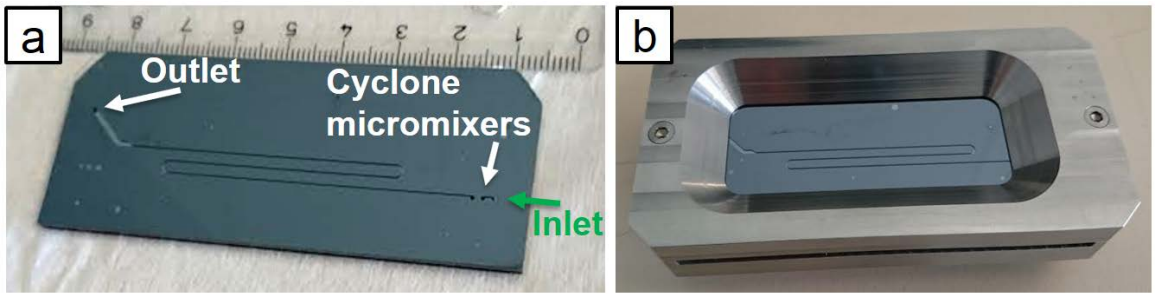

Fig. 11 a) Microfluidic chip, b) assembled in the supporting frame.

According to computational fluid dynamics (CFD) calculations by Achim Wenka (KIT-IMVT), three cyclone micromixers are required to achieve efficient mixing by applying a total reactant flow rate of 2.0 L h^{-1} resulting in a residence time of 2.9 ms and a pressure drop of 1.92 bar in the mixing region (Fig. 12). By using 13 bar pressure of N_2 gas to deliver the reactants at 2.6 L h^{-1} total flow rate (each reactant with 1.3 L h^{-1} flow rate) to the micromixers, a dead time below 2 ms can be achieved, which is essential for homogeneous mixing of the reactants to approach turbulent mixing conditions with a Reynolds number of about 2400. This provides efficient mixing in a sufficiently short time for fast reduction reactions (such as $NaBH_4$ in this case). The total residence time in the microfluidic device is 20 ms under the above mentioned conditions. The fluid mechanics (e.g. pressure drop and the flow environment) inside the microchannel are shown in Fig. 13, Table 1 and Table 2.

Prior to NP synthesis experiments, the microreactor channel walls were coated with Ombrello, which was injected by syringe tubing into the inlets of the microfluidic chip after it was treated in an oxygen plasma chamber[70] (50% power, 0.2 mbar and 2 min). In the next step, the chip was baked at 65 °C for 20 min. This well-established method was performed to minimize Au deposition by electrostatically repelling the PVP-stabilized Au NPs from the hydrophobic channel surfaces[71].

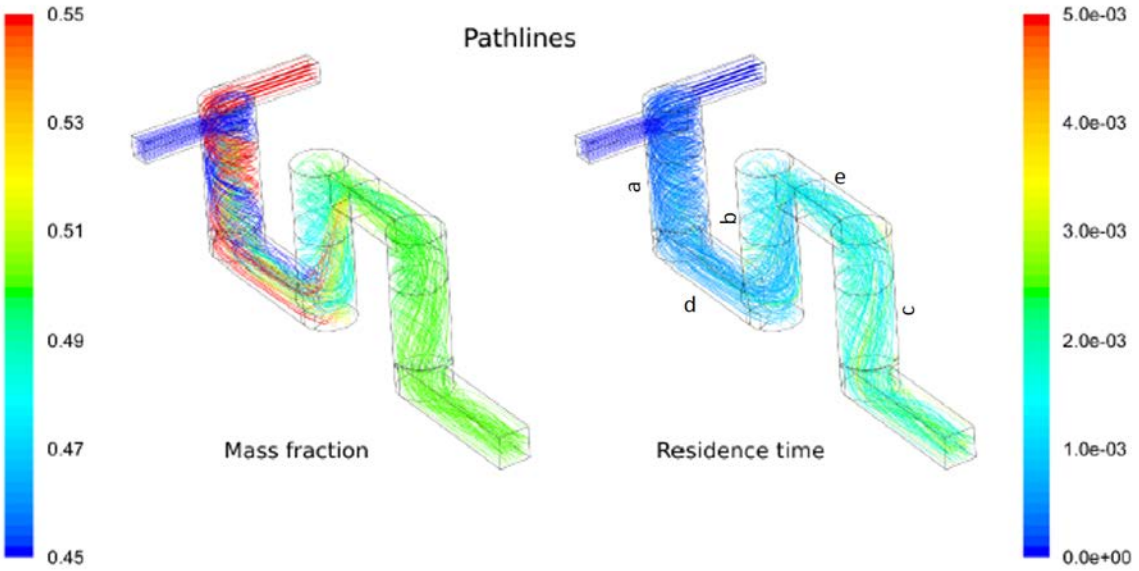

Fig. 12 CFD calculations for the three cyclone micromixers; (left) mass fraction and (right) residence time in seconds for total flow rate of 2.0 L h^{-1}. The diameters of the cyclones (a, b, c) are 500, 700 and 700 µm with 1500 µm height. The connecting channels (d, e) are 300 µm high and 300 µm wide (reprinted with permission from reference[72]).

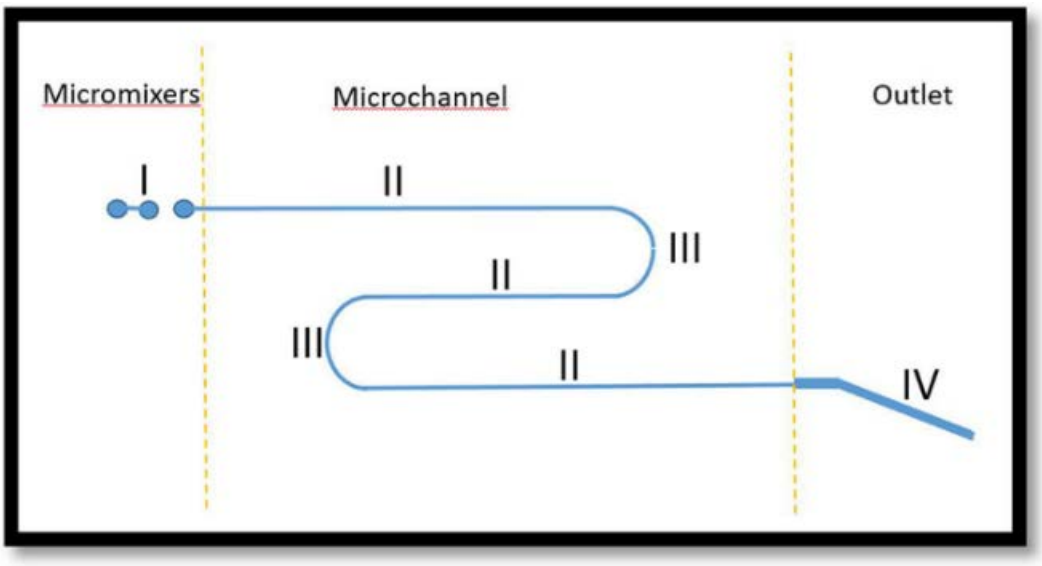

Fig. 13 Schematic of the microfluidic chip with labeled zones referring to pressure drop calculations shown in Table 1.

Table 1 Pressure drop of the reactant flow inside the microfluidic chip at different positions (cf. Fig. 13) estimated with water as the medium, 20°C temperature, 2.6 L h^{-1} flow rate and 13 bar pressure.

Zone	Description	Dimensions (mm)			Pressure drop (bar)
		W	H	L	
I	Micromixers with connections	-	-	-	4.1[a]
II	Rectangular tubes	0.3	0.3	138	7.5[b]
III	U-turns	0.3	0.3	7	0.8[b]
IV	Rectangular tubes	1	1	12	0
Total pressure drop					12.4

[a)] obtained from CFD calculations conducted at KIT-IMVT, [b)] calculated using the program "Druckverlust Online-Rechner", http://www.druckverlust.de/OnlineRechner/)

Table 2 Fluid mechanical conditions inside the microfluidic chip.

Parameters	Values
Medium	Water
Density	998.2 kg m^{-3}
Dynamic viscosity (20 °C)	1.00 mPas
Flow rate	2.6 L h^{-1}
Flow velocity	8.04 m s^{-1}
Reynolds number	2400
Flow type	Transitional region from laminar to turbulent flow
Pressure drop	12.4 bar

2.2. Characterization of Nanoparticles and Solid Materials

2.2.1 UV-Vis Spectroscopy

UV-vis absorption spectra of colloidal Au, Pd and Au_xPd_y solutions were recorded with a PerkinElmer- Lambda 650 UV-vis spectrometer with deuterium and tungsten halogen light sources (in the range of 200-800 nm wavelength, switching between the lamps at about 319 nm). Deionized water was used as a reference to calculate the absolute absorption of the samples. All measurements were performed *ex situ* in absorption mode using UV cuvettes under ambient conditions immediately after the synthesis of colloidal NPs to observe the behavior of the gold surface plasmon resonance (SPR) band in order to estimate particle sizes as well as the presence of palladium chloride (precursor) after the reduction reaction.

2.2.2 Transmission Electron Microscopy (TEM)

The catalyts powder samples were directly dispersed on Cu grids covered with holey carbon film. For colloidal samples, 5 µl of the diluted colloidal solution was dropped on a holey carbon Cu grid covered by 2 nm carbon film and then dried at room temperature. Morphology and microstructure of the catalysts were characterized by high angle annular dark-field (HAADF) scanning transmission electron microscopy (STEM) and high

resolution transmission electron microscopy (HRTEM), and their composition was analyzed by energy dispersive X-ray analysis (EDX) using an EDAX S-UTW EDX detector in a FEI Titan 80-300 microscope operating at 300 kV. Analysis of STEM-EDX mapping was carried out by using the TEM Image & Analysis (TIA 4.7 SP3 version) software. Particle size statistics of the specimens were performed on HAADF-STEM images by using the ImageJ 1.49v software[73].

2.2.3 X-Ray Absorption Spectroscopy (XAS)

In situ X-ray absorption near edge spectra (XANES) at the Au L_3-edge (11.919 keV), shown in chapter 3, were recorded at room temperature in fluorescence mode at SuperXAS beamline[74] of the Swiss Light Source (SLS) synchrotron radiation source (electron energy 2.4 GeV) using a Si (111) double-crystal monochromator (focused beamsize: 150 × 100 μm^2) and a 5 element SDD detector (SGX Sensortech). A single spectrum was acquired from 11.81 to 12.08 keV every 4 min. The data were analyzed using the Athena interface of the IFEFFIT software package[75].

The XANES and EXAFS spectra of Pd/TiO_2 and Au_xPd_y/TiO_2 pellets at the Pd K-edge (24.350 keV) presented in chapter 4 were recorded at room temperature in transmission mode at the P65 beamline of the PETRA III synchrotron radiation source (DESY, Hamburg) using undulator radiation (11 period undulator, flux ca. 10^{11} photons s^{-1}) and a Si (311) double crystal monochromator (beam size 1.2 × 0.5 mm^2). Higher harmonics were rejected by a pair of Pt-coated plane mirrors installed in front of the monochromator. Au L_3-edge (11.919 keV) XANES and EXAFS spectra of Au/TiO_2 and Au_xPd_y/TiO_2 pellets were recorded at room temperature in transmission mode with ionization chambers and in fluorescence mode (using a PIPS diode) at the undulator beamline P64 (60 period tapered undulator, flux ca. 10^{12} photons s^{-1}) at PETRA III using a Si (111) double crystal monochromator (beam size of 2 × 1 mm^2). Higher harmonics were rejected by a pair of Rh-coated plane mirrors in front of the monochromator.

Pd K-edge (24.350 keV) XANES and EXAFS spectra of Pd/TiO_2 and Au_xPd_y/TiO_2 pellets (chapter 5) were recorded at room temperature in transmission mode with ionization chambers at the recently installed wiggler beamline CAT-ACT at ANKA using a Si (311) double crystal monochromator (beam size of 1 × 1 mm^2). Higher harmonics were rejected by a Rh-coated mirror downstream from the monochromator. XANES spectra of the powder samples were recorded *in situ* (100-200 µm sieve fraction of sample diluted 1:1

with TiO_2 in a quartz capillary with 2 mm outer diameter and 0.02 mm wall thickness) in a N_2 flow (33 ml min^{-1} flow rate) while heating up to 400 °C at 5 °C min^{-1}. For data analysis the Athena and Artemis interfaces of the IFEFFIT software package were used[75].

2.2.4 X-Ray Photoemission Spectroscopy (XPS)

For XPS studies, a drop of produced colloidal Au:PVP NPs was placed on a Si wafer immediately after synthesis (unwashed) and dried in air for XPS studies. The washed and dried Au/TiO_2 powder samples were analogously investigated. The Au/TiO_2 powder samples were grafted on standard Prevac sample holder and sticked on designated carbon stripe. The XPS measurements were carried out under ultra-high vacuum conditions with a base pressure in 10^{-10} mbar range. Core-level spectra were recorded under normal emission with a VG Scienta R4000 electron analyzer using Al-K_α radiation (nonmonochromatic, 1486.6 eV). Prior to the elemental scans, a survey scan was measured for all the samples in order to detect all the elements present. The applied pass energies (E_{pass}) for survey and close-up scans were 100 eV and 50 eV, respectively. The energy resolution was better than 1 eV. The observed charging effects were compensated by calibrating spectra on C 1s line. In the case of colloidal PVP-stabilized Au NPs, the C 1s line from PVP was deconvoluted into three peaks with methylene carbon as most intense peak at 284.5 eV[29, 76]. For THPC-stabilized Au NPs, the C 1s line at 284.8 eV was used (chapter 3). To eliminate the surface charging for calcined Au_xPd_y/TiO_2 catalysts investigated in chapter 5, the binding energies were shifted to the C1s line at 285.00 eV. The XP spectra were deconvoluted using the Casa XPS program[77] with a Gaussian-Lorentzian mix function and Shirley background subtraction.

2.2.5 X-Ray Diffraction (XRD)

X-ray diffraction patterns of the catalysts were recorded using a D8 Advance Diffractometer by Bruker. The measurements were performed *ex situ* under ambient conditions in a 2θ range of 10°–80° (2 s/step, step size 0.016°) using Cu-K_α radiation (λ=0.15406 nm), a nickel filter and a graphite monochromator.

2.2.6 UHV-Fourier-Transform Infrared Spectroscopy (UHV-FTIR)

The IR measurements were performed with a state-of-the-art ultra-high vacuum (UHV) apparatus, combing a FTIR spectrometer (Bruker Vertex 80v) and a multi-chamber UHV system (Prevac). This innovative and dedicated design not only allows to perform infrared

reflection-absorption spectroscopy (IRRAS) measurements at grazing incidence on well-defined model oxide surfaces, but also enables to record IR spectra in transmission mode on polycrystalline oxide powders[78]. 200 mg Au_xPd_y/TiO_2 (x:y = 1:0, 7:3, 1:1, 3:7, 0:1) sample was pressed into an inert metal mesh and mounted on a sample holder, which was specially designed for the transmission FTIR measurements. The samples were treated by annealing at 400 °C for 1 h at UHV conditions. Exposure to CO at selected temperatures, typically at 110 K, was achieved by using a leak-valve-based directional doser connected to a tube (2 mm, inner diameter) that terminated 3 cm from the sample surface and 50 cm from the hot-cathode ionization gauge. IR data were accumulated by recording typically 1024 scans with a resolution of 4 cm^{-1}. Prior to each exposure, a spectrum of a clean sample was recorded as a background reference. After CO exposure at 110 K, the samples were heated to higher temperatures and the *in situ* IR spectra were recorded continually. Peak fittings on the IR spectra of CO adsorbed at different sites were conducted, and the normalized peak areas were shown as a function of temperature.

2.2.7 Inductively Coupled Plasma-Optical Emission Spectroscopy (ICP-OES)

For the measurements described in chapter 3, the amount of Au in the samples was determined by inductively coupled plasma-optical emission spectrometry (ICP-OES, OPTIMA 4300 DV from PerkinElmer). About 10–20 mg of the samples (weighing accuracy ± 0.01 mg) was dissolved in 4 mL hydrochloric acid and 40 mL sulfuric acid at 241 °C for 12 hours in a stainless steel pressure vessel DAB-2 from Berghof. Elemental analysis was accomplished with four different calibration solutions and an internal standard (Sc). Three wavelengths of the elements have been used for calculation.

For the experiments reported in chapter 4, the elemental composition of the samples with respect to Pd and Au was determined by ICP-OES spectroscopy (iCAP 7600, Thermo Fisher Scientific).10 mg of each sample were dissolved in 4 mL nitric acid and 4 mL sulfuric acid at 513 K for 10 h in a pressure digestion vessel (DAB-2 Berghof). Analysis of the elemental composition was carried out using four different calibration solutions and an internal standard (Y) based on three characteristic Au and Pd emission lines.

For the measurements described in chapter 6, the weight percentage of Al, Cu and Zn was determined by ICP-OES spectroscopy (Optima 4300 DV, PerkinElmer). 10 mg of the samples (accuracy ± 0.01 mg) was dissolved in 4 ml hydrochloric acid and 4 ml sulfuric acid at 513 K for 6 h in the pressure digestion vessel DAB-2 (Berghof). Elemental analysis

was carried out with four different calibration solutions and an internal standard (Sc). Three wavelengths of the elements were used for calculation.

2.2.8 Chemisorption

For chemisorption analysis, a Micromeritics AutoChem 2950 HP equipped with a thermal conductivity detector (TCD) and a MKS Cirrus 2 mass spectrometer (MS) was used. 160 mg of sample were placed in a U-shaped quartz glass sample cell. Fine quartz wool was placed in front and behind the sample bed to keep it at a constant axial position and to ensure plug flow conditions. The sample was dried under an Ar flow of 30 mLN min^{-1} *in situ* by heating it from room temperature to 250 °C at 5 °C min^{-1} and holding the temperature at 250 °C for 2 h.

Afterwards, the sample was cooled down to 50 °C and temperature-programmed reduction (TPR) at ambient pressure in a flow of 30 mLN min^{-1} of 5% v/v H_2 in Ar through the sample was started, increasing the temperature at a rate of 1 °C min^{-1} up to 250 °C and holding the sample at this temperature for 30 min. The effluent gas from the cell was passed through a cooling trap at 0 °C to condense any water formed. The dry gas was then analyzed by a TCD and MS in series. The H_2 signal of the MS (m/z = 2) was calibrated with a known concentration of 5% v/v H_2 in Ar before and after each measurement and used for quantification of the overall H_2 consumption during reduction.

Subsequently, N_2O pulse chemisorption was conducted. The sample was cooled to room temperature and flushed with 30 mLN min^{-1} He for 30 min. Afterwards, 40 pulses with 0.32 mLSTP of 30% v/v N_2O in He were dosed onto the sample. The effluent gas from the sample was passed through a cooling trap at -196 °C to separate any N_2O not converted to N_2. The N_2 formed by partial oxidation was then analyzed with a TCD and MS in series. The TCD data was used to determine the metallic Cu surface area and Cu dispersion (Cu atomic area 0.068 nm^2, stoichiometry factor 2.0).

2.2.9 Procedure for CO Oxidation Tests

The catalytic tests described in chapter 3 were carried out in a fixed-bed quartz flow reactor (inner diameter 8 mm) in a temperature programmed mode from 40 to 175 °C at a ramp rate of 1 °C min^{-1}. 400 mg of catalyst (sieve fraction 125–250 μm) was placed between glass wool plugs in the quartz tube. The bed length was about 10 mm and the gas flow 300 mL min^{-1} (gas hourly space velocity (GHSV): 36000 h^{-1} and CO feed rate: 5.1×10^{-7} mol s^{-1} g^{-1}_{cat}). The gas mixture contained 1000 ppm CO and 1000 ppm O_2 diluted with nitrogen

and dried by a cold trap (dry ice/isopropanol). Reaction products were analyzed using a URAS 26 CO/CO_2 analyzer. Prior to the testing, catalysts were dried in N_2 flow for 2 h to remove water. CO conversion was calculated using the following equation:

$$X_{CO} = 1 - \frac{C_{CO}^{outlet}}{C_{CO}^{inlet}} = \frac{C_{CO_2}^{outlet}}{C_{CO}^{inlet}}$$

where C_{CO}^{inlet} , C_{CO}^{outlet} and C_{CO2}^{outlet} denote CO and CO_2 concentrations at the inlet and outlet of the reactor.

CO oxidation was chosen as a relatively well-understood test reaction to investigate the catalytic properties of the metal NPs (chapter 4). The tests were carried out in a fixed-bed quartz flow reactor (quartz tube, inner diameter 8 mm) in a temperature programmed mode from 30 °C to 250 °C at a ramp rate of 1 °C min^{-1}. 300 mg of 1 wt.% Au/TiO_2, Pd/TiO_2 and Au_xPd_y/TiO_2 catalyst (sieve fraction 125–250 μm) were placed between glass wool plugs in the quartz tube. The catalyst bed length was ~10 mm, and the gas flow 600 ml min^{-1} (GHSV: 72000 h^{-1}). The gas mixture contained 1000 ppm CO and 10% O_2 in nitrogen (CO feed rate: 13.3×10^{-7} mol s^{-1} g^{-1}_{cat}). Before reaching the reactor the gas feed passed through a Messer Hydrosorb® cartridge to remove traces of water. Reaction products were analyzed using an URAS 26 NDIR CO/CO_2 analyzer. Prior to the testing, catalysts were dried in N_2 flow for 2 h to remove residual water and then pre-treated in 5% H_2 in N_2 at 250 °C for 1 h. Each heating and cooling cycle was performed twice. The results from the second cycle are reported in this work. Turnover frequencies (TOFs) were determined in the region of CO conversion below 20% (for Au/TiO_2 below 25%) and on the assumption that the reaction rate (r) was independent of the CO concentration. Metal dispersion for TOF calculation was obtained from the average particle size (determined by STEM) assuming spherical particles.

Chapter 5 describes how CO oxidation was applied as a complementary test reaction to UHV-FTIR measurements in order to investigate the catalytic properties of the metal NPs supported on TiO_2. For this purpose, CO oxidation experiments were carried out two times after pretreatments under different conditions once in N_2 up to 400 °C for 1 h and under H_2 pretreatment in 5% H_2 in N_2 up to 250 °C for 1 h to reduce the metal NPs. The tests were performed in a fixed-bed quartz flow reactor (quartz tube, inner diameter 8 mm) in a temperature programmed mode from 30 °C to 250 °C at a ramp rate of 1 °C min^{-1}. 70 mg of 2.4 wt.% Au/TiO_2, Pd/TiO_2 and Au_xPd_y/TiO_2 catalysts (sieve fraction 125–250 μm) were

mixed with 930 mg SiO_2 and then placed between glass wool plugs in the quartz tube. The catalyst bed length was ~15 mm, and the gas flow 600 ml min^{-1} (GHSV: 48000 h^{-1}). The gas mixture contained 1000 ppm CO and 10% oxygen in N_2 (CO feed rate: 5.8×10^{-6} mol s^{-1} g^{-1}_{cat}). The gas feed passed through a Messer Hydrosorb® cartridge to remove traces of water before reaching the reactor. Reaction products were analyzed using a URAS 10E NDIR CO/CO_2 analyzer. Each heating and cooling cycle was performed twice. The results from the second cycle are reported here. TOFs were determined in the region between 3-17% CO conversion (for Au/TiO_2 below 40%) and based on the assumption that the reaction rate was independent of the CO concentration. Metal dispersion for TOF calculation was obtained from the average particle size (determined by STEM).

3. Formation of Ultrasmall Au Nanoparticles[1]

In the previous chapter, the establishment of a novel microfluidic setup for *in situ* characterization of colloidal nanoparticles during synthesis was described. The following chapter demonstrates how the microfluidic setup was successfully used to synthesize ultrasmall Au nanoparticles with narrow size distribution and to study their formation with high time resolution using synchrotron based *in situ* X-ray absorption spectroscopy. Finally, the produced particles were subjected to CO oxidation as model reaction for catalytic performance.

3.1. Introduction

Colloidal Au NPs are regarded as promising candidates for various applications in the fields of catalysis, sensing, bio-imaging, medical and analytical sciences, optics, nanoelectronics etc[40, 51, 54, 79-85]. For these applications, Au NPs have been produced by different techniques such as electrochemical, photochemical and chemical methods. One of the most common routes is the chemical reduction, in which the Au ions obtained from a precursor are reduced to Au atoms in oxidation state zero, which in the next step, join together to form nuclei. Further coalescence of nuclei results in nanoparticle formation[25, 45, 54] (Fig. 14).

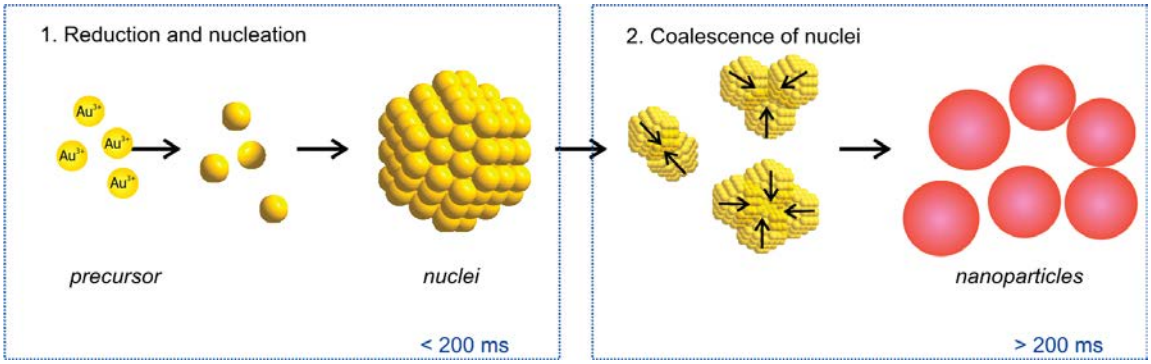

Fig. 14 The mechanism of gold nanoparticle formation using $NaBH_4$ as reducing agent (reprinted with permission from reference[45]).

Identification of the most important operation parameters for gold nanoparticle formation has been subject of intensive research. One important factor is the effect of different reducing agents and their reduction powers varying from weak reducing substances like

[1] Part of this chapter has been published in Reaction Chemistry & Engineering[39].

ascorbic acid[25, 55], citric acid[49] and sodium citrate[25, 27, 79, 86] to strong reducers such as sodium borohydride[25, 87, 88], hydrogen[27], hydrazine[89] and Tetrakis (hydroxymethyl) phosphonium chloride (THPC)[3, 90, 91]. The shape, size and polydispersity of nanoparticles are strongly affected by reducing agents applied[22].

Tsubota et al.[12] reported in early publications that gold NPs smaller than 3 nm were the most active for CO oxidation compared to NPs with larger diameters. According to Grunwaldt et al.[3], 2 nm large particles prepared by THPC in an alkaline solution can be deposited on titania or zirconia and exhibit high activity for the same catalytic reaction. Thus, simple methods for the synthesis of ultrasmall Au NPs are of wide interest in the field of gold catalysis. 'Ultrasmall NPs' is a widely used term in the materials science community, referring to NPs with 1-3 nm core size, bridging the gap between single molecules and classical larger sized NPs, with 70% of the atoms located on the surface and physiochemical properties uniquely differing from the corresponding bulk materials[19-21].

For a rational design of nanostructured functional materials, it is crucial to separate nucleation and growth processes from each other in order to control diffusive growth, and to tailor particle sizes and shapes as well as physical and chemical properties[50, 51]. Compared to conventional stirred batch reactors, synthesis of NPs in a continuous flow using microfluidic reactors has evolved as a promising method with several benefits, e.g. fast mixing, easy process handling, high mass and heat transport and process parameters within a wide range of operating conditions[52, 53, 56]. Furthermore, microfluidic reactors can be designed in a way that spectroscopic or diffraction measurements are possible during synthesis. This allows deeper insights into different stages of NP formation and to control intermediate processes occurring during synthesis[46, 47, 49, 92, 93]. These advantages have motivated growing competition in the field of fabrication technology of microfluidic chips, e.g. with respect to development of chip materials (e.g. silicon, glass and plastic), precise fabrication of channel structures and surfaces as well as improvement of time and cost efficiency and mass production[58, 94-96].

For optimized NP synthesis in microfluidic reactors, the influence of several parameters (e.g. flow rate, concentration ratio of precursors and reducing agents, pH, etc.) on nanomaterial properties resulting from structure, particle size and size distribution, morphology and interparticle interactions should be investigated in detail[20, 29, 41, 55, 97]. In this context *in situ* and *operando* studies and the combination of complementary

characterization techniques are crucial[46, 49, 92, 93]. In a recent study, *in situ* transmission electron microscopy (TEM) was used to investigate the dynamics of the nucleation of Au nanoclusters from supersaturated aqueous solutions. During those experiments Au^{3+} ions were reduced to Au^0 by the high-energy electron beam instead of using a reducing agent. This technique revealed that spinodal decomposition of the homogeneous Au solution (starting point at 3 s) resulted in a mixture of gold-rich and a gold-poor liquid phase at 9.2 s, which at 11.3 s turned into amorphous Au nanoclusters and finally into crystalline gold nuclei (at 15.4 s)[98].

The state-of-the-art in time-resolved studies of Au NP nucleation and growth using reducing agents is structural characterization of the produced NPs by small angle X-ray scattering (SAXS) and X-ray absorption near edge structure (XANES) in a reaction time window down to 100 ms after mixing the reactants, as demonstrated by Abécassis et al.[46, 47] and Polte et al.[45] in a stopped-flow and continuous flow, respectively. Abécassis et al. studied for the first time the formation of Au NPs *in situ* using SAXS and XANES at 100 ms time resolution. The Au NPs were produced during reduction of $AuCl_3$ with tetrabutylammonium borohydride (TBAB) and didodecyldimethylammonium bromide (DDAB) as surfactant in toluene, with turbulent mixing and a stopped-flow setup. The X-ray absorption data indicated the presence of Au(I) 104 ms after mixing which was gradually reduced to Au(0). Furthermore, these experiments revealed a strong influence of ligands and temperature on the kinetics of the reduction reaction[46]. Polte et al.[45] showed that reduction of the Au(III) precursor by sodium borohydride was complete at some point below 200 ms in a continuous flow by using a static mixer and recording SAXS data in an observation window from 100 ms to 136 s and XANES spectra 200 ms after mixing the reactants. These studies highlight the necessity of experiments at even higher time resolution, which not only require faster data acquisition but also efficient mixing on such short time scales. This requires to combine expertise from microfluidics, chemical engineering and spectroscopic techniques.

This chapter describes experiments using a novel microfluidic device[39, 68] with efficient micromixers for small mixing times (< 2 ms), which was specially designed for preparation of small colloidal noble metal particles and simultaneous *in situ* X-ray absorption spectroscopic investigations of the early stages (2 to 20 ms) of fast reduction reactions. In this case $NaBH_4$ was used to synthesize ultrasmall Au NPs (1.0 ± 0.4 nm) stabilized with polyvinylpyrrolidone (PVP) under flow conditions approaching turbulent mixing and plug

flow. The produced NPs were further characterized by various techniques, and their catalytic activity with respect to CO oxidation was tested in order to demonstrate potential applications in catalysis.

3.2. Colloidal Synthesis Procedure and Catalyst Preparation

3.2.1 Materials

Tetrachloroauric acid ($HAuCl_4 \cdot 3H_2O$; ≥99.9% purity), sodium borohydride ($NaBH_4$; 99.99% purity), polyvinylpyrrolidone (PVP; $(C_6H_9ON)_x$ with an average molecular weight of 40 kDa), tetrakis(hydroxymethyl)phosphonium chloride (THPC; 80% in H_2O), sodium hydroxide (NaOH) and sulphuric acid (H_2SO_4; 95% solution) were received from Sigma-Aldrich and used without further purification. High surface area titania (CristalACTIV^{TM}, commercially available G5, anatase; >99% purity; 370 $m^2\ g^{-1}$ surface area) was used as support. The microchannel walls were coated with Ombrello, a commercially available water repellent received from Autoteilemann GmbH.

3.2.2 Microfluidic Synthesis of Au:PVP NPs Reduced by $NaBH_4$

The preparation procedure of reactant solutions was adopted from Tsunoyama et al.[29], however, the concentration of reactant solutions was optimized for this specific microreactor with defined flow rates. 1.8 g Au precursor and 0.85 g $NaBH_4$ were dissolved separately each in 750 mL deionized water. To each of these two solutions 10 g PVP was added as stabilizer. Gold precursor and reducing agent solutions were poured into separate vessels (Fig. 10). Nitrogen pressure of ca. 13 bar was used to push the reactant solutions in the channels to achieve a total flow rate of 2.6 L h^{-1}. The products were collected in a stirred round-bottom flask, which was placed in an ice/water bath. The microfluidic chip was flushed first with aqua regia and then with water before each synthesis.

3.2.3 Batch Synthesis of Au NPs Reduced by $NaBH_4$

The same ratio of Au:$NaBH_4$ used for the microfluidic synthesis of NPs was applied for batch synthesis, i.e. 59.3 mg gold precursor and 333.3 mg PVP were dissolved in 120 mL deionized water. 28.3 mg $NaBH_4$ and 333.3 mg PVP were dissolved in 30 mL deionized water and added to gold precursor solution being stirred rapidly at room temperature. The fast reduction reaction was observed through a color change from light yellow to dark brown.

3.2.4 Batch Synthesis of Au NPs Reduced by THPC/NaOH

As a second method, a procedure was adopted from Duff et al[91]. The reducing agent THPC is a short-chain compound which acts both as a reductant and an ionic stabilizer in aqueous solutions[99]. First 1.5 mL of sodium hydroxide (0.2 M) was added to 46 mL of deionized water, while mixing in a round-bottom flask on top of a magnetic stirrer running at 500 rpm. 1.2 mL of 80% THPC was diluted in deionized water to 100 mL. Then 1.0 mL of this diluted THPC was added to the NaOH solution. After 2 min of stirring, 1.2 mL of 43 mM gold precursor was added to the solution and a fast reaction was observed through a color change from light yellow to dark brown.

3.2.5 Immobilization of Au NPs on TiO_2

For immobilizing the Au NPs on titania support, the PVP-stabilized Au NP solution produced in the microreactor was added to a suspension of 1 g titania in 80 mL water acidified with 6 mL H_2SO_4 solution (0.2 M) while stirring at room temperature. After adsorption of the gold colloids on the support, the suspension was centrifuged three times (4500 rpm, 10 min each) and washed with water. Subsequently, the material was dried at 70 °C overnight. A sample of this material was calcined at 300 °C for 90 min, while the remaining material was directly characterized and used for CO oxidation tests (uncalcined samples). This method was used to prepare catalytic materials with different Au loading (0.7 and 1.7 wt.%) on TiO_2.

3.3. Early Reaction Stages of Au Nanoparticle Formation

For obtaining pulsation-free flow at high flow rates for the synthesis of NPs the novel microfluidic setup describe in section 2.1. was used (Fig. 10). The reactants in the vessels were pressurized by N_2 and injected into the cyclone micromixers in the microfluidic chip. High flow rates through the small channels ($300 \times 300\ \mu m^2$) were fine adjusted with needle valves. This setup allows precise correlation of reaction time and X-ray beam position along the microchannel with high time resolution and thereby to accurately determine the residence time of Au NPs in the reaction channel (further fluid mechanical properties are summarized in Section 2.1. Fig. 12 and 13, Table 1 and 2). The setup and operating parameters were optimized for a total flow rate of 2.6 L h^{-1} (1.3 L h^{-1} for each reactant flow), a Reynolds number of 2400 approaching turbulent flow conditions[68, 100, 101], a pressure drop of ca. 9 bar inside the microchannel, a deadtime below 2 ms in the micromixers and residence time of ca. 20 ms in the microchannel. The flow conditions were

simulated by computational fluid dynamics (CFD) in order to optimize homogeneous mixing of the reactants in the cyclone micromixers (Fig 12).

The microfluidic chip was installed in a stainless steel support frame with access to two reactant inlets, one product outlet and an X-ray transparent Si/glass observation window. Afterwards, the chip was attached to a motorized sample stage which allowed to illuminate different positions along the microchannel downstream from the micromixers (Fig. 15) with the focused X-ray beam. The reduction reaction of Au NPs formed during the first 20 ms of the reaction was monitored by mapping the oxidation states of Au in solution in the microfluidic device by XAS with the microfocused beam. First, only Au precursor solution was injected into the microchannel in order to precisely locate the channel by Au-L_3 fluorescence mapping and to choose measurement positions. For NP synthesis the total flow rate of reactants ($HAuCl_4$/PVP and $NaBH_4$/PVP solutions) was adjusted to ca. 2.6 L h^{-1} in order to achieve turbulent lateral mixing; thus, lateral concentration gradients could be minimized and a plug flow behavior was reached. *In situ* XAS was used to follow the reaction progress in this continuous rapid flow by recording absorption spectra at different positions along the channel to probe the oxidation states of Au during reduction. The XANES spectra in Fig. 16 clearly indicate a significant contribution of oxidized Au after the first 6 ms of the reaction, whereas after ca. 10 ms reduction of Au was complete. The mixing of the reactants prior to the observation channel was optimized for monitoring such fast reactions. Accordingly, these results show that the reduction of Au^{3+} by $NaBH_4$ in the presence of PVP proceeds within a short time frame of 10 ms.

This is the first study of Au NP formation in a microfluidic device within such a narrow time window. Polte et al.[45] acquired SAXS and XANES data of Au NPs 100 ms and 200 ms after the start of the reaction, respectively. They concluded that reduction of Au^{3+} with $NaBH_4$ was complete at some earlier time, and focused on the nucleation and growth processes occurring at a later stage. Abécassis et al.[46] investigated the synthesis of Au NPs during reduction of $AuCl_3$ in an organic solvent (toluene) by a milder reducing agent (TBAB) *in situ* using SAXS and XANES with 100 ms time resolution. At 104 ms after mixing they observed Au^+ which was gradually reduced to Au^0. Our setup allows investigation of early stages of such fast reactions and thereby a new insight into reduction and nucleation during NP formation in a microfluidic device.

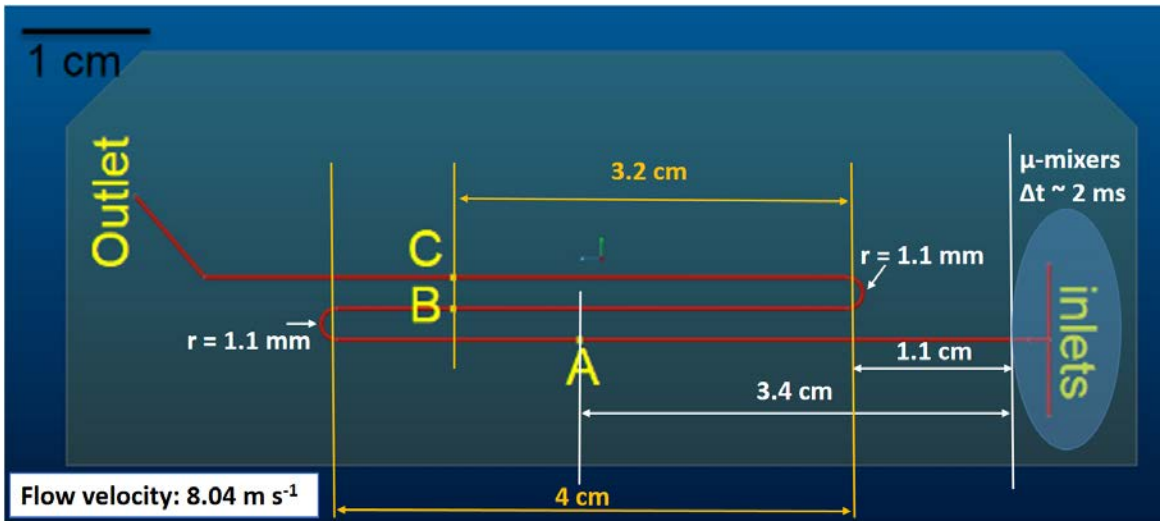

Fig. 15 Spatial-temporal points in the microchannel selected for XAS measurements (Positions A, B and C with corresponding reaction times of 6 ms, 10 ms and 18 ms).

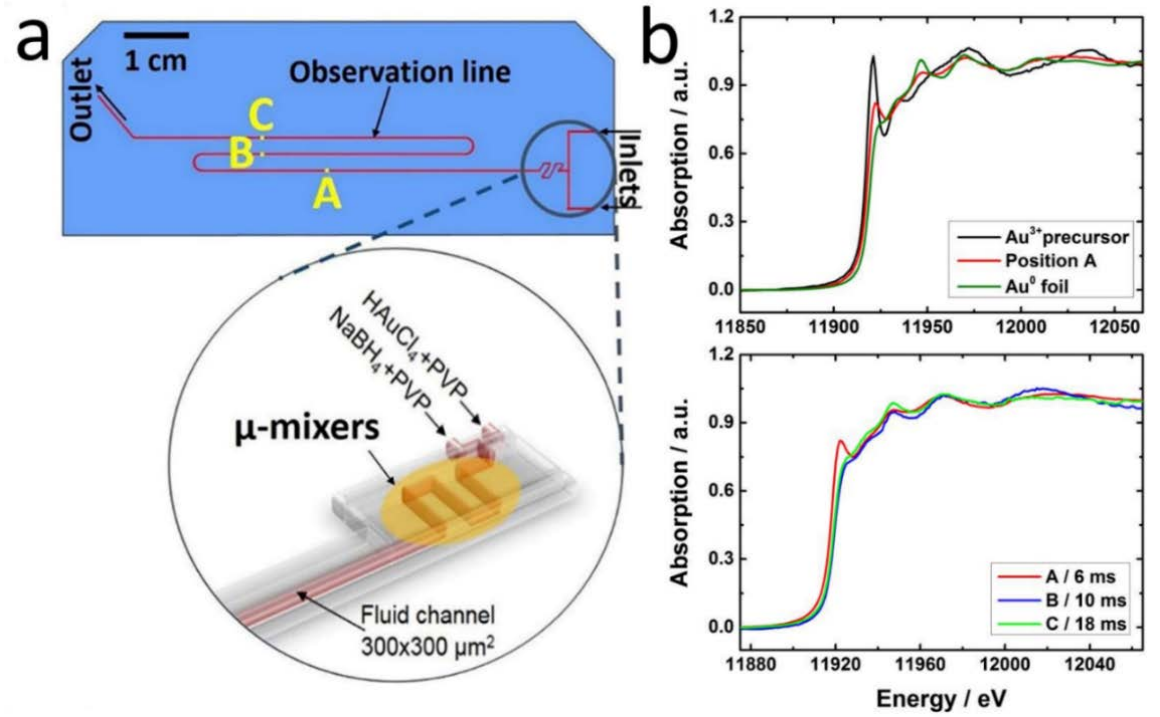

Fig. 16 a) Microfluidic chip, positions along the channel where *in situ* XAS data were acquired are marked, inset: schematic of the inlets and micromixers in the chip to achieve homogeneous mixing; b) reference spectra of Au^{3+} precursor and Au^{0} foil compared to absorption data acquired at position A (top) and XANES spectra recorded at different positions correlated to reaction times (bottom)[39].

3.4. Comparison of Au NPs Produced from the Microfluidic and Batch Reactor

The Au:PVP NPs synthesized in the microfluidic reactor were characterized by UV-vis spectroscopy and compared with Au NPs produced in the batch reactor. The NPs produced in the batch reactor were prepared using the same Au:PVP:$NaBH_4$ ratio as for microfluidic synthesis, and THPC/NaOH, respectively. Compared to the Au NPs prepared in batch reactor, in the spectrum of Au:PVP NPs produced in the microfluidic reactor a stronger suppression of the surface plasmon resonance (SPR) band was observed (Fig. 17a), which indicates formation of smaller NPs. In previous publications a strong suppression of the SPR was reported for ultrasmall Au NPs with diameters below 3 nm, in which surface scattering is the dominant factor[3, 29, 79]. These results illustrate the benefits of microfluidic synthesis compared to batch synthesis, indicating that homogeneous mixing of the reactants is already been achieved before the rapid reduction occurrs.

The hydrophobic wall surfaces efficiently inhibited Au deposition in the channels. However, in order to investigate the effect of the Ombrello-coated channel walls on the synthesis, the Au NPs produced in uncoated and coated channels were compared by UV-vis. The results indicate Au NPs with smaller diameters compared to the particles formed in the uncoated channel (Fig. 17b). Fig. 18 clearly shows deposition of Au NPs on the uncoated channels and blocking of the channel, which in the case of the Ombrello-coated channel is prohibited.

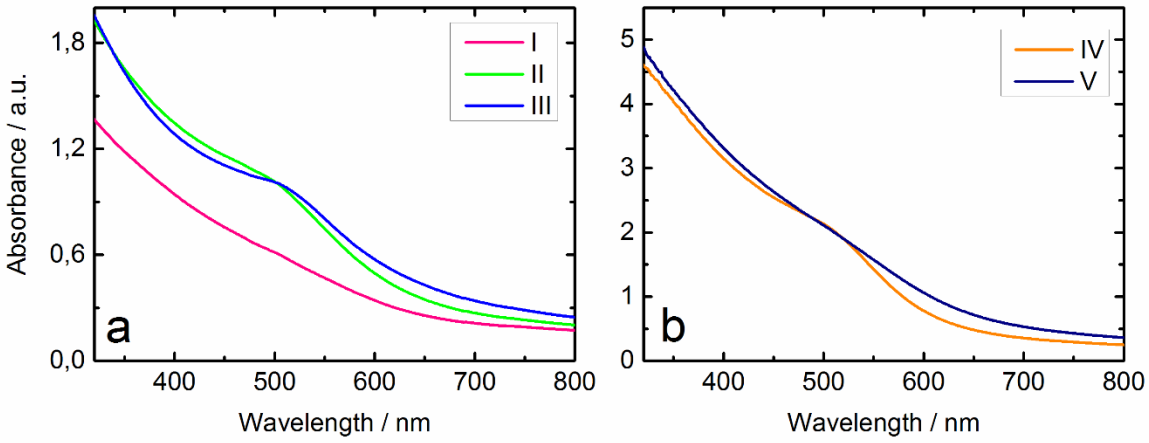

Fig. 17 a) UV-vis spectra of: (I) diluted Au:PVP NPs synthesized in microreactor using $NaBH_4$, (II) Au:PVP NPs synthesized in batch reactor using $NaBH_4$ and (III) Au NPs reduced by THPC/NaOH in batch reactor. b) Influence of hydrophobic channel coating on UV-vis spectra of Au:PVP NPs produced in the microreactor; (IV) Au:PVP NPs produced in uncoated and (V) Au:PVP NPs produced in Ombrello-coated microchannel[39].

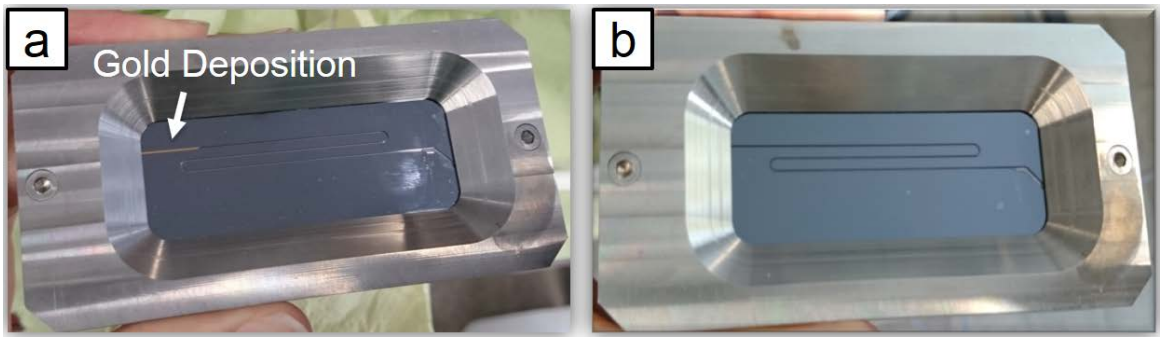

Fig. 18 The microfluidic chip after the Au NP synthesis in the a) uncoated microchannel and b) Ombrello-coated microchannel.

The three colloidal samples discussed above were analyzed by UV-vis spectroscopy once more about 3 months later to study their stability over time with respect to aggregation via their SPR behavior. Compared to fresh samples (shown in Fig.17a), the UV-vis spectra in Fig. 19 clearly indicate a change in NP size distribution which was also visible as a color change from brown to red/violet. However, particle aggregation over time was much more drastic in the case of Au NPs produced in batch reactor using PVP/$NaBH_4$ and THPC/NaOH. In the case of Au/THPC, which is a short-chain compound, the size distribution was much broader compared to Au/PVP/$NaBH_4$ indicating of higher stability of Au:PVP NPs. Interestingly, among the Au/PVP/$NaBH_4$ samples, the NPs produced in the microfluidic reactor turned out to be more stable (although they also showed NP growth compared to the fresh sample) than those from the batch reactor, indicating homogeneous mixing of reactants and the surfactant, and effective preservation of NPs against aggregation due to presence of PVP in the microreactor.

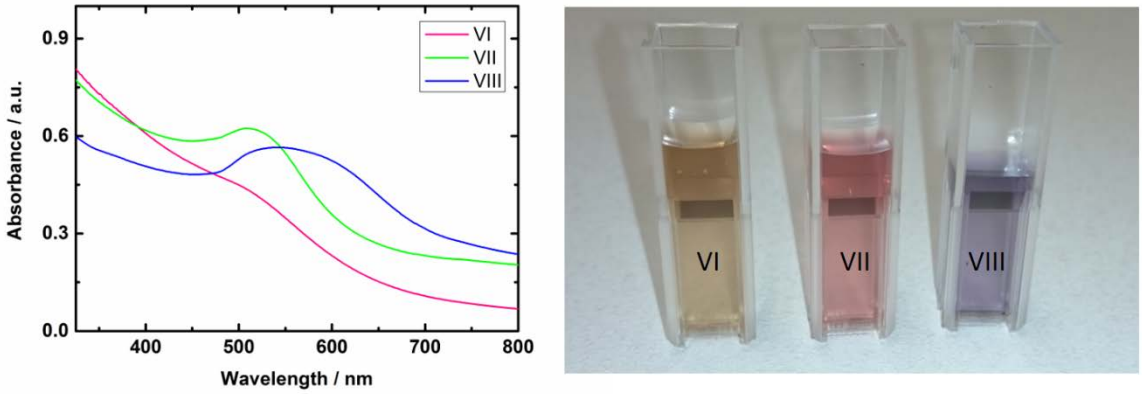

Fig. 19 UV-vis spectra of ca. 3 months old samples: (VI) Au:PVP NPs synthesized in the microreactor using $NaBH_4$, (VII) Au:PVP NPs synthesized in the batch reactor using $NaBH_4$ and (VIII) Au NPs reduced by THPC/NaOH in the batch reactor.

STEM images of all samples show NPs with spherical shape. Particle size distributions were determined by measuring diameters of hundreds of Au NPs (histograms in Fig. 20). The Au:PVP NPs produced in the microfluidic reactor show ultrasmall particle size with 1.0 nm average diameter, whereas the average size of Au:PVP NPs produced in batch reactor using $NaBH_4$ increased to 1.9 nm. Au:PVP NPs produced in the batch reactor exhibit a slightly broader particle size distribution. These results are comparable to those published in earlier works. Tsunoyama et al.[29, 102, 103] produced NPs in a microreactor with an average NP size of 1.3 nm and a slightly narrower size distribution compared to those produced in batch. Au NPs synthesized in batch by THPC/NaOH show the broadest size distribution with an average diameter of 2.8 nm compared to the previous two samples. However, it was also reported that thorough cleaning of the beakers (pre-washed with aqua regia) and freshly dissolved reactants leads to smaller NP sizes (<2.5 nm) and narrower size distributions[3, 90].

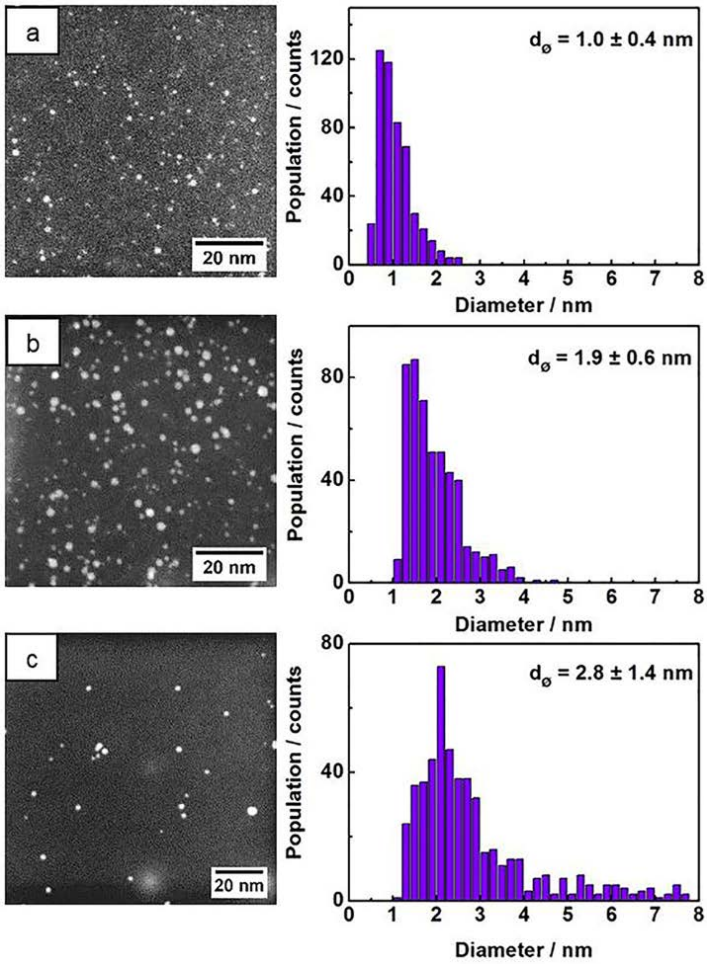

Fig. 20 STEM images and size distributions of 500 NPs of a) Au:PVP NPs produced in the microreactor, b) Au:PVP NPs produced in batch reactor using $NaBH_4$ and c) Au NPs reduced with THPC/NaOH in batch reactor[39].

3.5. Characterization of Supported Au NPs Produced by Microfluidics

The Au:PVP NPs from the microfluidic synthesis were deposited on TiO_2 with 0.7 and 1.7 wt.% Au loading for catalytic activity tests. The morphology and distribution of Au NPs on the TiO_2 support after drying at 80 °C were characterized by STEM and are shown in Fig. 21. The diameters of ca. 600 particles were measured to obtain size distributions revealing an average particle size of around 7.5 nm. The Au NPs were homogeneously distributed on the support and according to the corresponding histograms both catalysts exhibit similar particle size distributions. Deposition of the NPs on titania obviously leads to a significant increase in particle size. It is known that pretreatment of the TiO_2 under different conditions, the deposition method and post-synthetic treatment conditions such as drying and calcination result in different metal-support interactions. In the case of Au/TiO_2, it is proposed that a weak interaction increased the mobility of Au NPs, leading to some extent to aggregation[42].

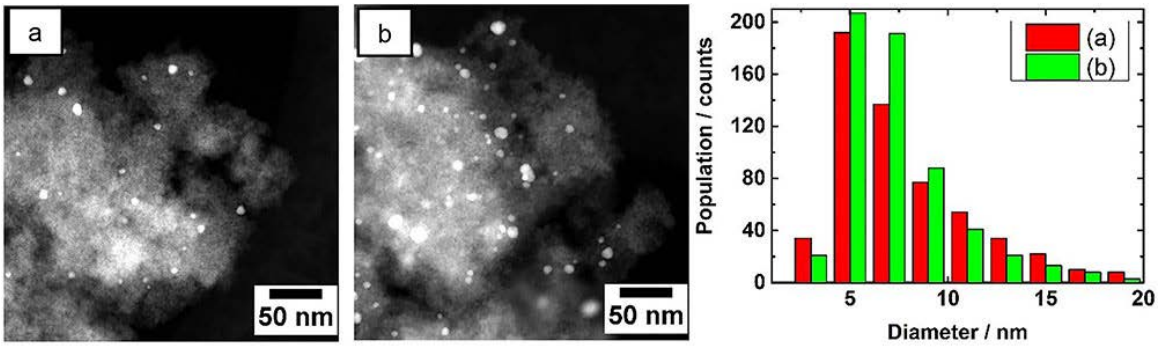

Fig. 21 STEM images of uncalcined a) 0.7 and b) 1.7 wt.% Au:PVP NPs on TiO_2 and size distribution[39].

In order to understand the electronic structures of Au NPs synthesized using different reducing agents/stabilizers the uncalcined NPs were characterized by XPS. The close up XPS spectra of the Au 4f doublets in Fig. 22a show a peak shift to lower binding energies for Au:PVP NPs and also for Au:PVP/TiO_2 samples, but not for Au NPs reduced by THPC. Since for both samples the TiO_2 support and mean Au NP size are comparable, this shift between Au:PVP/TiO_2 and Au:THPC/TiO_2 can be related to the electron transfer between the ligand and gold. The Au $4f_{5/2}$ and Au $4f_{7/2}$ orbitals in bulk state appear at 87.7 and 84 eV, respectively. However, in Au:PVP NPs these peaks appeared at 86.3 and 82.6 eV, respectively. These results indicate that the surfaces of the Au NPs are negatively charged. According to literature[103], this effect is attributed to the electron donating nature of PVP to

gold surfaces. In the case of Au:PVP/TiO_2 samples this shift to lower binding energies was smaller compared to unsupported Au:PVP. Fig. 22b shows the C1s core level for the samples which was used for XPS data calibration (c. f. section 2.2.4.).

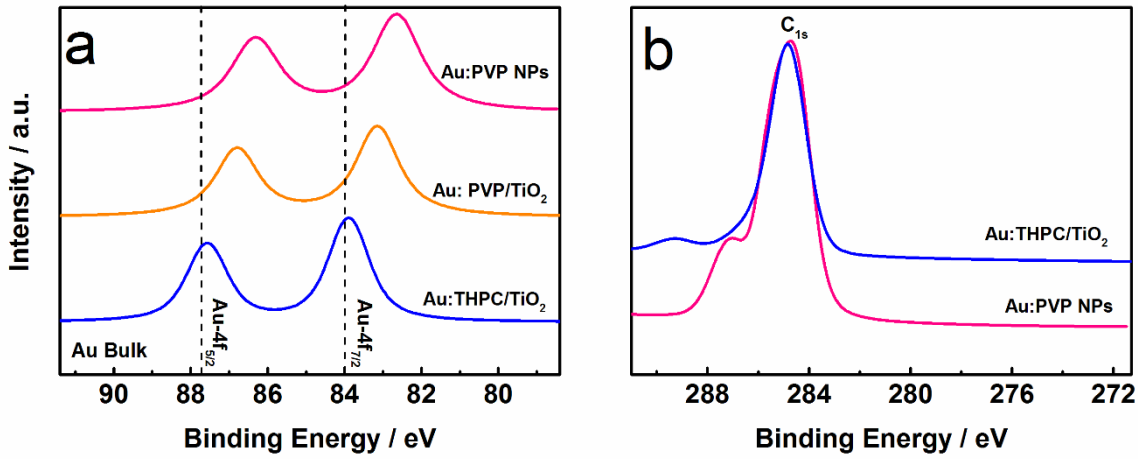

Fig. 22 XPS spectra of the a) Au 4f levels of Au:PVP NPs synthesized in the microfluidic reactor before and after being supported on TiO_2 compared to Au NPs synthesized in a batch reactor (reduced and stabilized by THPC) and b) C 1s level of Au:PVP NPs and Au:THPC NPs supported on titania[39].

The 0.7 wt.% Au:PVP/TiO_2 and 1.7 wt.% Au:PVP/TiO_2 catalysts showed high CO oxidation activity in calcined and uncalcined states considering their rather large Au particle size and the presence of organic surfactants on the catalyst surface (Fig. 23). The catalysts exhibited higher activity after calcination; the uncalcined 0.7 wt.% Au:PVP/TiO_2 sample reached 50% ($T_{1/2}$) and full CO conversion at 98 °C and 166 °C respectively, while after calcination at 300 °C these temperatures shifted to 73 °C and 121 °C for the first reaction cycle. For the uncalcined 1.7 wt.% Au:PVP/TiO_2 sample, 50% and full CO conversion were achieved at 102 °C and 175 °C respectively, while after calcination these temperatures shifted to 91 °C and 140 °C for the first reaction cycle. Accordingly, lower Au loading (0.7 wt.%) and calcined catalysts show the highest activity among these samples. Removal of PVP from Au NPs and sintering, both resulting from calcination, could to some extent play different and competitive roles in the activity of the catalysts. Calcination temperature, particle size, moisture and also the strength of Au-TiO_2 interaction, which depends on the deposition method, are key parameters with respect to catalytic activity. Strong Au-TiO_2 interaction leads to a high number of effective active sites in the perimeter interface of Au and TiO_2 resulting in higher activity in CO oxidation[4,

[9, 12]. In the present work, the mechanical mixing applied to adsorb colloidal Au on the support resulted in well-distributed Au NPs on the titania surfaces but also in aggregation of NPs compared to the colloid. Nevertheless, under conditions such as low Au loading (0.7 and 1.7 wt.%), 7.5 nm mean particle size on titania and presence of PVP, the catalytic activity of the samples in CO oxidation is considerable. Table 3 summarizes the particle sizes of the colloidal Au NPs as well as particle sizes, surface areas and catalytic properties of the Au/TiO_2 catalysts.

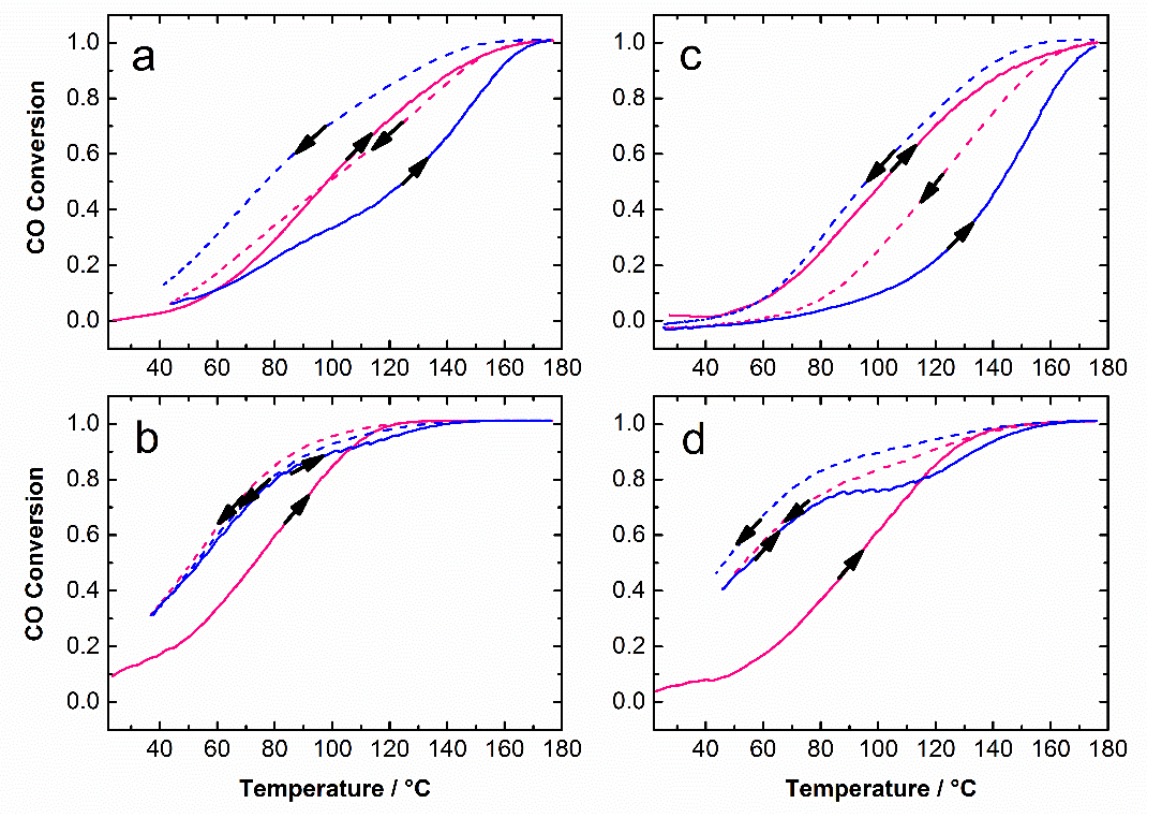

Fig. 23 First cycle (red) and second cycle (blue) of CO oxidation catalyzed by PVP-stabilized Au/TiO_2: uncalcined (a,c) and calcined (b,d); different Au loading of 0.7 wt.% (a,b) and 1.7 wt.% (c,d); Conditions: 400 mg catalyst, 300 mL min^{-1} total flow rate, 1000 ppm CO and 1000 ppm O_2 diluted in nitrogen[39].

Table 3 Characterization of Au NPs

Sample	State	Synthesis method	d_{Au} (nm) STEM	SA (m^2 g^{-1}) BET	$T_{1/2}$ (°C)	
					1st cycle	2nd cycle
Au:PVP NPs	colloid	µ-reactor	1.8±0.5			
Au:PVP NPs	colloid	Batch reactor	1.9±0.6			
Au:THPC NPs	colloid	Batch reactor	2.8±1.4			
0.7wt.%Au:PVP/TiO_2	uncalcined	Au –µ-reactor	7.9±3.9	317	98	125
	calcined	Au –µ-reactor			73	53
1.7wt.%Au:PVP/TiO_2	uncalcined	Au –µ-reactor	7.3±3.0	317	102	143
	calcined	Au –µ-reactor			91	55
TiO_2	uncalcined			329		
	calcined			208		

Before and after calcination and CO oxidation tests the catalysts were characterized by XRD. The diffractograms confirm the presence of an anatase phase of titania. In the XRD data of uncalcined 0.7 and 1.7 wt.% Au:PVP/TiO_2 catalysts gold reflections[3, 104] were not observed. Nevertheless, after calcination the gold reflections clearly appeared in the diffractogram of the 1.7 wt.% Au:PVP/TiO_2 catalyst (Fig. 24), probably caused by sintering due to higher gold concentration in this sample. This could explain the lower CO oxidation activity of the 1.7 wt.% Au:PVP/TiO_2 catalyst after calcination compared to 0.7 wt.% Au:PVP/TiO_2.

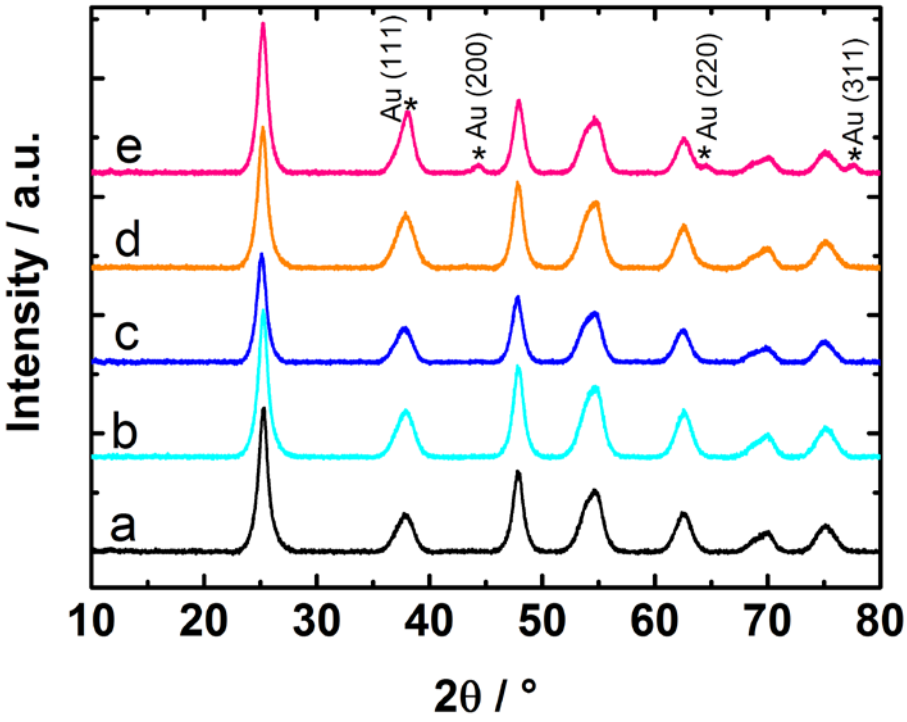

Fig. 24 XRD patterns of catalysts before and after calcination and CO oxidation; a) pure TiO_2, b) uncalcined 0.7 wt.% Au:PVP/TiO_2, c) calcined 0.7 wt.% Au:PVP/TiO_2, d) uncalcined 1.7 wt.% Au:PVP/TiO_2 and e) calcined 1.7 wt.% Au:PVP/TiO_2[39].

3.6. Conclusion

A novel microfluidic setup was built for advanced synthesis of ultrasmall nanoparticles with narrow size distribution in fast continuous flow at Reynolds numbers up to 2400 and for *in situ* spatially and time resolved studies of early stage kinetics of fast reactions. Three cyclone micromixers integrated in the chip allow achieving mixing times down to 2 ms. This setup was used to study Au NP formation using *in situ* XAS during Au^{3+} reduction to Au^0 by $NaBH_4$ in the presence of PVP. In the future the apparatus may also be used for other spectroscopic and scattering techniques. The reaction progress under continuous flow was monitored by recording XAS spectra at different positions along the microchannel with a focused X-ray beam. The results revealed that up to 6 ms there is still a significant contribution of oxidized Au. The reduction to Au^0 was complete within the first 10 ms of this fast reduction reaction and remained unchanged at 18 ms.

Au:PVP NPs synthesized in the microfluidic chip were characterized by complementary techniques (UV-vis, TEM, XPS and XRD) and compared to Au:PVP NPs and Au/THPC NPs synthesized in batch reactor. The average size of Au:PVP NPs from microfluidic synthesis was 1.0 ± 0.4 nm with a narrower size distribution. These NPs also showed a stronger suppression of the SPR band in UV-vis spectra. In accordance with earlier works, the addition of PVP as stabilizer transferred negative electric charges to the Au surfaces, leading to a decrease in Au 4f binding energies in XPS spectra.

Au:PVP NPs produced using the microfluidic setup were also deposited on titania. The catalysts thus obtained were quite active in CO oxidation. Under the same conditions the calcined 0.7 wt.% Au:PVP/TiO_2 sample was more active compared to the corresponding uncalcined catalysts with higher Au loading. According to XRD data, in the 1.7 wt.% Au:PVP/TiO_2 sample calcined at 300 °C sintering of NPs occurred. The results of these experiments indicate that the supported Au NPs produced from this microfluidic setup are not only suitable for *in situ* studies of NP formation but may also be attractive for catalytic and sensing applications.

The next chapter describes how the microfluidic synthesis of ultrasmall NPs was expanded to produce monometallic Pd and homogeneous alloys of AuPd NPs, which were characterized by various techniques and tested for CO oxidation.

4. Ultrasmall and Homogeneous AuPd Nanoalloys[2]

Chapter 3 demonstrated the successful application of a novel microfluidic reactor in the synthesis of ultrasmall Au NPs and kinetic studies of early stages of a fast reduction reaction during formation of these monometallic NPs, which were also catalytically tested with respect to CO oxidation. The following chapter describes how the microfluidic setup proved to be of high value for synthesis of bimetallic systems, in this case ultrasmall AuPd alloyed NPs.

4.1. Introduction

Small and highly dispersed NPs of transition metals have received growing attention in the context of nanoscience and nanotechnology in catalysis[17, 31, 102, 105-107], sensing[108-110], electronics and optics[111-113], imaging and biology[114-116], due to their high surface area and size dependent properties. Introducing bimetallic systems for such applications provides new opportunities to improve the performance of the materials by combining both metals´ properties and, in some cases, achieving synergistic effects. These improvements originate from tunable electronic interactions and geometric structures of NPs and also metal-support interactions in the case of supported catalysts[17, 117, 118]. The reasons for catalytic synergistic effects are hard to be explained based on literature comparison due to the differences in synthesis methods and its applied conditions, surface composition of the NPs, inhomogeneous NP size distribution and the insufficient in-depth structural characterization of the bimetallic NPs.

The formation of colloidal metal NPs via chemical reduction reactions, which is one of the most straightforward methods, proceeds in the four following steps: (1) mixing and diffusion of metal precursors and reducing agents, (2) reduction of metal ions to atoms, (3) nucleation and (4) growth of NPs[45, 117]. In conventional stirred batch reactors, inefficient mixing conditions lead to concentration gradients of reactants in the medium and poor control over the reaction conditions, resulting in polydisperse NPs with properties deviating from the desired ones. Controlling this issue gets even more complicated in case of bimetallics (especially solid-solution alloys) having two metals with different redox potentials (successive reduction)[17, 60, 119].

[2] Part of this chapter has been published in Journal of Physical Chemistry C[132].

The reaction conditions can be controlled microscopically using microfluidic reactors, allowing spatially and temporarily homogeneous mixing of metal precursors and reducing agents on a very short time scale (ms) and separating the nucleation and growth steps from each other, leading to narrow NP size distributions[29, 39, 53, 56]. Moreover, this technology allows a precisely controlled temperature profile over different steps of the reaction, e.g. warming up the microchannels at the beginning of the reaction to facilitate the nucleation, and cooling down the products after the microfluidic device to control the growth of NPs, ending up with highly monodisperse bimetallic nanoclusters (Hayashi et al.[117]). Recently, *in situ* spectroscopic and scattering studies during the formation of NPs in microfluidic channels have added up to the advantages of microfluidic technology. The latter case shows the importance of understanding the intermediates involved in during synthesis and optimization of the reactions to obtain high quality nanomaterials[46, 47, 49].

Bimetallic AuPd systems have attracted growing attention with respect to catalytic applications such as direct synthesis of hydrogen peroxide[120-122], alcohol and glucose oxidation[123-125], oxidation of primary C-H bonds[126] and CO oxidation[127-129]. Literature shows an improvement in catalytic activity, selectivity and durability of Pd when alloyed with Au[17]. Furthermore, since Au and Pd are miscible in all composition ratios, it is possible to tune the interatomic distances in AuPd in order to adjust the distances between the adsorption sites to the benefit of catalytic performance in structure-sensitive reactions[130, 131]. This highlights the necessity of establishing a synthesis technique with high control over the production quality and minimized random nucleation and growth, therefore yielding uniform alloyed compositions of bimetallic NPs.

For this study, the microfluidic device was used to synthesize highly monodispersed ultrasmall (1-2 nm) AuPd NPs with homogeneously mixed alloy structures stabilized with polyvinylpyrrolidone (PVP) under flow conditions approaching turbulent mixing and plug flow. The presence of homogeneously mixed nanoalloys was confirmed by various complementary characterization techniques such as X-ray absorption spectroscopy (XAS) in terms of X-ray absorption near edge structures (XANES) and extended X-ray absorption fine structures (EXAFS), high resolution transmission electron microscopy (HRTEM), energy-dispersive X-ray spectroscopy (EDX), UV-visible spectroscopy (UV-vis) and inductively coupled plasma-optical emission spectroscopy (ICP-OES). The NPs were supported on TiO_2 and the resulting Au/TiO_2, Pd/TiO_2 and Au_xPd_y/TiO_2 catalysts were tested for CO oxidation to demonstrate their potential application in catalysis.

4.2. Colloidal Synthesis Procedure and Catalyst Preparation

4.2.1 Materials

Tetrachloroauric (III) acid ($HAuCl_4 \cdot 3H_2O$, Roth, 99.5% purity), potassium tetrachloro palladate (II) (K_2PdCl_4, Alfa Aesar, 99.99% purity), polyvinylpyrrolidone (PVP, $(C_6H_9ON)_x$, Sigma-Aldrich, average molecular weight 40 kDa), sodium borohydride ($NaBH_4$, Sigma-Aldrich, 99.99% purity), sulphuric acid (H_2SO_4, Sigma-Aldrich, 95% solution) and high surface area titania (TiO_2, CristalACTIV^{TM}, >99% purity, anatase, 370 $m^2\ g^{-1}$ surface area) were used without further purification.

4.2.2 Microfluidic Synthesis of Au, Pd and Au_xPd_y NPs Reduced by $NaBH_4$

In order to synthesize highly monodisperse monometallic and bimetallic NPs via fast reduction reactions, the microfluidic setup capable of generating a continuous and pulsation-free flow of reactants at high flow rates was used (Fig. 25 and more details cf. Section 2.1.). The vessels of fluid delivery rack were pressurized by 13 bar N_2 gas to deliver the reactants at 2.6 L h^{-1} total flow rate to three cyclone micromixers integrated in a microfluidic chip for fast (2 ms) and homogeneous mixing. For each reactant, a flow rate of 1.3 L h^{-1} (total flow rate 2.6 L h^{-1}) was required to achieve Reynolds number exceeding 2400 in order to approach turbulent mixing within 2 ms, which is necessary for fast reduction reactions. The total residence time of the reactants in the microchannel was about 20 ms.

Table 4 summarizes the preparation conditions of the reactant solutions for synthesis of Au, Pd and Au_xPd_y NPs (x, y: molar ratio of Au and Pd with x + y = 10). Aqueous solutions of $HAuCl_4$ and K_2PdCl_4 precursors were prepared with a constant total metal precursor concentration (7.5 mM) for all samples. An aqueous solution of $NaBH_4$ (37.5 mM) was prepared in a separate flask. Afterwards, 666 mg PVP was added to each of these two solutions as stabilizer, a procedure adopted from Hayashi et al[117]. Prior to the microfluidic synthesis, the microchannel was flushed with aqua regia, and then several times purged with deionized water to remove impurities. The metal precursor and $NaBH_4$ solutions were filled into the vessels of the fluid delivery rack (Fig. 25). N_2 gas was applied to drive the reactants through the inlet channels at a total flow rate of 2.6 L h^{-1} in order to achieve turbulent flow conditions in the micromixers for efficient mixing of the reactants. The products were collected and stirred for 1 h in a round-bottom flask placed in an ice/water bath.

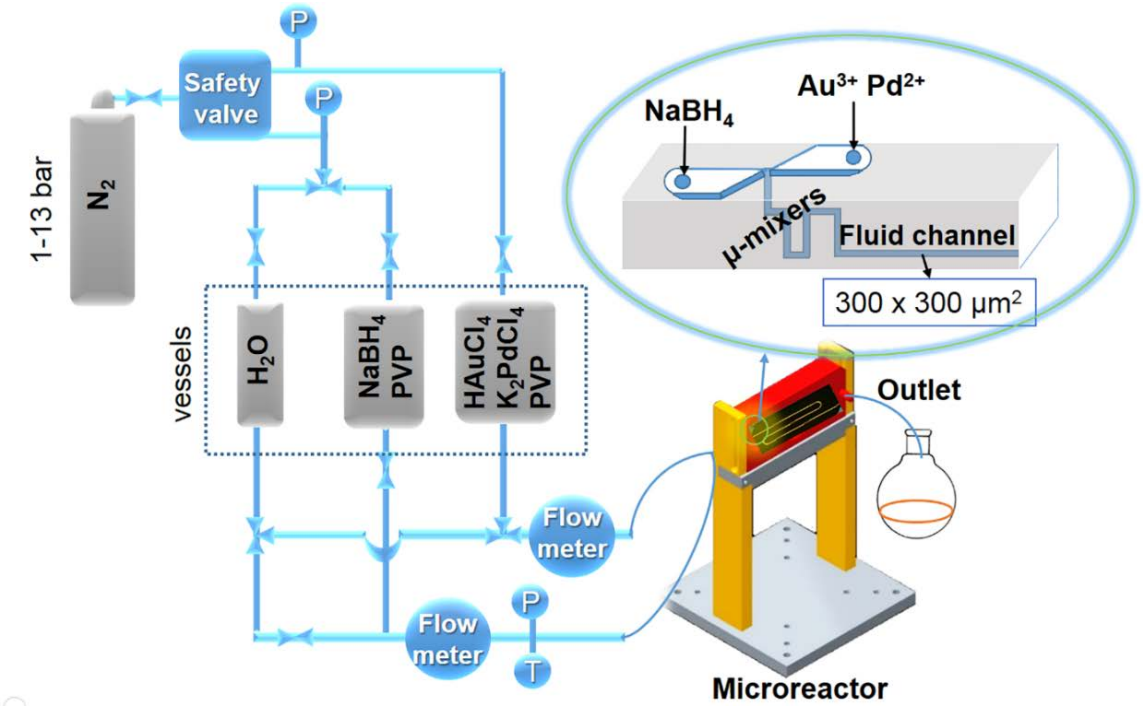

Fig. 25 Schematic of the microfluidic setup employed for synthesis of PVP-stabilized monometallic and bimetallic NPs in continuous flow (P, T: pressure transducer and temperature sensor), inset: schematic of the inlets and micromixers in the chip to achieve homogeneous mixing[132].

Table 4 Microfluidic synthesis conditions for Au, Pd and Au_xPd_y:PVP colloids.

Sample	Solution A[a]		Solution B[b]
	$HAuCl_4$ (mg)	K_2PdCl_4 (mg)	$NaBH_4$ (mg)
Au	236.4	0.0	114
Au_7Pd_3	165.5	58.7	114
Au_5Pd_5	118.2	97.9	114
Au_3Pd_7	71	137	114
Pd	0.0	200	114

a)7.5 mM aqueous solution with 666 mg PVP, b)37.5 mM aqueous solution with 666 mg PVP

4.2.3 Batch Synthesis of AuPd:PVP NPs Reduced by $NaBH_4$

The same molar metal:$NaBH_4$ ratio used for the microfluidic synthesis of NPs was applied in batch synthesis of Au_7Pd_3 and Au_3Pd_7 NPs to compare their size distributions with those of the materials produced in the microfluidic reactor (summarized in Table 5). The gold and palladium precursors and 166.6 mg PVP were dissolved in 60 mL deionized water. 28.5 mg $NaBH_4$ and 166.6 mg PVP were dissolved in 15 mL deionized water and added to gold precursor solution stirred rapidly at room temperature. The fast reduction reaction was observed through a color change.

Table 5 Conventional batch synthesis conditions for selected Au_xPd_y:PVP colloids.

Sample	Solution A[a]		Solution B[b]
	$HAuCl_4$ (mg)	**K_2PdCl_4 (mg)**	**$NaBH_4$ (mg)**
Au_7Pd_3	41.4	14.7	28.5
Au_3Pd_7	17.7	34.2	28.5

a)2.5 mM aqueous solution with 166.6 mg PVP, b)50.2 mM aqueous solution with 166.6 mg PVP

4.2.4 Preparation of Au/TiO_2, Pd/TiO_2 and Au_xPd_y/TiO_2 Catalysts

The PVP-stabilized Au_xPd_y colloidal solutions synthesized in the microfluidic reactor were added to 1 g TiO_2 suspended in 80 mL deionized water in an ultrasonic bath at room temperature and stirred for one hour. Prior to the impregnation of TiO_2 with NPs, the titania support was acidified with 8 mL H_2SO_4 solution (0.2 M), decreasing the suspension pH to 2. After 1 h of stirring, the suspension was centrifuged four times (4500 rpm, 5 min each) and washed with water in between. Eventually, the catalysts were dried at 80 °C overnight and calcined at 380 °C for 3 h. This method was applied for preparing 1.0 and 2.4 wt.% Au_xPd_y/TiO_2 as well as monometallic Au and Pd NPs on TiO_2.

4.3. Characterization of Colloidal Au, Pd and AuPd NPs

STEM images of monometallic Au, Pd and bimetallic Au_xPd_y colloids in Fig. 26 prove the formation of spherical ultrasmall NPs (average diameter ~ 1 nm). The corresponding histograms clearly show that highly monodisperse metal NPs were produced by mixing the metal precursors, PVP and $NaBH_4$ in the microfluidic reactor. STEM images of two selected bimetallics of Au_7Pd_3 and Au_3Pd_7 produced in conventional batch reactor (Fig. 27) clearly show broader size distributions with average particle sizes of 1.4 nm and 1.6 nm, respectively. These results are comparable to those reported by Hayashi et al.[117], who also showed that microfluidic synthesis is superior to batch reactor synthesis in terms of achieving a controlled size and narrow size distribution of Au_xPd_y NPs. These benefits originate from fast mixing of the reactants and controlling the initial states of nucleation and growth in the microfluidic reactors. According to literature[50, 51, 117, 133], the reduction process of metal ions in the microfluidic reactors equipped with micromixers is more homogeneous in shorter time intervals, and liberation of metal atoms with oxidation state zero is much faster compared to synthesis in conventional stirred batch reactors. This is due to the fast molecular diffusion processes occurring in the microfluidic reactor compared to batch reactors which first require dissociation of the reactant solutions into tiny fractions and subsequent domination of the molecular diffusion mechanism. Therefore, in the batch

reactors the initially-formed NPs consume the available metal atoms in the solution to grow, and the newly-formed NPs remain small due to the absence or low concentration of metal atoms which finally results in broader size distributions.

The HRTEM images of Au_xPd_y NPs in Fig. 28 show a crystal-like structure and the absence of other structures such as core-shell or segregated subcluter. The measured lattice spacings (red marks in Fig. 28) for Au_xPd_y NPs ranged between 2.35 Å (Au (111)) and 2.24 Å (Pd (111))[134, 135]. This indicates that a uniform distribution/mixing of Au/Pd precursors and reducing agent was achieved by approaching turbulent mixing conditions using the cyclone micromixers, resulting in the formation of colloidal Au_xPd_y nanoalloy structures. According to HRTEM analysis of about 10-20 particles, the lattice parameters change upon changes in composition in agreement with Vegard's law. The average unit cell parameters for Au_3Pd_7, Au_5Pd_5 and Au_7Pd_3 were 4.015 Å, 4.020 Å and 4.041 Å, respectively. This trend indicates that homogeneous alloys are formed following Vegard's law.

Fig. 29 shows STEM images of PVP-stabilized Au_7Pd_3, Au_5Pd_5 and Au_3Pd_7 colloids and the composition maps obtained from STEM-EDX spectrum imaging within a single NP. According to the composition maps, Au and Pd are uniformly distributed in the investigated representative particle for all three bimetallic Au_xPd_y colloids. HRTEM analysis and the composition maps demonstrate that Au-Pd alloy NPs were formed in the three bimetallic Au_xPd_y colloids produced in the microfluidic reactor.

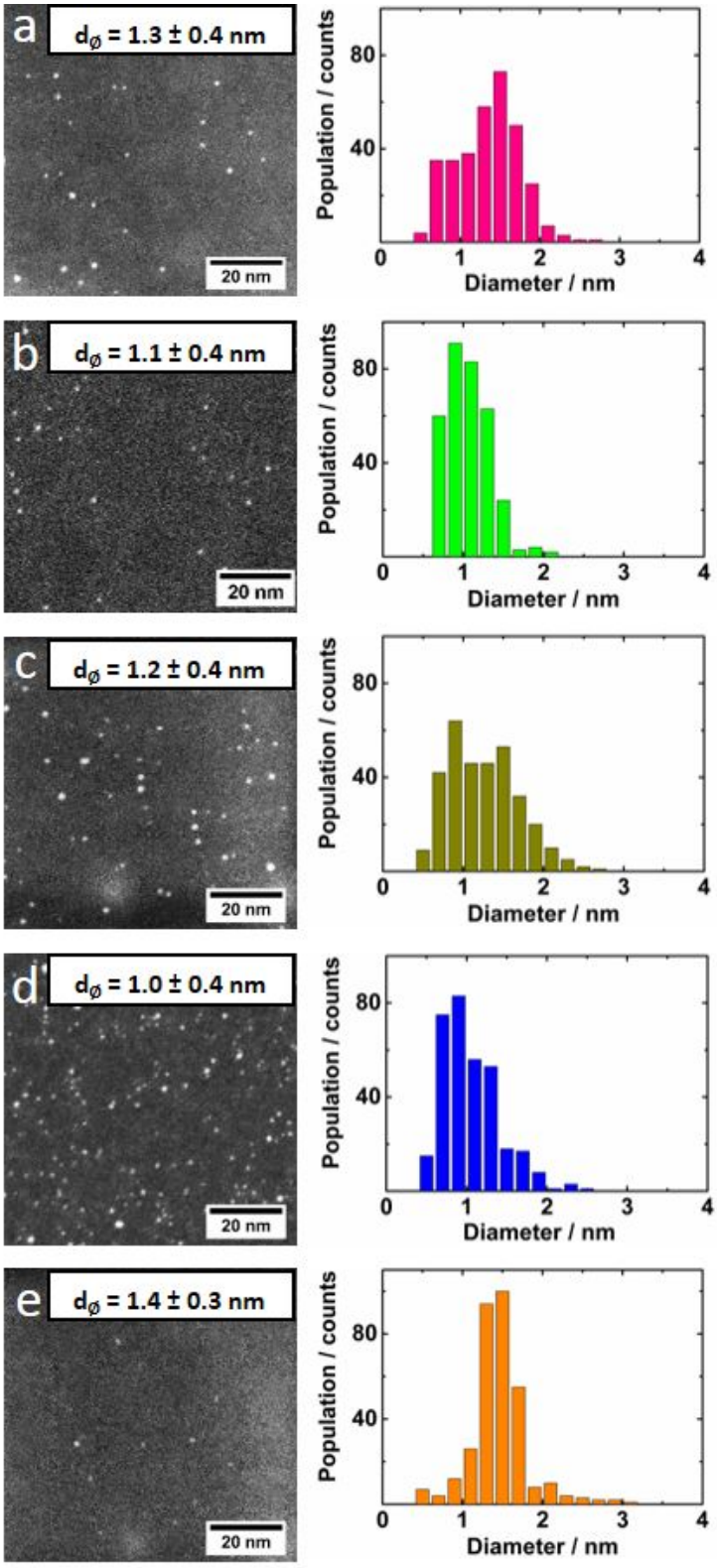

Fig. 26 STEM images and size distributions of PVP-stabilized a) Au_7Pd_3, b) Au_5Pd_5, c) Au_3Pd_7, d) Au and e) Pd NPs produced in the microfluidic reactor (330 particles analyzed for each size distribution)[132].

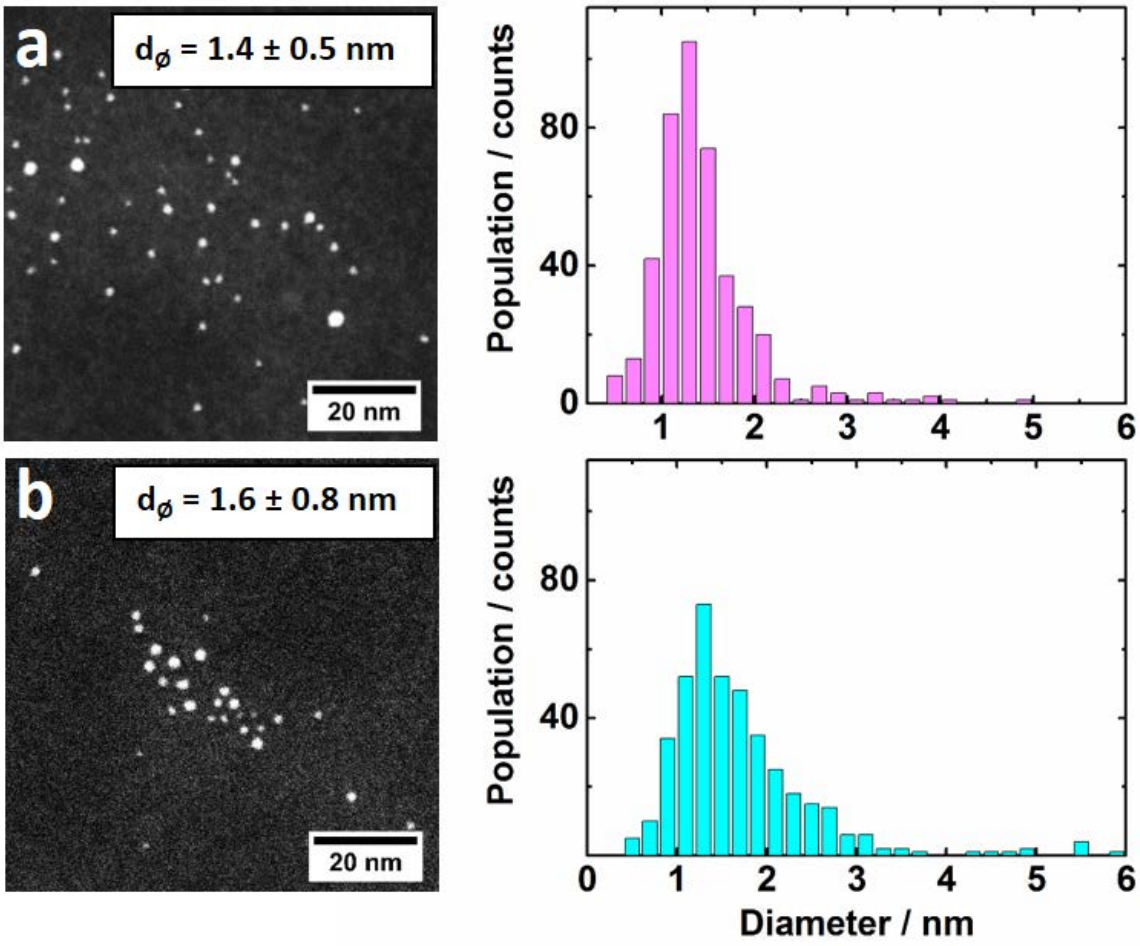

Fig. 27 STEM images and size distributions of PVP-stabilized a) Au_7Pd_3 and b) Au_3Pd_7 NPs produced in the batch reactor (ca. 400 particle diameters analyzed for each size distribution)[132].

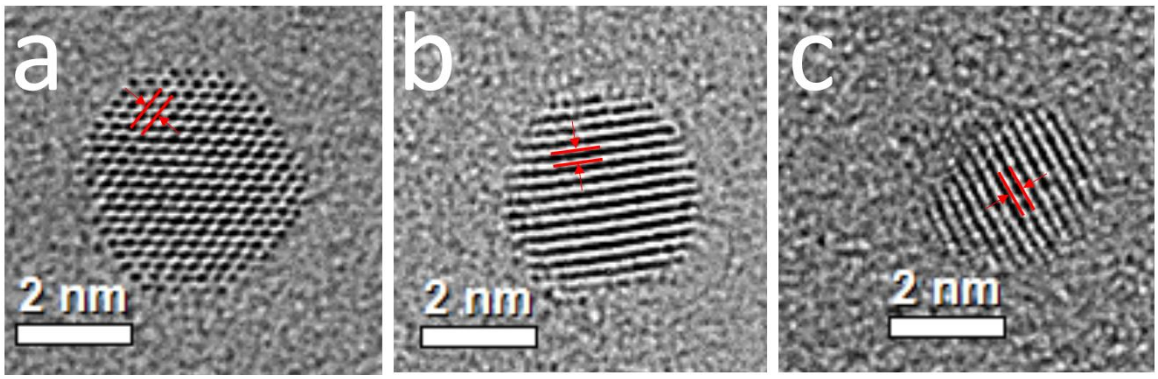

Fig. 28 HRTEM images of PVP-stabilized a) Au_7Pd_3, b) Au_5Pd_5 and c) Au_3Pd_7 NPs produced in the microfluidic reactor. The d-spacing is marked by red lines[132].

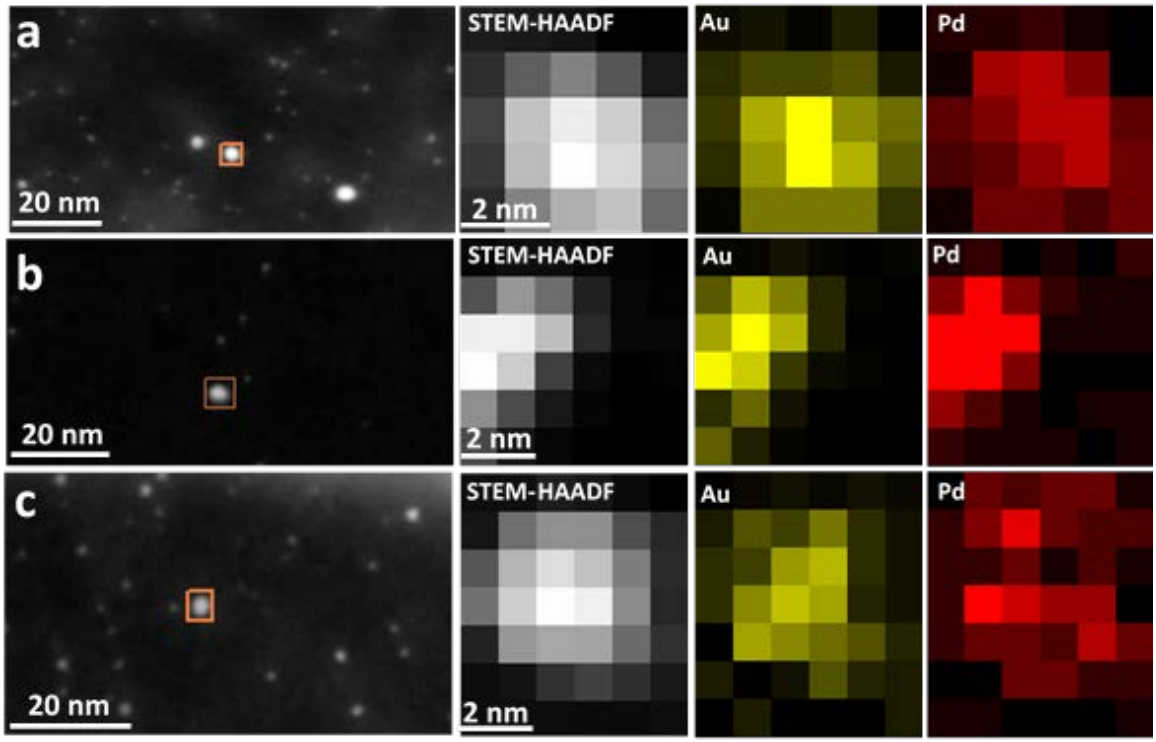

Fig. 29 STEM images of PVP-stabilized a) Au_7Pd_3, b) Au_5Pd_5 and c) Au_3Pd_7 colloids and the corresponding element maps obtained from STEM-EDX spectrum imaging in the areas marked by orange boxes[132].

The formation of ultrasmall Au, Pd and Au_xPd_y colloidal NPs was also confirmed by UV-vis spectroscopy (Fig. 30). The measured spectra indicate a strong suppression of surface plasmon resonance (SPR) of gold highlighting dominance of surface scattering from NPs with diameters below 3 nm[3, 29, 79]. Furthermore, since the total concentrations of metal atoms in all samples were almost equal, the absorption behavior changes with different Au:Pd molar ratio. At higher wavelengths (above 500 nm), the absorption increases with increasing Pd content in the NPs presumably due to overlapping 4d → 5sp and 5sp → 5sp transitions which typically occur in pure Pd, and intraband 6sp → 6sp transitions in pure gold (wavelengths above 400 nm)[117, 136]. Moreover, the absence of the absorption peak of palladium chloride at 425 nm suggests full reduction of the Pd precursor to metallic Pd[137]. At lower wavelengths (below 500 nm) the absorption increases with increasing Au amount in the NPs, indicating interband 5d → 6sp transitions in pure gold[117, 138-140]. These results indicate different electronic structures of NPs with changing Au:Pd molar ratios.

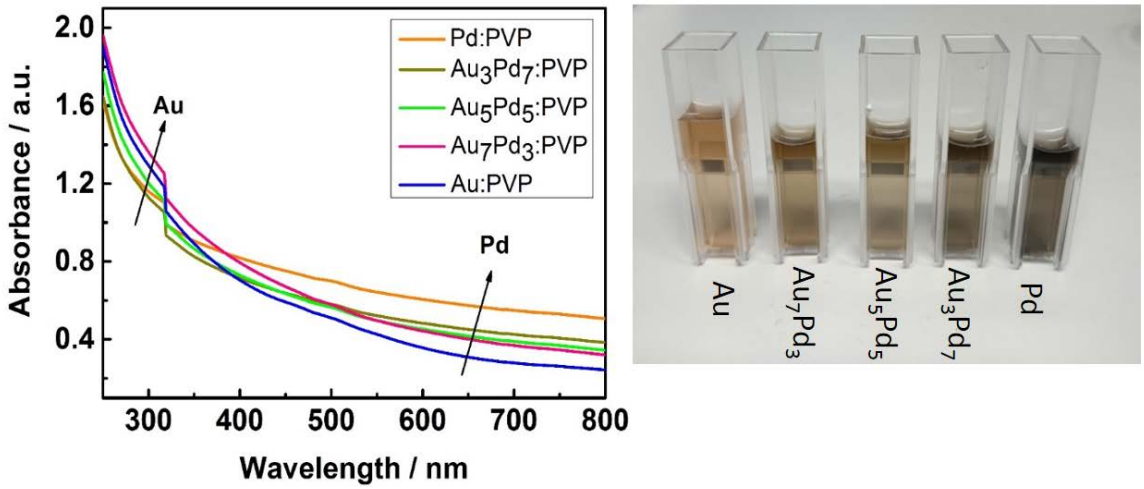

Fig. 30 UV-vis spectra and image of monometallic Au and Pd and bimetallic Au_xPd_y NP colloids produced in the microfluidic reactor[132]. The abrupt increase in the spectra at 319 nm is related to switching between deuterium and tungsten lamps.

4.4. Homogeneity of Au_xPd_Y Nanoalloys Supported on TiO_2

The colloidal NPs produced in the microreactor were deposited on TiO_2 powder with 1 wt.% total metal (Au+Pd) loading for CO oxidation tests and 2.4 wt.% total metal loading as pellets for XAS measurements to investigate the structure and homogeneity of AuPd nanoalloys. The elemental compositions of selected Au_xPd_y/TiO_2 catalysts obtained from ICP-OES are given in Table 6. These values are in good agreement with the target Au:Pd molar ratios during colloidal synthesis and the desired metal loadings of the supported catalysts for CO oxidation and *ex situ* XAS.

The particle morphology and size distribution of the nanoalloys after calcination at 380 °C were studied by STEM (Fig. 31). Size distributions were determined by measuring the diameters of hundreds of particles giving an average diameter of ca. 5.3, 4.9 and 7.3 nm for Au_7Pd_3, Au_5Pd_5 and Au_3Pd_7, respectively. Obviously, deposition on TiO_2 and calcination leads to a significant increase in NP size. Different phases, surface area and pretreatment of the support, deposition method and applied conditions as well as post-treatments such as calcination have been known to play an important role in NP aggregation and to cause different interaction between the metal NPs and the ceramic supports, which can influence the catalytic performance[42].

Table 6 ICP-OES results for Au_xPd_y/TiO_2 catalysts

	1* wt.% Au_3Pd_7/TiO_2 (wt.%)	3* wt.% Au_3Pd_7/TiO_2 (wt.%)	3* wt.% Au_5Pd_5/TiO_2 (wt.%)
Au	0.41	1.04	1.34
Pd	0.55	1.41	0.94
Total metal loading	0.96	2.45	2.28
Au:Pd molar ratio	2:5	2:5	5:6

*: nominal value

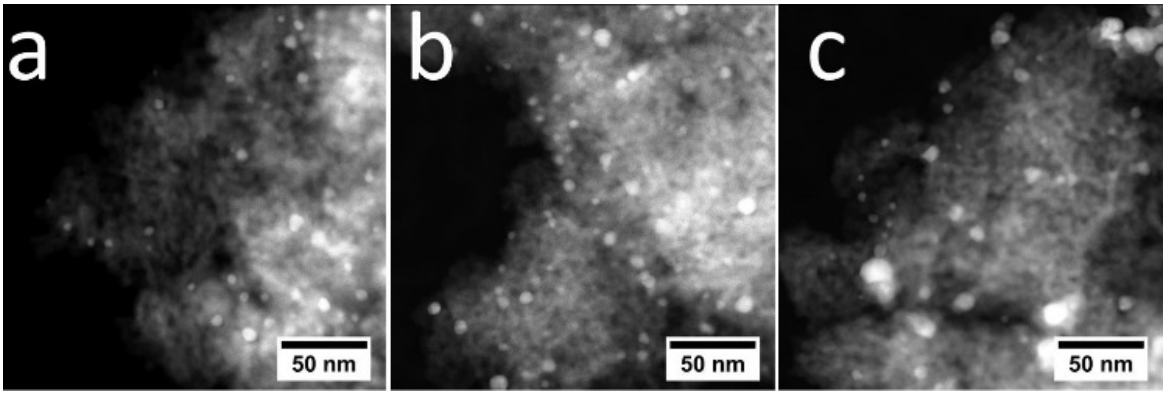

Fig. 31 STEM images of calcined a) Au_7Pd_3/TiO_2, b) Au_5Pd_5/TiO_2 and c) Au_3Pd_7/TiO_2[132].

Fig. 32 shows k^3-weighted and Fourier-transformed (FT) Au L_3 EXAFS data of the 2.4 wt.% Au_xPd_y and Au NPs deposited on TiO_2 along with the corresponding XANES spectra. The EXAFS oscillations of Au_xPd_y NPs differ significantly from those of Au foil indicating the presence of an alloy phase. This observation leads to the conclusion that decreasing Au (i.e. increasing Pd) concentration in the bimetallic NPs leads to an increase in the average number of Pd neighboring atoms surrounding the Au absorber atoms, i.e. an increase in Au–Pd bonds. The FT data also follow the same trend in which the Au_xPd_y NPs show intense peaks, at 2.0–2.2 Å and 2.6–2.9 Å. These peaks both correspond to the first shell metal–metal contribution[118]. The splitting of the first shell peak arises from interference between Au–Au and Au–Pd backscattering, with different phase shift and amplitude[118, 131]. With decreasing Au content, the intensity of the lower-R peak increases indicating a growing number of Au-Pd bonds. Furthermore, the peak shift toward shorter distances with the decreasing amount of Au in the alloyed compositions suggests that more gold atoms are now coordinated to palladium, which is in accordance with the linear dependence of lattice parameters on the ratio of the two metals in bimetallic alloys (Vegard's law)[131, 141]. The structural parameters obtained from fitting EXAFS data of the bimetallic Au_xPd_y NPs at the Au L_3-edge are presented in Table 7.

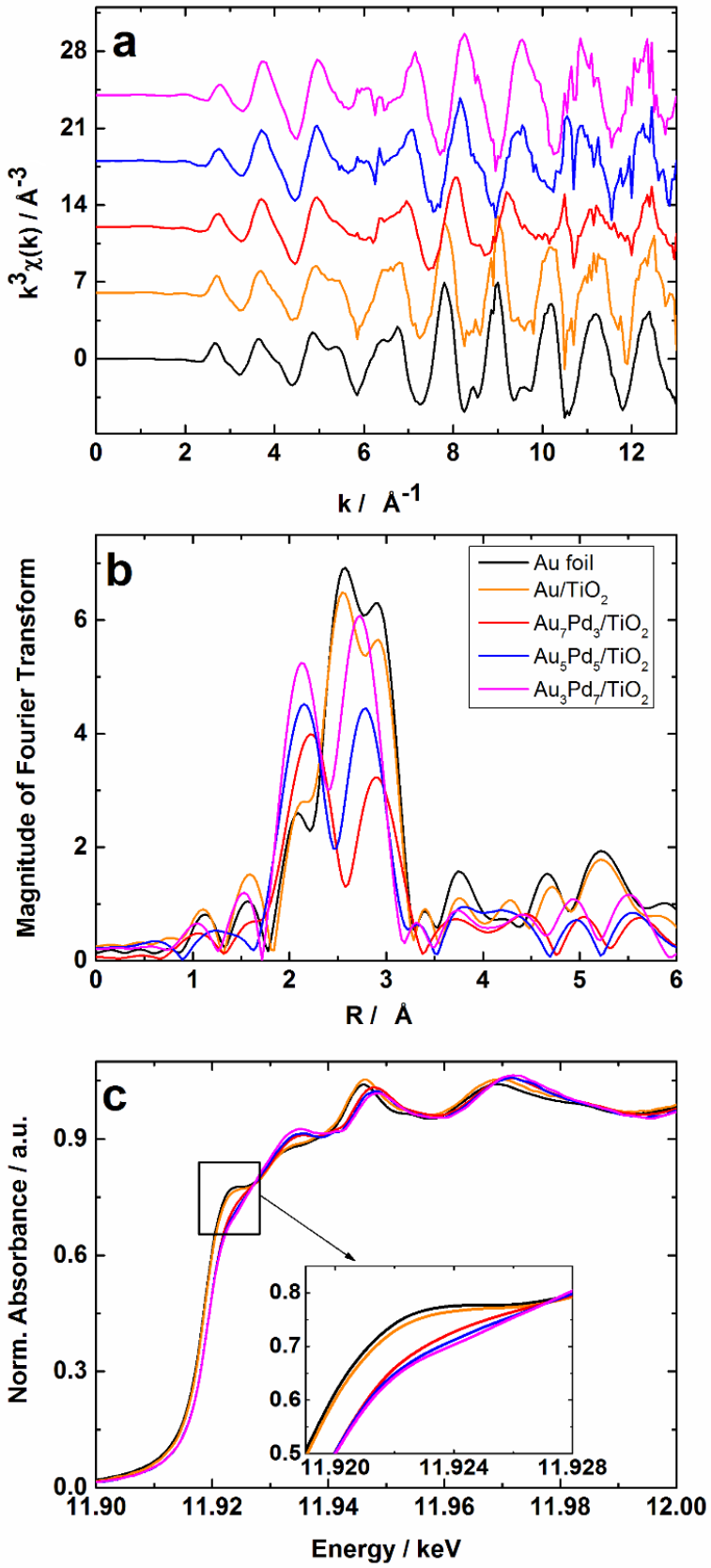

Fig. 32 XAS measurements at the Au L_3-edge on Au/TiO_2 and Au_xPd_y/TiO_2: a) k^3-weighted EXAFS oscillations, b) magnitude of the Fourier-transformed EXAFS data in R-space, and c) XANES spectra (inset: magnified image of the white line region)[132].

Table 7 EXAFS fitting results obtained from Au L_3-edge absorption spectra of Au/TiO_2 and Au_xPd_y/TiO_2; (N: Coordination number, R: Distance (Å), σ^2: Debye–Waller factor ($Å^2$), ΔE_0: Inner core correction, $S_0^2 = 0.72 \pm 0.03$: amplitude reduction factor)

Sample	N_{Au-Au}	**R (Å)**	σ^2 (10^{-3} $Å^2$)	N_{Au-Pd}	**R (Å)**	σ^2 (10^{-3} $Å^2$)	ΔE_0(eV)	N_{Total}
Au foil	12	2.85±0.03	7.7±0.3	-	-	-	-4.3±0.0	12
Au/TiO_2	12.9±1.1	2.85±0.03	8.6±0.5	-	-	-	-5.7±0.7	12.9
Au_7Pd_3/TiO_2	9.4±1.0	2.81±0.07	8.5±0.7	3.3±0.7	2.78±0.03	7.4±1.1	4.1±0.7	12.7
Au_5Pd_5/TiO_2	7.2±1.3	2.81±0.07	8.5±0.7[f]	5.0±1.5	2.79±0.03	6.3±1.6	4.5±1.4	12.2
Au_3Pd_7/TiO_2	5.7±0.8	2.79±0.10	8.5±0.7[f]	6.5±0.9	2.77±0.01	6.5±0.8	4.5±0.7	12.2

[f]: fixed during fitting

The coordination number (N) in bulk fcc metals (e.g. Au and Pd) is 12. In case of bimetallic Au_xPd_y NPs, two types of coordination numbers are obtained from the Au L_3-EXAFS data: $N_{Au–Au}$ and $N_{Au–Pd}$. For Au_xPd_y NPs with homogeneous mixed alloy structure, the ratio of $N_{Au–Au}$ to $N_{Au–Pd}$ should be close to the molar ratio of Au:Pd in the NPs, whereas, $N_{Au–Au}$ to $N_{Au–Pd}$ ratios smaller than the Au:Pd molar ratios indicate inhomogeneous alloying mixture[118]. Moreover, the value of N_{Total} (i.e., $N_{Au–Au} + N_{Au–Pd}$) can also provide information about the structure of the bimetallic NPs.

Based on this discussion, the alloy structure of Au_xPd_y NPs can be explained. From the values of coordination numbers (N) reported in Table 7, it can be concluded that homogeneous mixed nanoalloys were formed for all the bimetallic Au_xPd_y NPs as for the three Au_xPd_y samples the $N_{Au–Au}$ / $N_{Au–Pd}$ ratios are comparable to the corresponding Au:Pd molar ratios. The $N_{Au–Au}$ / $N_{Au–Pd}$ ratios are 2.3, 1.4 and 0.87 and the corresponding molar ratios are 2.5, 1 and 0.42 for Au_7Pd_3, Au_5Pd_5 and Au_3Pd_7, respectively. Hence the core of the particles is slightly enriched in Au.

$N_{Au–Au}$ decreases from 9.4 for Au_7Pd_3 to 7.2 for Au_5Pd_5 and then finally to 5.7 for Au_3Pd_7. A reverse trend was observed for $N_{Au–Pd}$, as it increases from 3.3 for Au_7Pd_3 to 5.0 for Au_5Pd_5 and then finally 6.5 for Au_3Pd_7. N_{Total} is close to 12 for all samples indicating that there is no significant contribution of surface Au atoms to the EXAFS signal. The Au–Au distance also decreases from 2.81 Å (in Au_7Pd_3) to 2.79 (in Au_3Pd_7) showing that the influence of the shorter Pd-Pd length grows stronger with increasing Pd content.

Fig. 32c shows XANES spectra of the Au/TiO_2 and Au_xPd_y/TiO_2 catalysts at Au L_3-edge. The first strong resonance in the spectra (white line)[142, 143] is due to the electronic transition $2p \rightarrow 5d$. The intensity of the white line increases if there are more unoccupied 5d states (d-holes). In bulk Au 5d electrons are transferred to s–p states due to s–p–d hybridization,

while in case of Au NPs, decrease in NP size leads to narrower 5d bands and less s–p–d hybridization[131]. In Fig. 32c-inset, the white line intensities of bulk Au, monometallic Au NPs and the three bimetallic Au_xPd_y NPs supported on TiO_2 are compared. The white line intensity decreases in the order of bulk Au > Au NPs > Au_7Pd_3 NPs > Au_5Pd_5 NPs > Au_3Pd_7 NPs, which shows that the number of d-holes decreases with decreasing particle size and concentration of Au (i.e. increasing Pd concentration).

For bimetallic Au_xPd_y NPs, Liu et al.[118] have discussed the effect of size and alloying on the white line intensity at the Au L_3-edge. Using FEFF 8 simulations of Au L_3-edge XANES spectra, they showed that the white line intensities decreases in the order of bulk Au > Au55 > Au55@Pd. Based on the obtained results, it has been proposed that the Au–Pd alloying effect has a stronger influence on the decrease in white line intensity compared to the size effect. In the present Au_xPd_y samples also the white line intensity decreases with increasing percentage of Pd which corresponds to a higher degree of alloying between Au and Pd. This result can be further augmented from EXAFS analysis where the rise in $N_{Au\text{-}Pd}$ with increasing Pd content indicates a higher degree of alloying.

The Pd K-edge EXAFS spectra of Au_xPd_y/TiO_2 along with spectra of Pd/TiO_2 and a Pd reference foil are shown in Fig. 33a-c. The amplitude of the EXAFS oscillations decreases in the order of Pd foil > Pd/TiO_2 > Au_3Pd_7/TiO_2 > Au_5Pd_5/TiO_2 > Au_7Pd_3/TiO_2. The amplitude and shape of the EXAFS oscillations in Au_xPd_y/TiO_2 clearly differ from those in bulk Pd and Pd/TiO_2.

The structural parameters obtained from fitting the first coordination shell for these samples are given in Table 8. For Pd/TiO_2 the value of $N_{Pd\text{-}Pd}$ is 8.3, which indicates formation of small size Pd entities on TiO_2. In the case of Au_3Pd_7, $N_{Pd\text{-}Pd}$ strongly decreased to 4.0 and $N_{Pd\text{-}Au}$ was 4.1, while N_{Total} (8.1) is still close to 8. The lower value of N_{Total} compared to the bulk material suggests that some Pd atoms are present at the surface and hence not completely surrounded by neighboring Pd/Au atoms. For Au_5Pd_5, $N_{Pd\text{-}Pd}$ decreases to 2.8 and $N_{Pd\text{-}Au}$ increases to 6.0 showing that Au atoms have replaced almost 70% of the Pd atoms in the sample. The value of N_{Total} slightly increases to 8.8, indicating that more Pd atoms are now coordinated to neighboring Au/Pd atoms. In the Au_7Pd_3 sample, the content of Pd is too low which only gives a weak rise to EXAFS oscillations; Therefore, $N_{Pd\text{-}Pd}$ and $N_{Au\text{-}Au}$ determined for this sample show large error margins, however, still a further decrease in $N_{Pd\text{-}Pd}$ was observed with lower Pd content. For the Au_xPd_y samples, Pd-Pd

distance slightly increases with increasing gold content compared to the bulk Pd, indicating lattice expansion. Furthermore, in all samples Pd is in a reduced state (Fig. 33d).

In the case of the Au L_3-edge EXAFS results, the value of N_{Total} is always close to 12, indicating that most Au absorber atoms are completely surrounded by Au/Pd atoms. However, the value of N_{Total} obtained from Pd K-edge EXAFS fitting was ca. 8 as compared to 12 in the bulk material. Thus, in the present Au-Pd system synthesized in the microfluidic reactor, the Au atoms are mixed homogeneously with Pd atoms in the core of the NPs, but Pd is presumably the dominating element in the surface composition of the nanoalloys. Gibson et al.[144] used *in situ* XAS and DRIFTS to study structural changes in AuPd NPs (2.5 wt.% of each metal, synthesized via sol-immobilization in a batch reactor) supported on γ-Al_2O_3 during CO oxidation and concluded from the measured data that during reaction the particles are restructured resulting in a core-shell like structure with a gold core and a Pd shell. However, in the present case it is also possible that some Pd is segregated from the alloyed particles.

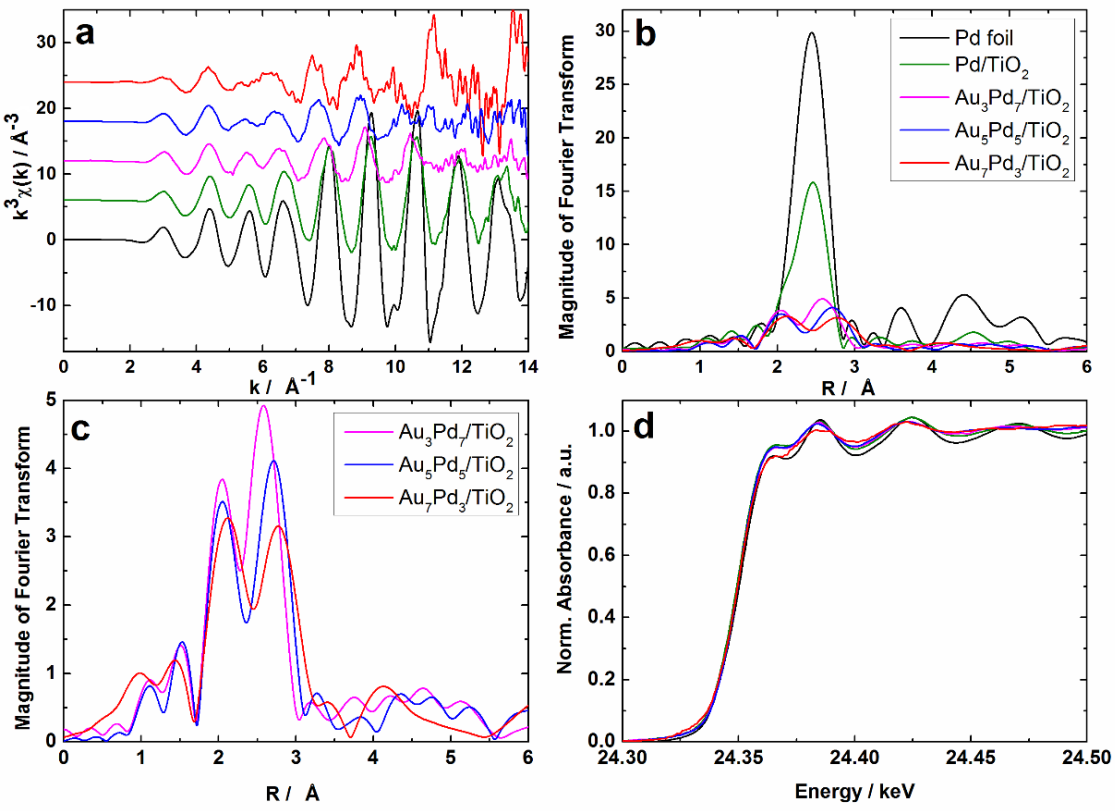

Fig. 33 XAS measurements at the Pd K-edge: a,b) k^3-weighted EXAFS oscillations and magnitude of the Fourier transformed EXAFS data of Pd/TiO_2 and Au_xPd_y/TiO_2 in R-space, c) magnitude of the Fourier-transformed EXAFS of Au_xPd_y/TiO_2 in R-space and d) comparison of the XANES spectra of the produced NPs with Pd foil absorption data[132].

Table 8 EXAFS fit results for Pd/TiO_2 and Au_xPd_y/TiO_2 (Pd K-edge), $S_0^2 = 0.82 \pm 0.11$.

Sample	N_{Pd-Pd}	R (Å)	σ^2 (10^{-3} Å^2)	N_{Au-Pd}	R (Å)	σ^2 (10^{-3} Å^2)	ΔE_0(eV)	N_{Total}
Pd foil	12	2.74±0.00	5.6±0.3	-	-	-	-2.2±0.5	12
Pd/TiO_2	8.3±0.9	2.73±0.02	6.8±0.5	-	-	-	-2.1±1.0	8.3
Au_3Pd_7/TiO_2	4.1±0.5	2.75±0.00	6.8±0.5[f]	4.1±0.9	2.76±0.00	7.4±1.1[f]	-2.3±2.0	8.1
Au_5Pd_5/TiO_2	2.8±0.5	2.76±0.01	6.8±0.5[f]	6.0±0.9	2.77±0.01	7.4±1.1[f]	-2.5±2.0	8.8
Au_7Pd_3/TiO_2	2.3±1.1	2.79±0.05	6.8±0.5[f]	5.7±1.9	2.80±0.04	7.4±1.1[f]	-1.5±3.7	8.0

[f] : fixed during fitting

4.5. CO Oxidation Test on Au/TiO_2, Pd/TiO_2 and Au_xPd_y/TiO_2

Fig. 34a shows conversion of CO over the TiO_2 supported catalysts obtained during heating and Fig. 34b shows the corresponding Arrhenius plots. The CO conversion profiles show the typical behavior of Au catalysts[4, 129, 145] with Au/TiO_2 converting 20% of CO already at room temperature and a moderate light-off curve reaching full conversion at 120 °C. Increasing the Pd content in Au_xPd_y/TiO_2 catalysts results in lower activity at room temperature and a steeper light-off. The monometallic Pd/TiO_2 catalyst shows the lowest activity among the tested samples. The turnover frequencies (TOFs) measured over the Au/TiO_2 catalyst (Table 9) appears to be in the same range as TOF over Au/TiO_2 catalysts measured by Tsubota et al[12]. The TOFs reveal a gradual increase in CO oxidation activity with increasing Au content in the order of $Pd/TiO_2 < Au_5Pd_5/TiO_2 \leq Au_3Pd_7/TiO_2 < Au_7Pd_3/TiO_2 < Au/TiO_2$, which agrees well with the series previously published by Xu et al.[129] and allows the conclusion that the CO oxidation activity of homogeneous mixed nanoalloys of Au_xPd_y in CO oxidation can be described as a sum of activities of the individual Au and Pd components[127] without revealing synergistic effects.

Apparent activation energy decreases in the order of $Pd/TiO_2 > Au_3Pd_7/TiO_2 > Au_5Pd_5/TiO_2 > Au_7Pd_3/TiO_2 > Au/TiO_2$. Monometallics of Au and Pd catalysts display similar E_a to those published by Xu et al.[129] and follow the same qualitative trend reported for Au (100) and Pd (110) surfaces[146]. However, unlike the work of Xu et al.[129], the bimetallic catalysts prepared for this study exhibit E_a values in between those values for the monometallic samples which rules out noticeable synergistic effects.

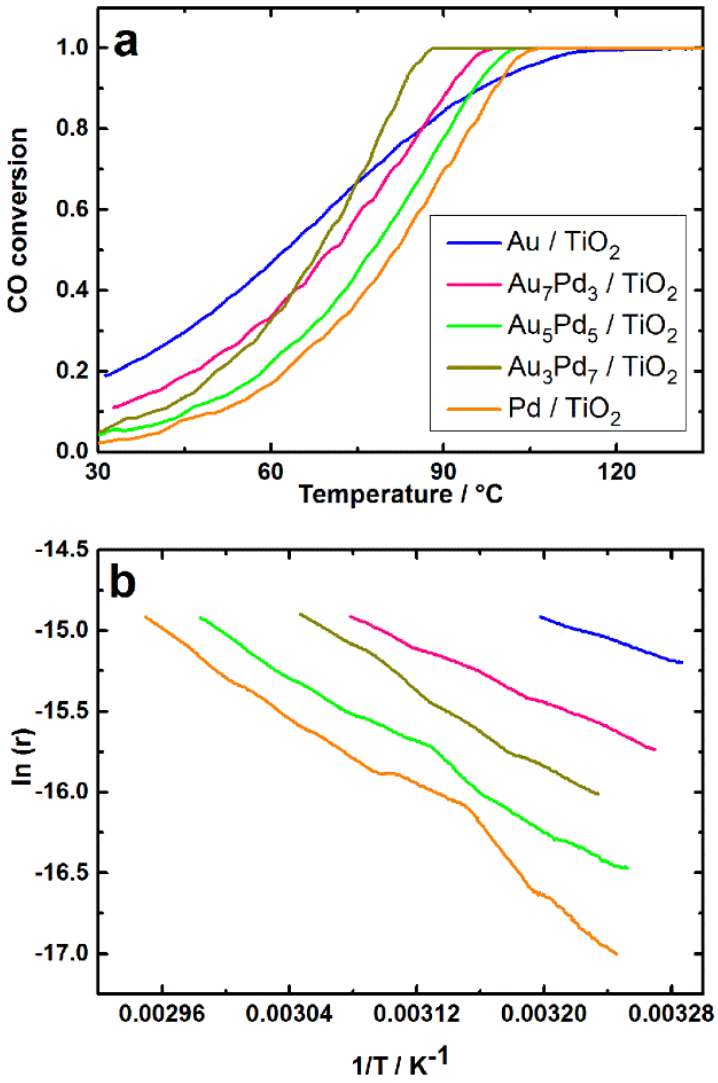

Fig. 34 a) CO conversion and b) corresponding Arrhenius plots obtained during CO oxidation. Conditions: 1000 ppm CO, 10% O_2 in N_2, 300 mg of catalyst, 600 mL min^{-1} flow and 1 °C min^{-1} temperature ramp rate[132].

Table 9 Apparent activation energies for CO oxidation and turnover frequencies obtained over calcined pure TiO_2, Au/TiO_2, Pd/TiO_2 and Au_xPd_y/TiO_2 catalysts.

Catalyst	E_a (kJ mol^{-1})	$TOF_{273\,K}$ (s^{-1})	$TOF_{313\,K}$ (s^{-1})	Surface area[b] ($m^2\ g^{-1}$)
Au/TiO_2	27	1.9×10^{-2}[a]	8.9×10^{-2}[a]	178
Au_7Pd_3/TiO_2	36	6.0×10^{-3}	4.5×10^{-2}	178
Au_5Pd_5/TiO_2	49	1.2×10^{-3}	1.9×10^{-2}	194
Au_3Pd_7/TiO_2	53	1.8×10^{-3}	3.5×10^{-2}	162
Pd/TiO_2	55	4.4×10^{-4}[a]	9.7×10^{-3}[a]	189
TiO_2	-	-	-	154

[a]: Assuming comparable NP diameter as bimetallic catalysts and [b]: from Brunauer–Emmett–Teller (BET) measurements.

4.6. Conclusion

In this chapter, the application of the microfluidic reactor (cf. section 2.1) to synthesize AuPd nanoalloys in a precisely controlled continuous microflow was shown. The microfluidic chip features three cyclone micromixers located immediately after the inlets for the reactants, necessary to achieve homogeneous turbulent mixing of the reactants in a very short time regime (2 ms) at 2.6 L h^{-1} flow rate and a Reynolds number of ca. 2400. By spatially and temporarily homogeneous mixing of the solutions in the micromixers followed by flowing through the microchannel (for 20 ms), highly monodispersed ultrasmall Au, Pd and AuPd colloids were produced using fast reduction reactions ($NaBH_4$ as reducing agent and PVP as surfactant).

The STEM images proved formation of NPs with 1-2 nm diameters. HRTEM investigations of the AuPd bimetallic samples indicate the presence of a crystal-like structure in a single NP with lattice spacings between of those of pure Au and pure Pd, whereas EDX mapping shows a uniform distribution of Au and Pd in one selected particle. The strong suppression of SPR of gold in the UV-vis spectra showed the formation of ultrasmall Au and AuPd NPs and also the full reduction of Pd^{2+} to metallic Pd^0. The produced colloidal NPs aggregated after deposition on titania and calcination to about 5-7 nm.

XANES and EXAFS spectra of Au/TiO_2 and Au_xPd_y/TiO_2 catalysts in the form of pellets showed variation in white line intensity at the Au L_3-edge correlated to the extent of alloying between Au and Pd in these NPs which leads to the conclusion that Au–Pd alloying causes a decrease in white line intensity. The structure and amplitude of EXAFS oscillations at the Au L_3- and Pd K-edge varied with increasing concentration of the second metal. The peaks in the FT data were shifted for bimetallic NPs indicating a change in the lattice constant due to alloy formation. The ratio of the Au-Au and Au-Pd coordination numbers obtained from Au L_3 EXAFS data point towards formation of a homogeneous alloy. Furthermore, coordination numbers extracted from Pd K-EXAFS data revealed the formation of a homogeneous mixture of Au and Pd in these alloyed NPs with either Pd dominating at the NP surface or being segregated as smaller monometallic particles. Since XAS is basically a bulk sensitive technique, the next chapter will shine a light on the surface properties of the NPs based on characterization by surface sensitive methods, i.e. XPS and particularly UHV-FTIR.

CO oxidation was chosen as a test reaction to demonstrate the catalytic activity of the produced catalysts along with the monometallic samples, revealing Au as the most active catalyst, Pd as the least active one and AuPd in between useful for fine-tuning of the catalytic results but without noticeable synergistic effects.

The next chapter introduces UHV-FTIR as an additional, surface sensitive characterization method which was used with CO as probe molecule to investigate microfluidically synthesized Au, Pd and Au_xPd_y NPs on TiO_2 by identifying the different Au/Pd entities on the catalyst surface.

5. Surface Analysis of Au_xPd_y/TiO_2 by CO as a Probe Molecule and Sensing Applications[3]

Previous chapters reported on the microfluidic synthesis and characterization of Au, Pd and alloyed AuPd nanoparticles (in colloidal solution and supported on TiO_2) as well as catalytic tests. While so far, mainly the overall composition and structure of the particles were investigated, the focus in this chapter will be laid on specifically surface sensitive characterization. In order to include an additional facet of potential applications, the produced Au, Pd and AuPd alloyed NPs were supported on SnO_2 and tested as gas sensors.

5.1. Introduction

Small particle sizes trigger two key parameters in increasing the catalytic activity of supported Au NPs: a higher number of low-coordination sites and an increase in the total length of perimeter sites at the metal-support interfaces. It is difficult to separate the effects of these factors from each other, and therefore hard to understand their individual roles in the synergistic performance. Additionally, the quantum size effect and the strain effect add up to this open debate[9, 147, 148].

In the case of large Au NPs and bulk gold, the CO oxidation reaction ($CO + ½ O_2 \rightarrow CO_2$) cannot proceed since the gold surface (stepped or polycrystalline) is not able to dissociate O_2 to form oxygen adatoms (O_{ads}) at temperatures between 200 and 500 K, and there is no evidence for significant adsorption of CO. In a Langmuir-Hinshelwood-type reaction, simultaneous adsorption of CO and active oxygen is necessary for CO oxidation[149-151]. Interestingly, on gold films with only two-atom layer thickness likewise CO oxidation occurs (not on thinner and thicker films) and also the surfaces of gold single crystals show CO oxidation activity even at liquid N_2 temperature (ca. 73 K) if the surface is pre-dosed with atomic oxygen[152]. Therefore, the oxygen adatoms should either be injected onto the gold surface, or provided by a second element on the catalytic surface which is able to dissociate oxygen molecules. In this case, spill over of the as-formed O_{ads} onto Au active sites (which already adsorbed CO) might occur, which then triggers the CO oxidation reaction. One such second element could be palladium to form a AuPd alloy, since Pd is capable of dissociating O_2 even at 150 K. Under steady-state conditions, pure Pd is active for CO oxidation at higher temperature (above 400 K). Therefore, the low temperature CO

[3] Parts of this chapter will be submitted to scientific journals for publication.

oxidation reaction should take place under a less demanding conditions on supported AuPd nanoalloy particles compared to supported Au NPs[149, 153, 154].

In this chapter, the effect of alloying on titania-supported Au_xPd_y NPs with respect to the structure, morphology and surface properties is investigated. Using a novel UHV-FTIR apparatus at KIT-IFG (project leader Dr. Y. Wang), a systematic study on the adsorption of CO molecules on different entities (Ti^{4+}, Au^0, Pd^{2+}, atop Pd^0 and bridge Pd^0) of Au/TiO_2, Pd/TiO_2, and Au_xPd_y/TiO_2 at different temperatures was performed in order to gain a comprehensive understanding of CO oxidation reactions on alloy surfaces.

5.2. Nanoparticles Synthesis and Catalyst Preparation Procedure

5.2.1. Materials

$HAuCl_4 \cdot 3H_2O$ (Roth, 99.5% purity), K_2PdCl_4 (Alfa Aesar, 99.99% purity), PVP (Sigma-Aldrich, average molecular weight 40 kDa), $NaBH_4$ (Sigma-Aldrich, 99.99% purity), H_2SO_4 (Sigma-Aldrich, 95% purity) and TiO_2 (Evonik, commercially available Aeroxide P-25, anatase:rutile phase ratio of 80:20, surface area 50 $m^2\ g^{-1}$) were used without further purification.

5.2.2. Microfluidic Synthesis of Colloidal Au, Pd and Au_xPd_y NPs

Parameters for NP synthesis following the colloidal route for preparation of ultrasmall Au, Pd and Au_xPd_y NPs in the microfluidic reactor were adopted from section 4.2.2. The nominal molar Au:Pd ratios were 1:0, 7:3, 5:5, 3:7 and 0:1.

5.2.3. Preparation of Au, Pd and Au_xPd_y on TiO_2

After dispersing 1 g TiO_2 in 80 mL deionized water in an ultrasonic bath, the obtained colloidal NPs synthesized in the microfluidic reactor were added to the suspension at room temperature and stirred for 1 h. Prior to the impregnation with NPs, the TiO_2 support was acidified with 0.1 mL pure H_2SO_4 solution (suspension pH: 2). Afterwards, the suspension was centrifuged 4 times at 4500 rpm for 5 min and washed with water in between. Finally, the catalysts were dried at 80 °C overnight and calcined at 400 °C for 3 h in static air. This method was applied for preparing 2.4 wt.% Au/TiO_2, Pd/TiO_2 and Au_xPd_y/TiO_2.

5.3. Characterization of Au/TiO_2, Pd/TiO_2 and Au_xPd_y/TiO_2

5.3.1 STEM and EDX

Earlier in section 4.3., it was shown that the colloidal synthesis of ultrasmall Au and Pd as well as Au_xPd_y NPs with a homogeneous alloy structure was achieved using a microfluidic reactor. Fig. 26 shows a STEM image of highly monodispersed spherical NPs with average diameters of ca. 1 nm stabilized by PVP. In this chapter, the same colloidal samples were produced and deposited on a frequently studied TiO_2 (AEROXIDE P-25) support in order to investigate the influence of alloying on the mechanism of CO oxidation on the surface of Au/TiO_2, Pd/TiO_2 and Au_xPd_y/TiO_2.

The particle morphology and size distribution of the produced NPs deposited on TiO_2 after calcination at 400 °C are shown in Fig. 35. From these STEM images and the corresponding histograms, it can be concluded that the size of the NPs increased after deposition and calcination. However, the alloyed Au_xPd_y NPs, especially the Au-rich alloys (Au_7Pd_3 and Au_5Pd_5) show significantly smaller particle sizes and narrower size distributions compared to Au/TiO_2. This could be attributed to the effect of alloying with Pd which apparently prevented the aggregation of NPs to larger sizes. Interestingly, the images of pure Pd/TiO_2 do not clearly show the Pd NPs on the support, probably due to the oxidized state of Pd after calcination resulting in a lower contrast with the titanium oxide, as supported by the IR results shown below. In the case of Pd-rich Au_3Pd_7 alloy, it is difficult to precisely determine NP sizes since there is a segregated contiguous surface layer around the NPs on the support. EDX mapping (Fig. 36) indicated the presence of Pd in this contiguous surface layer. Accordingly, some Pd is segregated out of the NPs, although, Pd is also present together with Au in the NP core. In the Au-rich alloys, Au and Pd atoms are distributed uniformly, and located only at the NP positions. The combination of STEM and EDX mapping indicates that alloying decreases NP agglomeration compared to monometallic Au NPs under the applied preparation condition, and additionally it keeps Pd close to Au atoms in the NP structure, which eventually influences the performance of the catalysts.

Additionally, in order to differentiate between the effects of calcination and deposition/drying on the sintering of the NPs, one uncalcined sample (Au_7Pd_3/TiO_2) was selected for STEM analysis in order to compare the size distribution histograms before and after calcination. Comparison of the results (Fig. 37) clearly shows that the mean NP size increased from 1.3 nm in colloidal form to 4.1 nm after deposition and drying, and further

to 5.2 nm after calcination. Moreover, the NP size distribution was broadened after calcination.

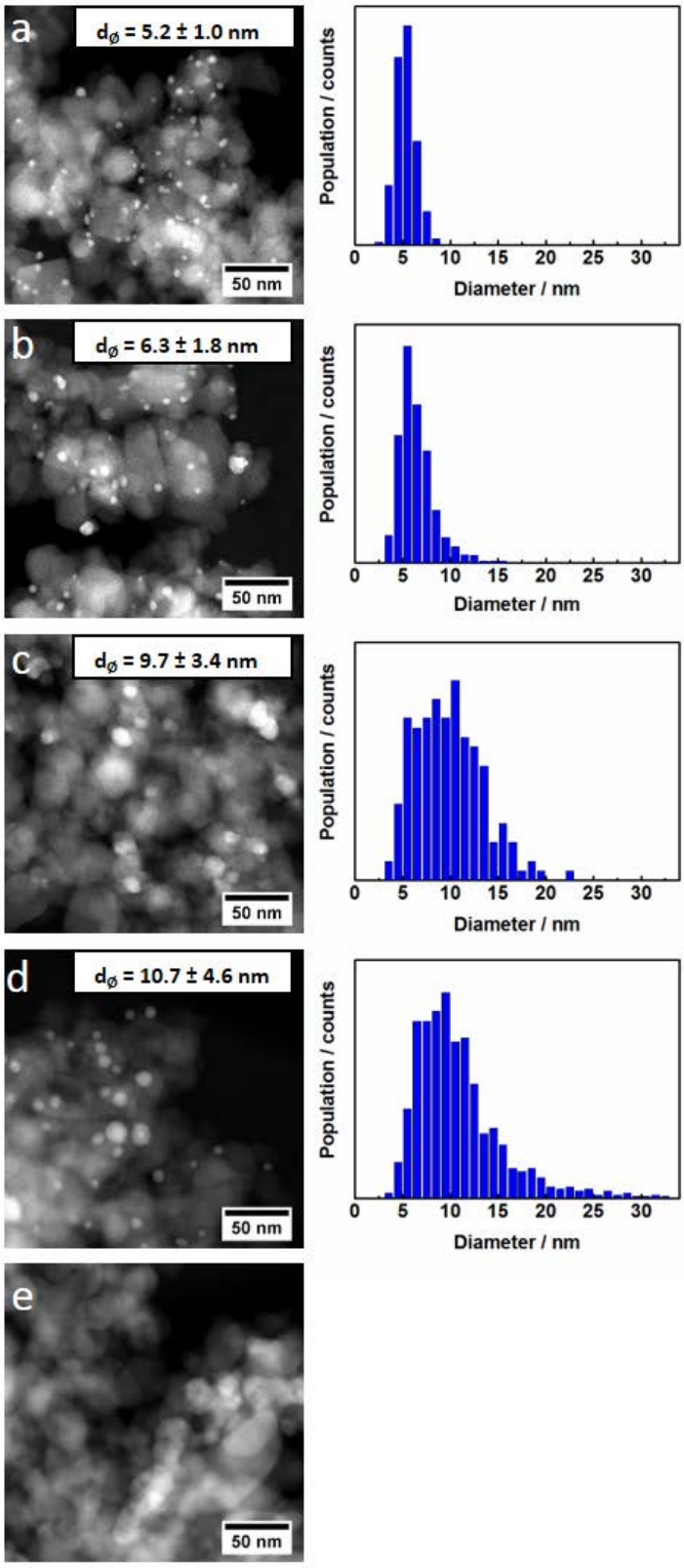

Fig. 35 STEM images and size distributions of calcined a) Au_7Pd_3, b) Au_5Pd_5, c) Au_3Pd_7, d) Au and e) Pd NPs supported on titania.

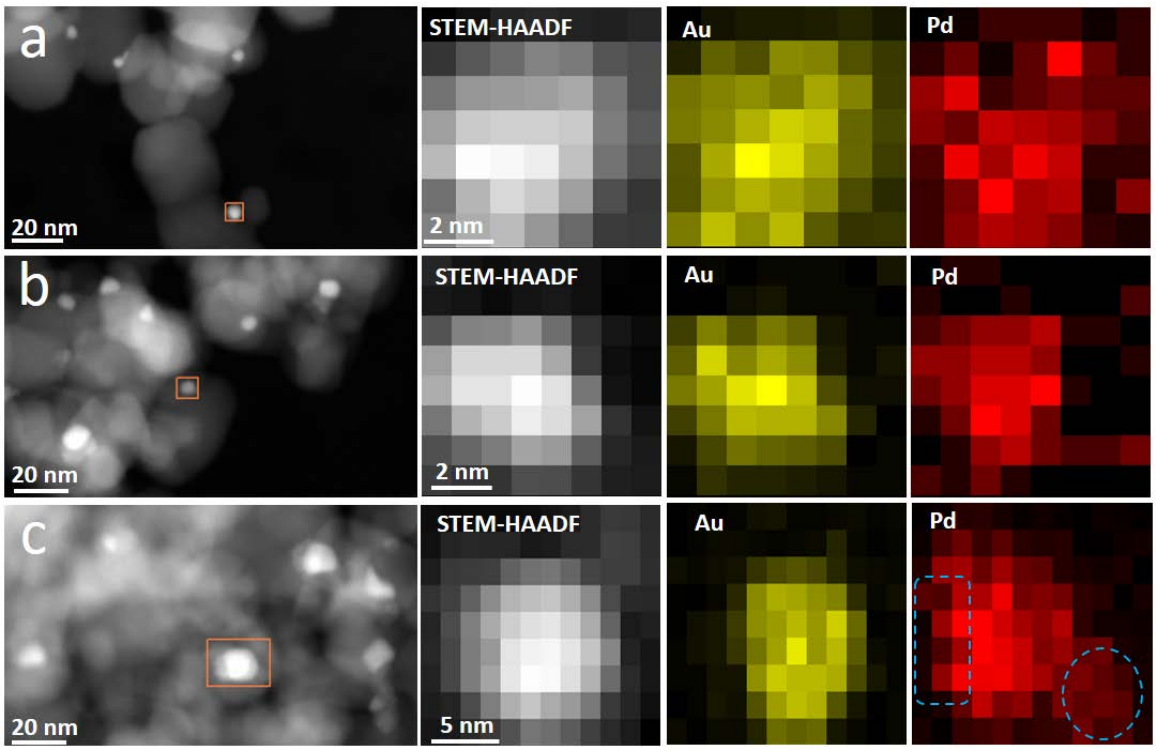

Fig. 36 STEM-EDX mapping of calcined a) Au_7Pd_3, b) Au_5Pd_5 and c) Au_3Pd_7 NPs supported on TiO_2.

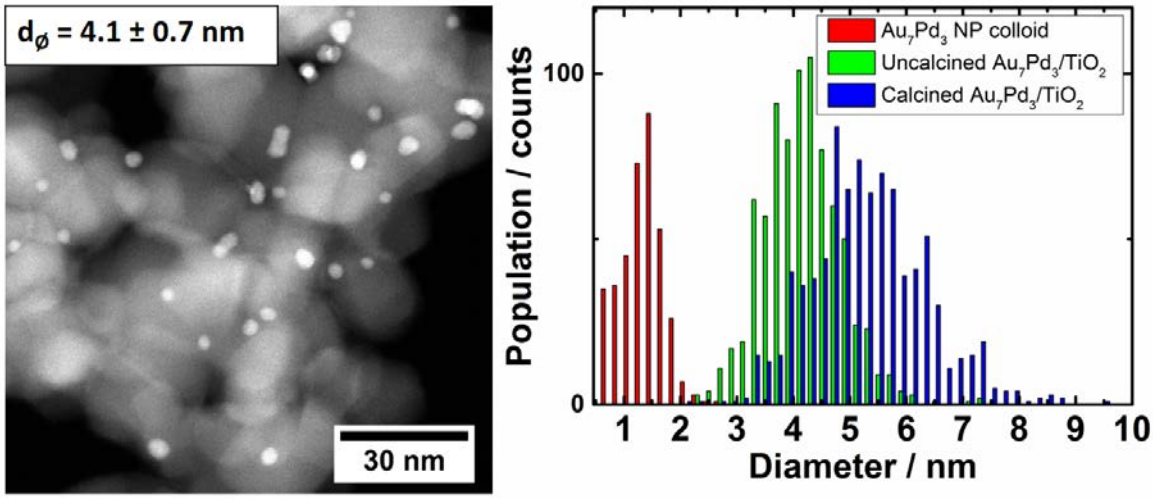

Fig. 37 STEM image of uncalcined Au_7Pd_3/TiO_2 and its size distribution comparison with colloidal Au_7Pd_3 NPs (Fig. 26a) and calcined Au_7Pd_3/TiO_2 (Fig. 35a).

5.3.2 *In situ* XANES Spectroscopy

In order to identify the initial oxidation state of Pd in calcined Pd/TiO_2 and $AuPd/TiO_2$ catalysts and to investigate whether it changes during the annealing treatment (UHV, heating up to 400 °C for 1 h followed by cooling down to room temperature) before the UHV-FTIR experiments, the samples were characterized *in situ* by XANES spectroscopy under inert conditions (N_2 gas flow), while heating up to 400 °C and afterwards cooling down to room temperature. Selected spectra recorded during heating up cycles shown as examples in Fig. 38. They indicate a dominance of oxidized palladium in both samples at all temperatures applied. A very similar behavior was observed during the cooling cycles. For better comparison with the metallic state (i.e. oxidation state zero) spectra of a Pd foil were measured as a reference and included in Fig. 38. They clearly differ from the spectra of the NPs, which accordingly are dominated by oxidized species.

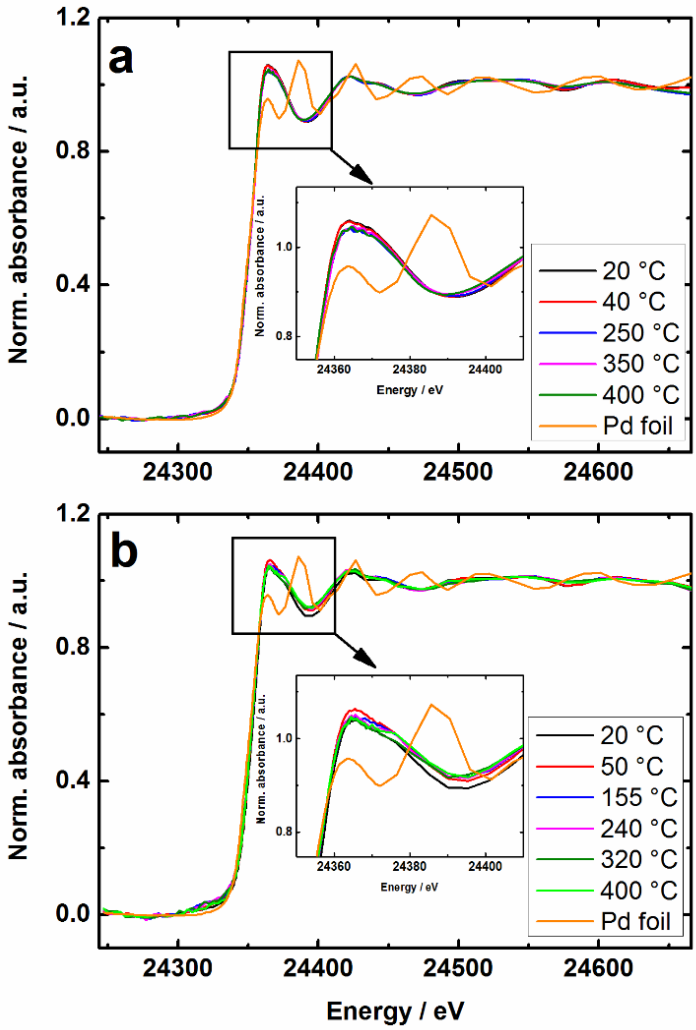

Fig. 38 *In situ* XANES spectra of a) Pd/TiO_2 and b) Au_5Pd_5/TiO_2 in quartz capillaries recorded during heating to 400 °C at a ramp rate of 5 °C min^{-1} in a N_2 flow (33 ml min^{-1}).

5.3.3 X-Ray Photoelectron Spectroscopy

Figure 39 shows the Au 4f and Pd 3d XP spectra of various Au_xPd_y/TiO_2 samples pretreated by annealing at 400 °C for 1h under UHV conditions. In the Au 4f region (Fig. 39a), two spin−orbit components at 84 and 87.7 eV are observed for all Au-containing samples, which are characteristic for metallic Au^0 species. The Pd 3d peaks in the XP spectra are dominated by two spin−orbit components of Pd $3d_{5/2}$ and Pd $3d_{3/2}$ (Figure 39b). For the pure Pd and Pd-rich (70%) AuPd alloy NPs, after deconvolution, two doublets are clearly resolved at 335.3 and 340.6 eV as well as at 337.1 and 342.4 eV, which are assigned to metallic Pd^0 and Pd^{2+} species, respectively[155-157]. On the basis of quantitative analysis, the concentration of Pd^{2+} on the surface was estimated to be about 14.4% in the case of monometallic Pd/TiO_2 sample, and about 9.9% for Au_3Pd_7/TiO_2. These results reveal the presence of oxidized Pd^{2+} species at the surface of pure Pd and segregated contiguous Pd NPs in Au_3Pd_7/TiO_2 as shown by STEM-EDX (Fig. 36). The surface Pd^{2+} species are likely formed via the activation of dioxygen at the active Pd sites. Interestingly, for other bimetallic samples, where the Pd atoms exist only in the form of alloy, the Pd^{2+} species was not observed. This finding indicates a strong interaction between Au and Pd. The Pd $3d_{5/2}$ core-level overlaps with the relatively broad Au $4d_{5/2}$ peak at 335.2 eV, which is resolved for the gold-rich (Au_5Pd_5 and Au_7Pd_3) alloys.

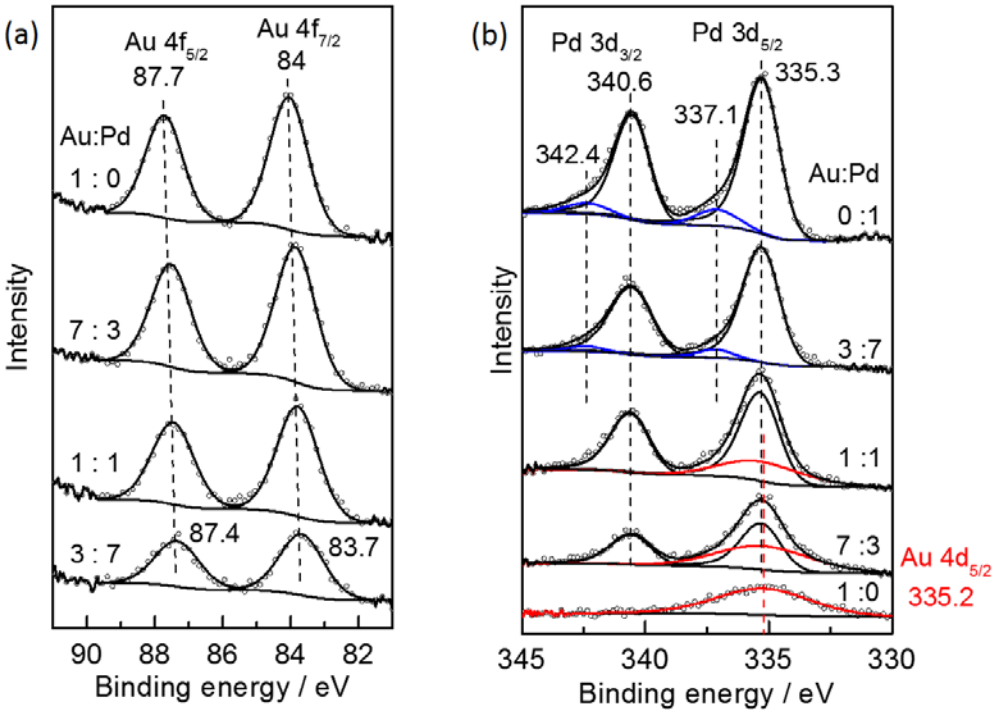

Fig. 39 Deconvoluted XP spectra of Au_xPd_y/TiO_2 samples (x:y = 1:0, 7:3, 1:1, 3:7, 0:1): a) Au 4f region and b) Pd 3d region.

5.3.4 UHV-FTIR Spectroscopy with CO as Probe Molecule

A fundamental study on the adsorption of CO on the TiO_2 supported Au, Pd and AuPd NPs was performed using a novel UHV-FTIR apparatus[78, 158] at KIT-IFG in order to investigate the effect of alloying on CO adsorption based on high-quality temperature-dependent FTIR spectra. In the following section, the obtained results will be presented for each sample separately in detail, and then compared in order to address the effects of alloying in AuPd catalysts. Different surface adsorption sites such as Ti^{4+}, Au^0, Pd^{2+}, atop Pd^0 and bridge Pd^0 on Au/TiO_2, Au_3Pd_7/TiO_2, Au_5Pd_5/TiO_2, Au_7Pd_3/TiO_2 and Pd/TiO_2 were investigated after exposure to 2×10^{-3} mbar CO at different temperatures. Stretching bands of CO adsorbed on monometallic Au or Pd NPs above 2000 cm^{-1} can be assigned to linearly adsorbed CO and bands below 2000 cm^{-1} to CO adsorbed in a bridged configuration[159-162].

UHV-FTIR spectra of Au/TiO_2 powder were recorded at different temperatures. In Fig. 40, the peak centered at 2187 cm^{-1} in the spectrum recorded at 105 K is attributed to CO adsorbed on Ti^{4+}. Based on the temperature-dependent IR data, the binding energy of CO was estimated to be about 40 kJ mol^{-1}, which indicates a rather weak interaction between CO and Ti^{4+}. Its intensity decreased rapidly with increasing temperature and also slightly shifted to higher wavenumbers, due to reduced adsorbate-adsorbate interactions[158].

Moreover, with increasing temperature from 105 K to ca. 190 K, the amount of CO absorbed on Au sites increased (υ_{CO} at 2118-2129 cm^{-1}) due to restructuring of the CO adlayer from a non-uniform distribution at low temperatures to a more homogeneous molecular environment and thereby an increase in order, and also a thermal diffusion of CO adsorbed at Ti^{4+} sites to more stable Au sites[163], and then again decreased. This was accompanied by a slight blue-shift in frequency from 2118 to 2129 cm^{-1}, until it completely vanished at 260 K. It is known that the typical frequency of CO adsorbed on neutral Au^0 sites is located at ~2100-2110 cm^{-1} wavenumber[148, 164-167]. The observed blue-shift for CO on Au/TiO_2 reveals an electronic modification of surface Au species via strong interactions between Au and the TiO_2 support at the interfacial sites. CO preferentially adsorbs chemically on the low-coordinated Au sites at Au/TiO_2 interfaces and completely desorbs only after heating to 260 K, in a accordance with the literature[148]. Interestingly, in the corresponding XPS data only metallic Au^0 species were detected. These findings suggest a strong interaction between Au and TiO_2 support at the interfacial sites.

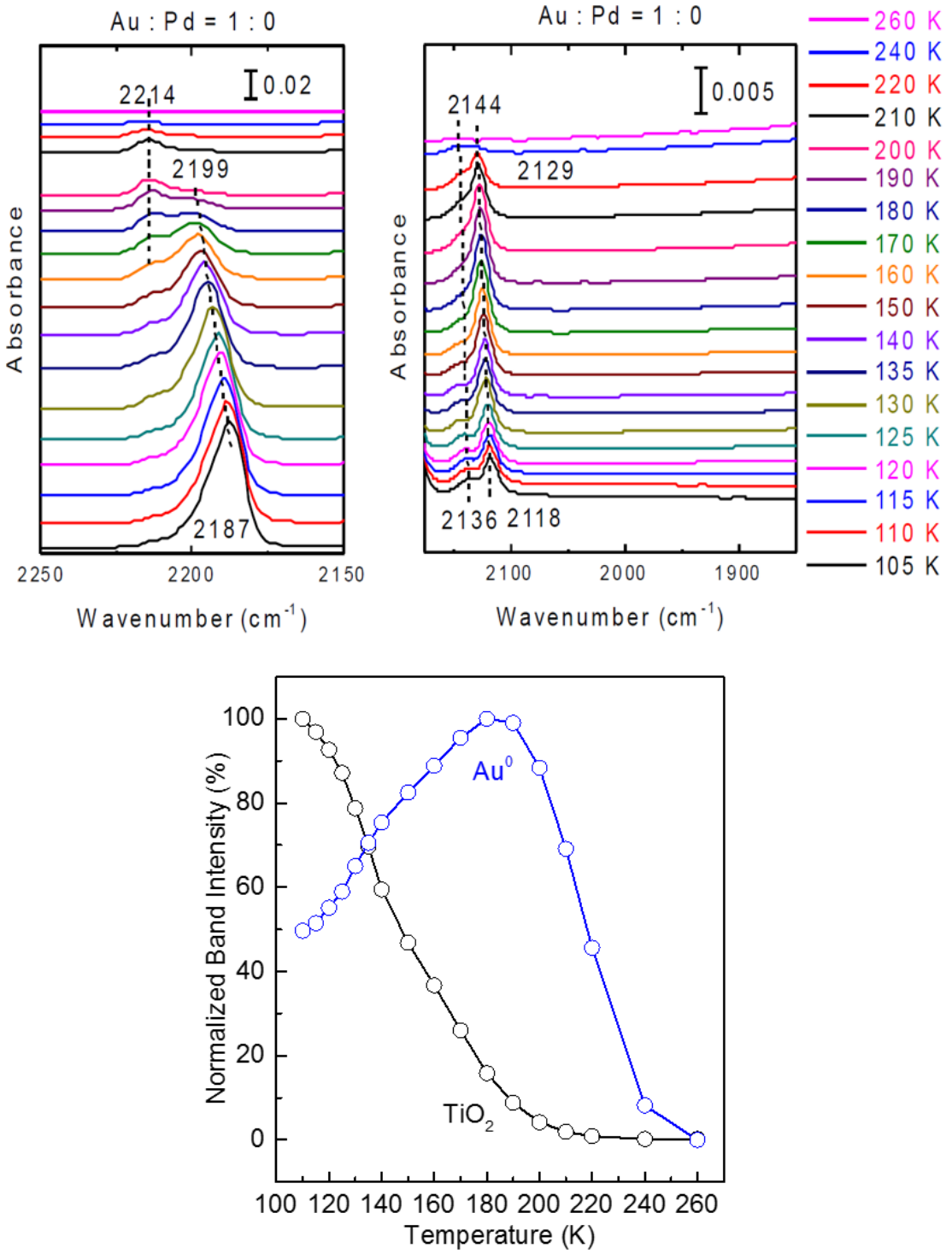

Fig. 40 UHV-FTIR spectra recorded during CO adsorption on the Au/TiO_2 catalyst after exposure to 2×10^{-3} mbar CO at different temperatures.

As the next sample, the Pd/TiO_2 powder catalyst was investigated by UHV-FTIR spectroscopy under the same conditions to study the behavior of pure Pd (Fig. 41). Noticeably, a strong contribution of a υ_{CO} signal from adsorption to Pd^{2+} sites (2152-2163 cm^{-1}) was observed in wide temperature range (105-430 K). Upon increasing the temperature to 200 K, the 2161 cm^{-1} band becomes more intense due to desorption of CO on Ti^{4+} for the same reasons as discussed for Au/TiO_2. It is known that CO molecules bound to specific surface Pd^0 sites exhibit different vibrational frequencies: typically 2110-2070 cm^{-1} for linearly (on-top) bonded CO, 2000-1900 cm^{-1} for 2-fold bridging CO, and 1900-1800 cm^{-1} for CO adsorbed on 3-fold hollow sites[146, 159, 168]. Interestingly, the decrease in the intensity of the band corresponding to CO on Pd^{2+} started around 260 K, which is clearly correlated to the rise in the intensity of the band corresponding to CO on Pd^0. This results indicate surface Pd^{2+} reduction to metallic Pd^0 via CO oxidation with Pd-bonded oxygen species. Worth mentioning, the presence of oxidized Pd in the sample was confirmed earlier by *in situ* XAS and XPS data. In the spectra of this sample, the atop CO on Pd^0 was observed at around 2097-2109 cm^{-1}, i.e. compared to Au/TiO_2 at higher temperatures with a maximum band intensity at 425 K, which decreased with increasing temperature again until it disappeared at 500 K.

After studying the behavior of monometallic Au and Pd NPs supported on TiO_2 with respect to adsorption of CO probe molecules, UHV-FTIR spectroscopy was applied to the more complicated samples, i.e. the AuPd alloys. In the case of Au_3Pd_7/TiO_2, as shown in Fig. 42, there is a large amount of CO adsorbed to Pd^{2+} sites (band at 2152-2161 cm^{-1}) similarly to pure Pd/TiO_2 in the same temperature range; i.e. with increasing temperature from 110 K to 210 K the intensity of the band attributed to CO on Pd^{2+} increased and afterwards decreased to zero at ca. 380 K. Moreover, a red-shift in this peak position during heating was observed. The υ_{CO} at 2092-2099 cm^{-1} was attributed to CO adsorbed on atop Pd^0, similar to the Pd/TiO_2 sample. However, the most pronounced difference between the spectra of this alloy and the monometallic Pd/TiO_2 was the significant bridging CO on Pd^0 peak in Au_3Pd_7/TiO_2, which indicates segregated contiguous Pd sites. This observation is in agreement with STEM and EDX mapping which clearly indicated the presence of a Pd layer surrounding the alloy NPs. This peak at 1950 cm^{-1} began to grow from 110 K on, reached its maximum intensity at ca. 240 K and then decreased gradually with increasing temperature until it vanished at 430 K. Moreover, the peak at 2092-2105 cm^{-1} corresponds

to atop CO on Au^0 and Pd^0 sites, which is red-shifted compared to the pure Au/TiO_2 catalyst presumably due to the chemical modification of gold sites in the alloys.

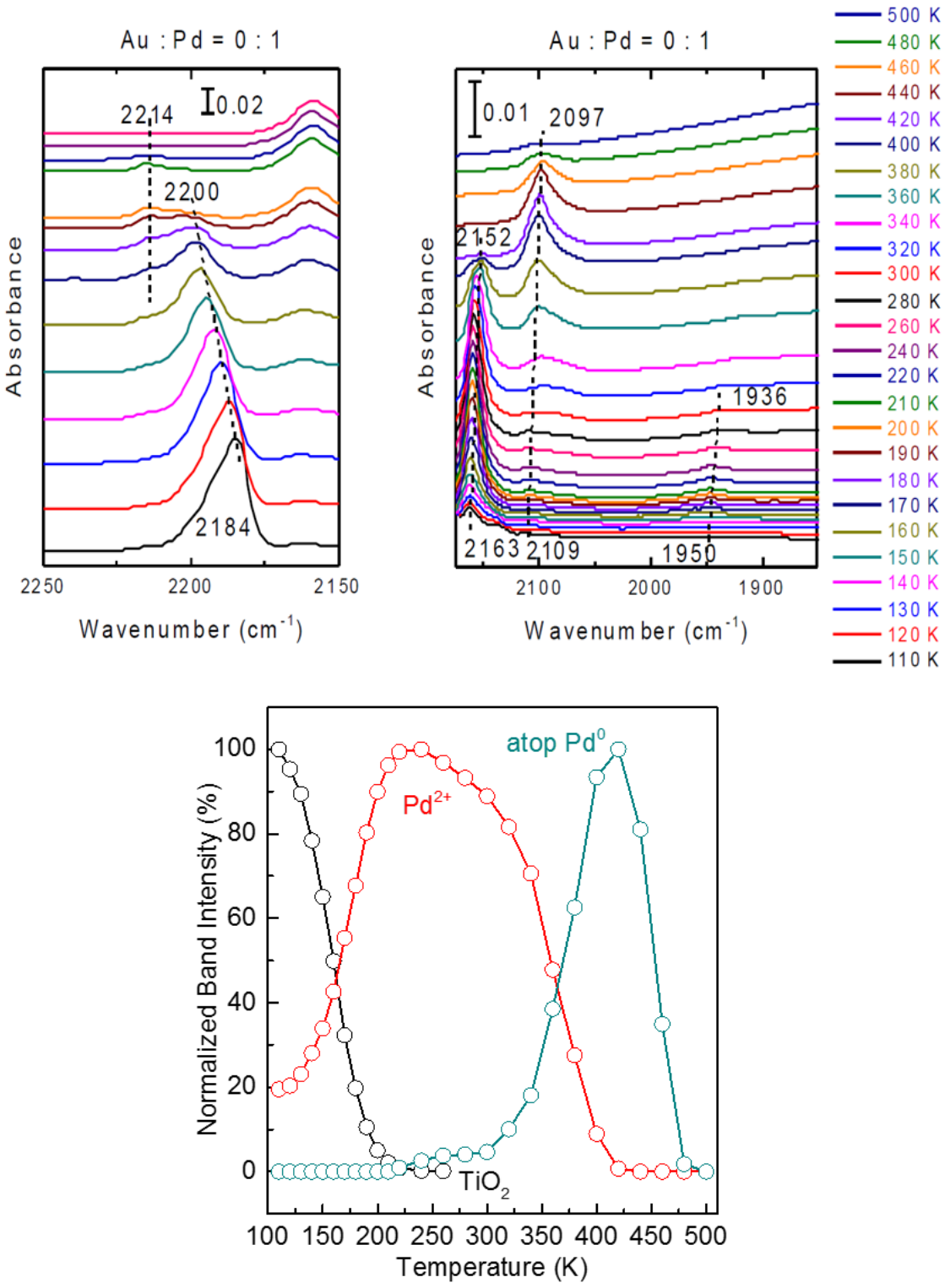

Fig. 41 UHV-FTIR spectra recorded during CO adsorption on the Pd/TiO_2 catalyst after exposure to 2×10^{-3} mbar CO at different temperatures.

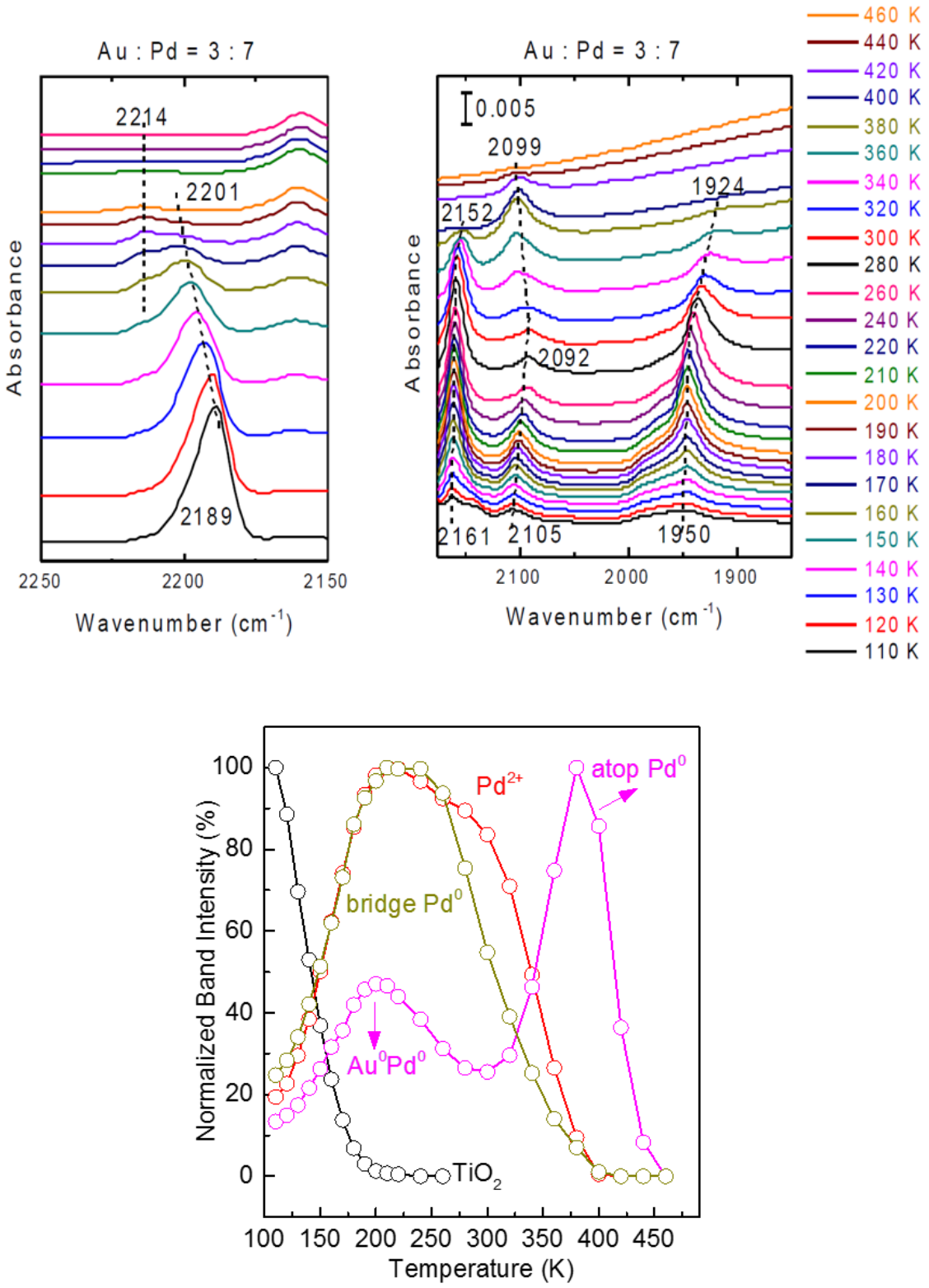

Fig. 42 UHV-FTIR spectra recorded during CO adsorption on the Au_3Pd_7/TiO_2 catalyst after exposure to 2×10^{-3} mbar CO at different temperatures.

The catalytic experiments (cf. Section 5.3.5) prove that the Pd-rich Au_3Pd_7/TiO_2 sample showed superior performance in CO oxidation compared to the other Au_xPd_y/TiO_2 catalysts. This could be related to a synergistic effect, where the Pd-enriched (contiguous) sites activate O_2 while CO chemisorbs on both bimetallic Au and Pd sites. CO binds weaker to Au sites of the bimetallic structure compared to Pd, which should facilitate the low-temperature CO oxidation by diminishing self-poisoning.

The spectra of the Au_5Pd_5/TiO_2 catalyst (Fig. 43) show a significantly higher band intensity of CO adsorbed on Pd bridge sites, rising at 1950 cm^{-1} at 110 K and gradually shifting to 1921 cm^{-1} with increasing temperature up to 380 K. In this case, in contrast to the pure Pd and Pd-rich alloy NPs, CO tends to adsorb mostly on atop Pd^0, Au^0 (around 2109 cm^{-1}) and bridge with Pd^0 atoms, while the CO-Pd^{2+} was observed only as minority species (suggested also by XPS). Moreover, such bridging of CO to Pd^0 indicates Pd segregation at the NP surface, where CO preferentially binds in a bridging configuration with a higher binding energy.

Fig. 44 shows spectra of the Au_7Pd_3/TiO_2 catalyst with high intensities of CO adsorption on Au sites reaching a maximum at around 200-210 K. The feature at 2110 cm^{-1} at 110 K was split into two peaks with increasing temperature: one part of it was blue-shifted to 2121 cm^{-1} with increasing temperature up to 260 K which was assigned to CO bound to Au^0 next to Pd in on-top configuration, while the other part was slightly red-shifted to 2102 cm^{-1} at 300 K and attributed to CO bound to Au^0-enriched (contiguous) sites. In this case, CO absorbed on Pd^{2+} was not observed. However, a strong contribution of CO on atop Pd^0 in a wide temperature range was observed. In this case, the shoulder at 2086 cm^{-1} at 110 K (assigned to CO atop Pd^0) grew in intensity and slightly red-shifted to ca. 2083 with increasing temperature up to 250 K, and then decreased in intensity until it disappeared at 400 K indicating that CO is bound stronger to Pd atoms than to Au. In addition, this band exhibits a red-shift in frequency to 2072 cm^{-1} with rising temperature. This coverage-dependent frequency shift is primarily caused by the adsorbate dipole-dipole coupling interactions, which are typical for CO adsorption on metal surfaces[169, 170]. There was also a a small contribution of bridging CO adsorbed on Pd^0, which indicates small amount of Pd patches at some positions on the surface. This weak bridging CO band at 1940-1950 cm^{-1} reached maximum adsorption at 220 K. The IR data demonstrates that the Au_7Pd_3/TiO_2 surface was dominated by bimetallic Pd^0 and Au^0 atoms whereas no CO-Pd^{2+} species was detected. As discussed in the XPS section, according to Pauling's electronegativity scale a

net Pd to Au charge transfer is expected upon alloying. However, this intermetallic charge transfer is partially compensated by the enrichment of Pd d-electrons and the depletion of Au d-electrons[171-173]. The IR data provided insights into the electronic structure changes of the bimetallic Au and Pd components. A decrease in the Au d charge weakens the electron back-donation from Au into the CO $2\pi^*$ orbital and consequently strengthens the C−O vibration. In contrast, a red-shift of the CO-Pd^0 band occurs as a result of the charge transfer into the d bands of Pd. In fact, at 2086-2072 cm^{-1} the IR band of CO adsorbed on-top of bimetallic Pd sites was observed, which is shifted clearly to lower frequencies compared to CO bound to monometallic Pd atop sites (2100 cm^{-1}). For bimetallic Au-bonded CO (~2120 cm^{-1}) a blue-shift with respect to CO adsorbed at Au-enriched sites (2102 cm^{-1}) was observed.

A summary of the IR frequencies and binding energies of CO adsorbed on different sites of Au, Pd and AuPd supported on TiO_2 is shown in Fig. 45. For monometallic Au and Pd NPs, the Au^0 and Pd^{2+} cations were identified as majority of species, while for bimetallic AuPd NPs, Au^0, atop Pd^0 and bridge Pd^0 become the dominating species. This implies a strong electronic interaction between Au and Pd in the AuPd nanoalloys in which the electrons transferred from Au to Pd keep surface Pd mostly in a metallic state. Interestingly, in Au_3Pd_7 both Pd^{2+} and Pd^0 species were detected by UHV-FTIR. In this case, segregated Pd could to a considerable extent be responsible for the presence of Pd^{2+} in this sample, in accordance with the results of STEM/EDX mapping, while Pd^0 species are due to alloying with gold. This confirms the proposed effect of alloying on CO adsorption. The population of different entities (Ti^{4+}, $Au^{\delta+}$, Au^0, Pd^{2+}, atop Pd^0 and bridge Pd^0) depends on the ratio of Au to Pd, e.g. bimetallic AuPd NPs show a gradual increase in bridge CO-Pd^0 with increasing Pd concentration. According to the literature, the IRRAS features of CO adsorbed on a single crystal AuPd (100) surface were observed at 2060-2085 cm^{-1} for atop CO on isolated Pd and at 1900-2000 cm^{-1} for bridging CO on contiguous Pd sites, respectively. The υ_{CO} peaks above 2100 cm^{-1} correspond to atop CO on Au[129, 149]. These findings are comparable with the present study, considering the fact that investigation of supported NPs involves random crystallographic planes and phase segregations.

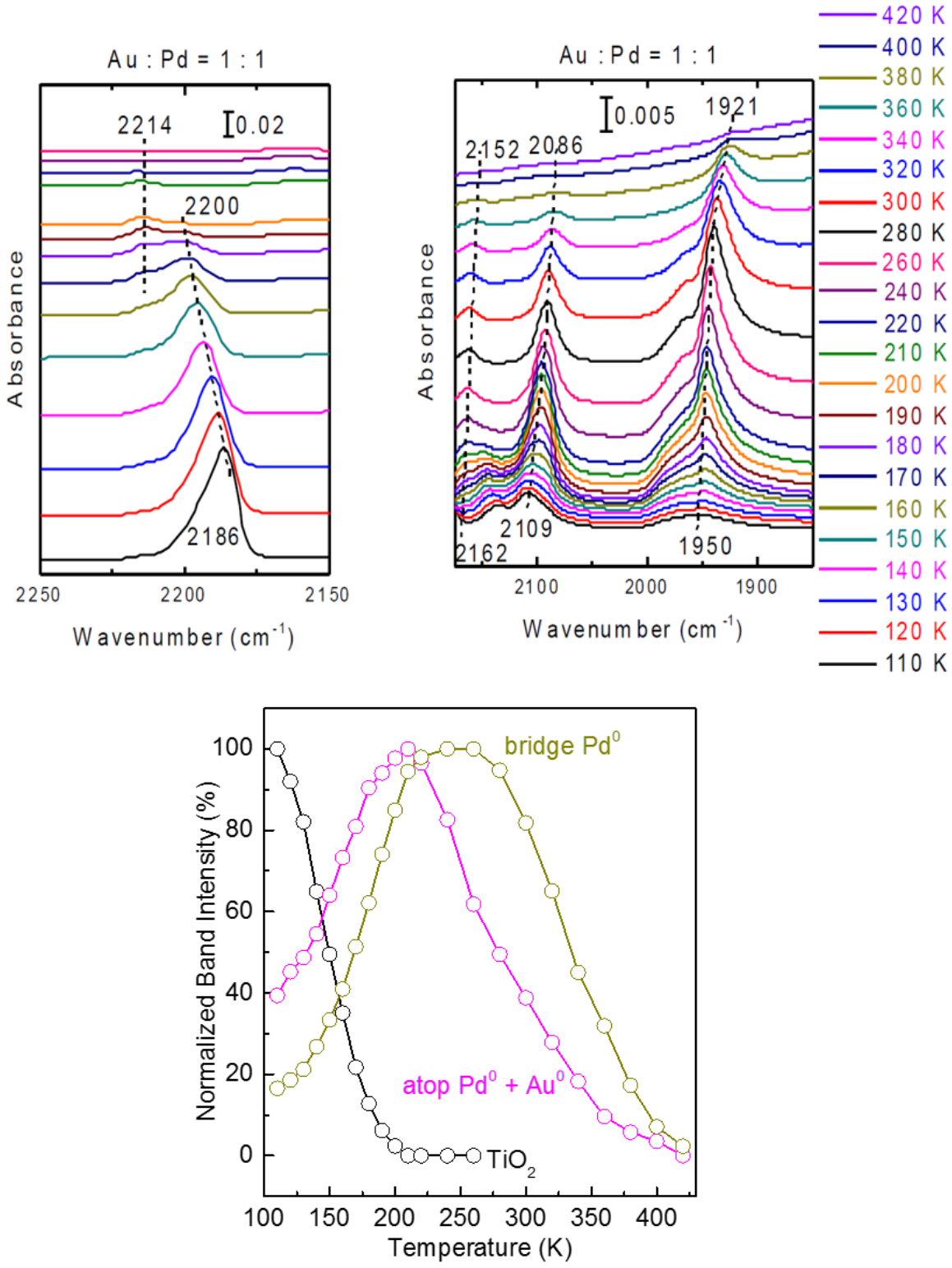

Fig. 43 UHV-FTIR spectra recorded during CO adsorption on the Au_5Pd_5/TiO_2 catalyst after exposure to 2×10^{-3} mbar CO at different temperatures.

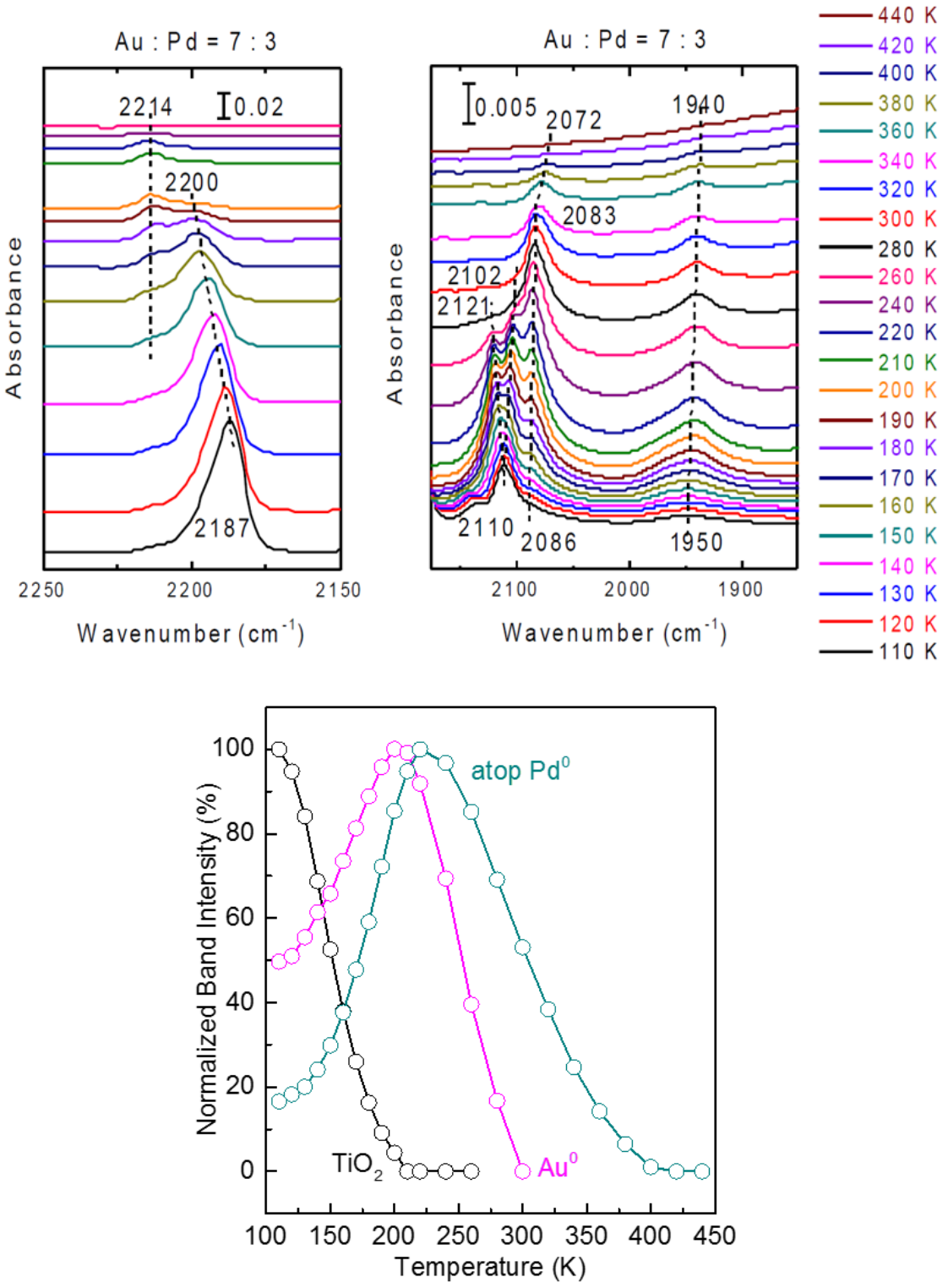

Fig. 44 UHV-FTIR spectra recorded during CO adsorption on the Au_7Pd_3/TiO_2 catalyst after exposure to 2×10^{-3} mbar CO at different temperatures.

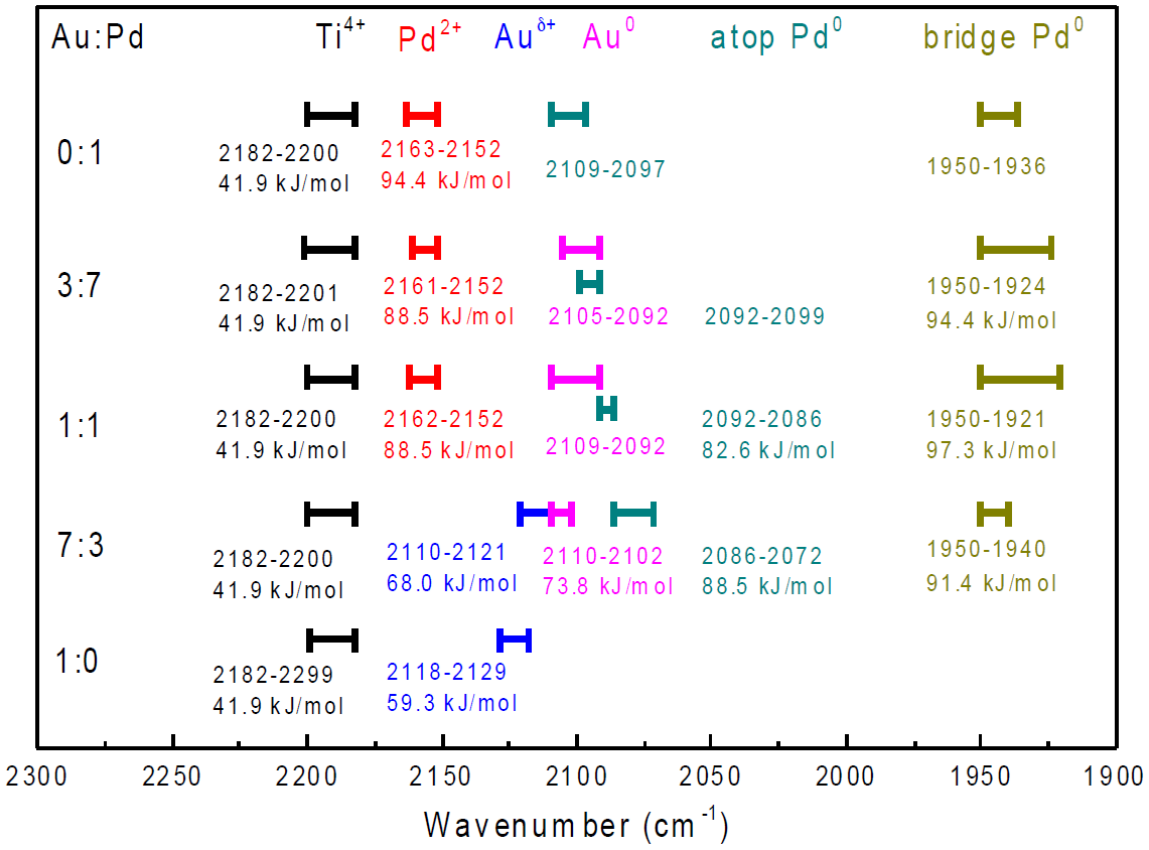

Fig. 45 Summary of IR frequencies and binding energies of CO adsorbed on different sites of Au/TiO_2, Au_3Pd_7/TiO_2, Au_5Pd_5/TiO_2, Au_7Pd_3/TiO_2 and Pd/TiO_2 after exposure to 2×10^{-3} mbar CO at different temperatures.

5.3.5 CO Oxidation with and without H_2 Reductive Pretreatment

Au/TiO_2, Pd/TiO_2 and Au_xPd_y/TiO_2 were tested for CO oxidation in order to assess their performance and to investigate whether annealing in inert atmosphere, as done prior to the UHV-FTIR measurements results in a more active catalyst. For this purpose, CO oxidation tests also on the catalysts were applied first after pretreatment in N_2 flow up to 400 °C for 1 h, and without any reduction process. Afterwards, the tests were repeated under the same conditions after reduction in H_2 at 250 °C for 1 h to reduce the oxidized metal NPs. Fig. 46 shows the CO oxidation tests after both pretreatments and their corresponding reaction rate (r). While Pd/TiO_2 and Au_xPd_y/TiO_2 started to show significant activity above 100 °C, Au/TiO_2 exhibited ca. 30% CO conversion at this temperature. With a gentle light-off curve, Au/TiO_2 reached full conversion at ca. 227 °C. On the other hand, CO conversion by Pd/TiO_2 and Au_xPd_y/TiO_2 catalysts steeply rose in such a way that between 147-177 °C full conversion was achieved (at lower temperature compared to Au/TiO_2). Although,

different pretreatments did not alter the results drastically, the H_2 pretreatment definitely increased the activity of the samples. Among the bimetallic samples, Au_3Pd_7/TiO_2 showed the best performance, which was more obvious in the case of pretreatment with only N_2. The higher catalytic performance of Au_3Pd_7/TiO_2 could be attributed to the coexistence of isolated and alloying Pd NPs as imaged in STEM-EDX (Fig. 36). The isolated Pd NPs are more active in the dissociation of dioxygen forming atomic O species. This could be followed by oxygen spillover to the interfacial sites between AuPd and TiO_2, where the O reacts with activated CO to yield CO_2. Reduction of oxidized metal NPs with H_2 improved the activities of Au_5Pd_5/TiO_2, Au_7Pd_3/TiO_2 and also Pd/TiO_2 more clearly compared to Au_3Pd_7/TiO_2.

Kinetic parameters extracted from the conversion curves are shown in Table 10. The rates in terms of TOF gradually increase in the order of $Au_5Pd_5/TiO_2 < Pd/TiO_2 \leq Au_7Pd_3/TiO_2 < Au_3Pd_7/TiO_2 < Au/TiO_2$. Apparent activation energies decrease in the order of $Au_5Pd_5/TiO_2 > Au_3Pd_7/TiO_2 \geq Pd/TiO_2 \geq Au_7Pd_3/TiO_2 > Au/TiO_2$. Reductive pretreatment enhanced the CO oxidation rate and lowered the activation energy E_a. This may be due to O vacancies (O_v) generated in the reducible TiO_2 support. O_v can have a twofold effect: They facilitate dissociative adsorption of O_2, and can stronger bind adsorbed CO. It is known that oxidation of CO to CO_2 on metallic clusters is determined by adsorption and dissociation of molecular oxygen and the binding strength of carbon monoxide. Since the activation energy of CO oxidation over Au_5Pd_5/TiO_2 and Au_7Pd_3/TiO_2 decreased after reductive pretreatment, it is assumed that CO poisoning also decreased (which would contradict stronger adsorption of CO on O_v of TiO_2). Thus, in this case dissociation of O_2 is rate limiting, similar to the pathway proposed for Au/CeO_2. The strongest synergetic effect of Au and Pd is shown by the PdO containing catalyst. PdO is highly active in dissociative adsorption of O_2, and metallic AuPd sites adsorb CO without being poisoned. The fact that E_a and TOF over Au_3Pd_7/TiO_2 virtually do not change after reductive activation indicates that O_2 activation is passed on from O_v in the TiO_2 support to PdO (reductive pretreatment leads to Pd^0 which is known to quickly reoxidize at intermediate temperatures in the presence of O_2, i.e. the reductive activation does not stabilize Pd^0 in the oxidizing feed).

These results indicate that the bimetallic catalysts show synergistic effects at higher temperatures, with Au_3Pd_7/TiO_2 revealing the highest activity in CO oxidation due to AuPd alloyed NPs responsible for adsorption of CO without being poisoned and Pd^{2+} component

activating molecular O_2. These findings confirm the anticipation based on UHV-FTIR data regarding the catalytic performance of such samples.

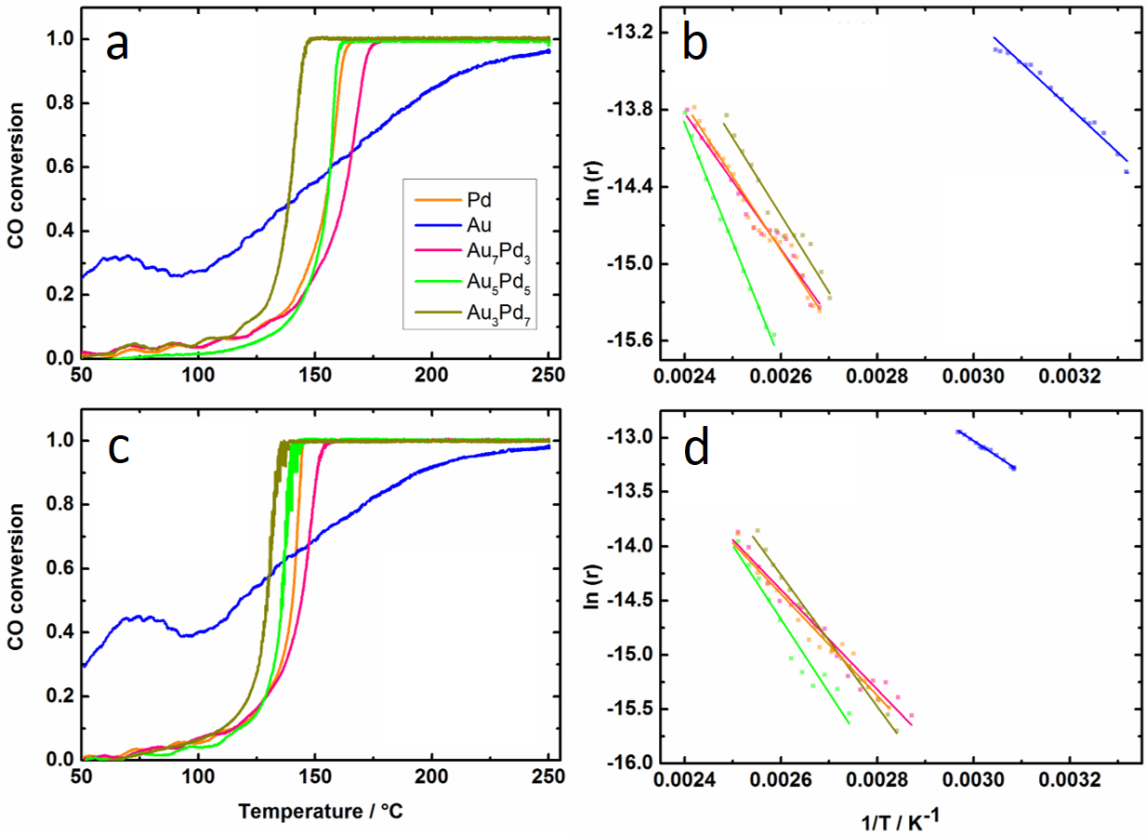

Fig. 46 CO conversion over Au/TiO_2, Au_3Pd_7/TiO_2, Au_5Pd_5/TiO_2, Au_7Pd_3/TiO_2 and Pd/TiO_2 catalysts after (a) N_2 and (c) H_2 pretreatment and their corresponding Arrhenius plots (b and d), respectively. Conditions: 1000 ppm CO, 10% O_2 in N_2, GHSV: 48000 h^{-1} and 1 °C min^{-1} ramp rate.

Table 10 Apparent activation energies, TOFs and temperatures of 50% CO conversion ($T_{1/2}$) for CO oxidation tests.

Sample	After N_2 pretreatment				After H_2 pretreatment			
	E_a kJ mol^{-1}	$TOF_{313\ K}$ s^{-1}	$TOF_{393\ K}$ s^{-1}	$T_{1/2}$ K	E_a kJ mol^{-1}	$TOF_{313\ K}$ s^{-1}	$TOF_{393\ K}$ s^{-1}	$T_{1/2}$ K
Au/TiO_2	29	1.1	10.3	415	24	1.3	8.5	391
Au_7Pd_3/TiO_2	44	6.2×10^{-3}	1.9×10^{-1}	435	38	1.5×10^{-2}	3.0×10^{-1}	417
Au_5Pd_5/TiO_2	77	3.0×10^{-4}	1.1×10^{-1}	428	56	3.5×10^{-3}	2.8×10^{-1}	408
Au_3Pd_7/TiO_2	50	8.7×10^{-3}	4.3×10^{-1}	412	50	1.2×10^{-2}	6.2×10^{-1}	402
Pd/TiO_2	47	6.1×10^{-3}	2.5×10^{-1}	428	39	1.7×10^{-2}	3.7×10^{-1}	413

5.4. Conclusion

Ultrasmall Au_xPd_y (x:y = 1:0, 7:3, 5:5, 3:7 and 0:1) NPs were synthesized in a continuous flow using the microfluidic reactor presented in this thesis. A flow rate of 1.3 L h^{-1} was chosen for each reactant line (line 1: Au and Pd precursor and line 2: $NaBH_4$ as reducing agent.) PVP was used as surfactant in both lines. The ultrasmall colloidal NPs with particle sizes of ca. 1 nm were deposited on a TiO_2-P25 support. STEM images showed the sintering/aggregation of NPs on the support after deposition, drying and calcination treatments. Among these samples, Au_xPd_y/TiO_2 (especially the Au-rich alloys) showed to a lower extent particle growth (ca. 5 nm). In the case of Pd/TiO_2, it was difficult to observe Pd NPs by STEM presumably because they were covered by an oxidized Pd layer. Combined STEM and EDX mapping demonstrated that there was a Pd segregated contiguous layer around the NPs in the Pd-rich alloy (Au_3Pd_7/TiO_2). Interestingly, this sample showed some synergistic effect in CO oxidation tests compared to the other samples. Au/TiO_2 reached full conversion at about 227 °C with a mild light-off curve. However, Pd/TiO_2 and Au_xPd_y/TiO_2 catalysts showed a steep rise in their activities in such a way that full conversions were obtained at lower temperature than Au/TiO_2 (between 147-177 °C). Pd containing catalysts showed higher CO oxidation activity after reduction with H_2. The effect of this reduction was not significant in the results of Au_3Pd_7/TiO_2, which performed better than the other samples.

XAS spectra of the Pd/TiO_2 and $AuPd/TiO_2$ recorded *in situ*, proved the presence of oxidized Pd in the temperature range between 25 and 400 °C under inert conditions. This information is necessary to find out whether the oxidation state of palladium changes during pretreatment for UHV-FTIR measurements. The Pd^{2+} species were also detected for pure Pd and Pd-rich alloy NPs in the corresponding XPS data. Importantly, XPS results showed also the presence of metallic Pd^0 as major species, revealing that only the surface Pd was oxidized by oxygen. Different surface species (Ti^{4+}, Au^0, Pd^{2+}, atop Pd^0 and bridge Pd^0) were identified by *in situ* IR studies using CO as probe molecule at specific temperatures. Within this regards, the behavior of bimetallics differed from the monometallics. This means that in the case of monometallic Au and Pd NPs, Au^0 and Pd^{2+} cations were identified as majority of species, while for bimetallic Au_xPd_y NPs, Au^0, atop Pd^0 and bridge Pd^0 become dominant. The population of these entities altered also with the Au:Pd ratio, e.g. bimetallic AuPd NPs show a gradual increase of bridge Pd^0 with increasing Pd

concentration. These IR results indicated a strong electronic interaction between Au and Pd.

In order to add a new facet to the potential applications, Au, Pd and AuPd NPs prepared in the microfluidic reactor were deposited on SnO_2 supports with different surface areas. The performance of the resulting nanomaterials in gas sensing, specifically detection of CO, CH_4 and volatile organic compound (VOCs) such as toluene and ethanol, and the influence of different metal loadings is discussed in the following section.

5.5. Au, Pd and AuPd NPs in Gas Sensing Applications

Metal oxide semiconductors (MOSs) have motivated research efforts in scientific communities with respect to a variety of applications including gas sensors for the detection of flammable and toxic gases such as carbon monoxide, hydrogen, methane etc[109, 110, 175, 176]. One such MOS is tin dioxide (SnO_2), an n-type semiconductor with a wide energy gap. SnO_2 has been considered for other applications such as catalysis, rechargeable Li batteries and optical-electronic devices[177, 178]. In recent studies, noble metal nanoparticles (e.g. Pd, Pt and Au) have been doped to SnO_2 surfaces as sensitizers in order to alter its electronic structure, which eventually leads to modification of its chemical and physical properties. This increases the sensor signal to noise ratio (SNR), stability and sensitivity against perturbing effects caused e.g. by interfering gases and humidity. With regard to the performance of such sensors, many characteristic features related to nanoparticles play influential roles such as particle size and size distribution as well as shape, structure and metal-support interaction which all depend on the preparation method and further treatment e.g. calcination temperatures[109, 179-184]. *Operando* XAS has emerged as a powerful technique to gain a deeper understanding of the mechanisms involved in the improvement of sensing properties upon addition of such sensitizers. In this context, Koziej et al.[185] characterized a Pd/SnO_2 sample with low metal loading (0.2 wt.%) and observed finely dispersed Pd in atomic state (or as very small clusters) on the SnO_2 surface which presumably binded to the surface lattice oxygen (in contrast to a 3 wt.% Pd/SnO_2 sample which formed larger Pd clusters). This material improved the sensor signal by well-dispersed Pd, and not via a spill-over or Fermi-level control mechanism. In this sample Pd remained oxidized during the *operando* studies which explains the high performance, since oxidized Pd shows better sensing properties compared to Pd in metallic state[186]. *Operando* XANES investigations on Au/SnO_2 sensor materials by Degler et al.[110] indicated a spill-over mechanism in which oxygen adsorbed on the Au surface was transferred to tin dioxide. The negatively charged ionic oxygen species were responsible for interaction with the target gases, hence increasing the sensor performance in presence of Au sensitizers.

In this chapter, the performance of Au, Pd and AuPd NPs doped on two different SnO_2 supports (with different specific surface area) in sensing application is reported in order to demonstrate the high potential of the NPs produced in the microfluidic reactor (explained in detail in chapter 4). Furthermore, Au/SnO_2 samples with different metal were investigated to address the effect of metal loading and possible sintering of NPs. In the

latter case, the Au NPs were produced in a batch reactor. The sensing tests were performed within a collaboration with the University of Tübingen (project leader Dr. N. Barsan).

5.6. Synthesis and Preparation

5.6.1. SnO_2 Synthesis

Tin dioxide was provided by the University of Tübingen. The synthesis method was aqueous sol-gel, in which $SnCl_4$ (Merck, purified by distillation) was used as precursor. The precipitated solid material was filtered and washed several times and dried at 120 °C. Afterwards, it was divided into two samples, one calcined at 450 °C and the other at 1000 °C for 8 h under air. This led to the formation of SnO_2 with two different specific surface areas; (32.7 $m^2 g^{-1}$ and 3.6 $m^2 g^{-1}$), which in this work will be called as SnO_2-HS and SnO_2-LS, respectively. The powders were finally milled before use.

5.6.2. Microfluidic Synthesis of Colloidal Au, Pd and AuPd NPs and Immobilization on SnO_2

The colloidal route for synthesis of ultrasmall Au, Pd and AuPd NPs using a microfluidic reactor are described in section 4.2.2. The nominal molar Au:Pd ratios were 1:0, 1:1 and 0:1. The metal NP solution produced in the microreactor was added to a suspension of 1 g SnO_2 in 80 mL water acidified with 10 mL H_2SO_4 solution (0.58 M) while stirring at room temperature for 1 h. After adsorption of the metal colloids on the support, the suspension was centrifuged three times (4500 rpm, 5 min each) and washed with water until pH 5-6 was achieved. Subsequently, the material was dried at 80 °C overnight. Afterwards, the samples were calcined at 380 °C for 60 min. This method was used to prepare sensor materials with different Au, Pd and AuPd loading on SnO_2-HS and SnO_2-LS.

5.6.3. Batch Synthesis of Colloidal Au NPs Reduced by THPC/NaOH and Immobilization on SnO_2

The colloidal route for synthesis of Au NPs in the batch reactor are described in section 3.2.4. For immobilizing the Au NPs on the SnO_2 support, the metal NP solution produced in the batch reactor was added to a suspension of 1 g SnO_2 in 114 mL water acidified with 6 mL H_2SO_4 solution (0.2 M) while stirring at room temperature. After adsorption of the metal colloids on the support, the suspension was filtered and washed 3 times with deionized water. Subsequently, the material was dried at 130 °C overnight. Afterwards, the samples were calcined at 400 °C for 60 min. This method was used to prepare sensor materials with different Au loading (0.25 and 1.0 wt.%) on SnO_2-HS and SnO_2-LS.

5.6.4. Gas Sensor Preparation

Gas sensors were made by screen printing a paste, made from undoped or metal-doped SnO_2 powders and an organic binder (propandiol), on alumina substrates equipped with interdigitated Pt-electrodes and a backside heating meander (Pt)[187].
Gases were mixed using home-made gas dosing units with mass flow controllers, addition the diluted analyte gas to the carrier gas stream (synthetic air, 20.5% vol O_2) with a total flow of 250 sccm. Humidity levels were dosed by using evaporators filled with deionized water. All gases were supplied by Westfalen AG Münster.

The sensors were heated by applying a specific voltage and current to the backside heaters using a DC-powder supply (Agilent E3614A) and adjusting the exact values according to the sensor's temperature calibration. All experiments were conducted at 300 °C. The sensor response (resistance R) was measured using a digital multimeter (Agilent 34410A). All experiments were performed by measuring one sensor at a time to avoid downstream effects.

The sensor signal was calculated based on the following equations:

- For reducing gases ($R_0 > R_{gas}$; CO, acetone, ethanol, H_2O):

$$S = \frac{R_0}{R_{gas}}$$

- For oxidizing gases ($R_{gas} > R_0$; NO_2):

$$S = \frac{R_{gas}}{R_0}$$

5.7. Sensing Results

The strategy was to compensate the effects of different specific surface areas of SnO_2 by different loadings of Au, Pd and AuPd NPs synthesized in the microfluidic reactor, i.e. by depositing 0.1 wt.% metal on SnO_2-LS and 1.0 wt.% metal on SnO_2-HS, since the specific surface areas of SnO_2-LS and SnO_2-HS differ by one order of magnitude. The results shown in Fig. 47 lead to the following observations for this series of samples:

Doping SnO_2 with monometallic of Au and Pd NPs improved the CH_4 sensing signal in humid air, in the case of SnO_2-LS even in dry air. AuPd had no effect (SnO_2-LS) or a negative effect (SnO_2-HS) on the CH_4 sensing signal.

Au strongly enhanced the CO sensing signal. A positive effect of Pd on CO sensing was only observed in the case of SnO_2-LS in humid air. With respect to CO sensing, AuPd had no beneficial effect on SnO_2-HS and worked only for SnO_2-LS in humid air.

Regarding volatile organic compound (VOC) sensings, qualitatively, similar effects of the loadings on both SnO_2 materials are observed, however in the case of SnO_2-LS the effects were much stronger. One could highlight the good VOC sensor signals of Au-loaded SnO_2-LS for toluene.

While Pd and especially Au improved the sensor signals, the AuPd alloy had no such effect, except for CH_4 sensing in dry air (but not significantly) and CO sensing with SnO_2-LS in humid air. For all other tested gases/conditions, the signals did not exceed those from undoped SnO_2 and were in many cases lower.

Taking the Au doped samples as an example (0.1 wt.% Au/SnO_2-LS performed the best), one could conclude that the surface concentration is a dominating factor compared to the properties of the SnO_2 base materials (in most cases undoped SnO_2-HS performed better than undoped SnO_2-LS). In the case of Au/SnO_2, there are qualitatively strong differences between SnO_2 materials, (in the case of AuPd alloy the differences are weaker). However, with respect to Pd loading, one could still see the differences comparing the toluene and ethanol sensing in dry and humid air, thus there is also an influence of the SnO_2 material on the sensing performance.

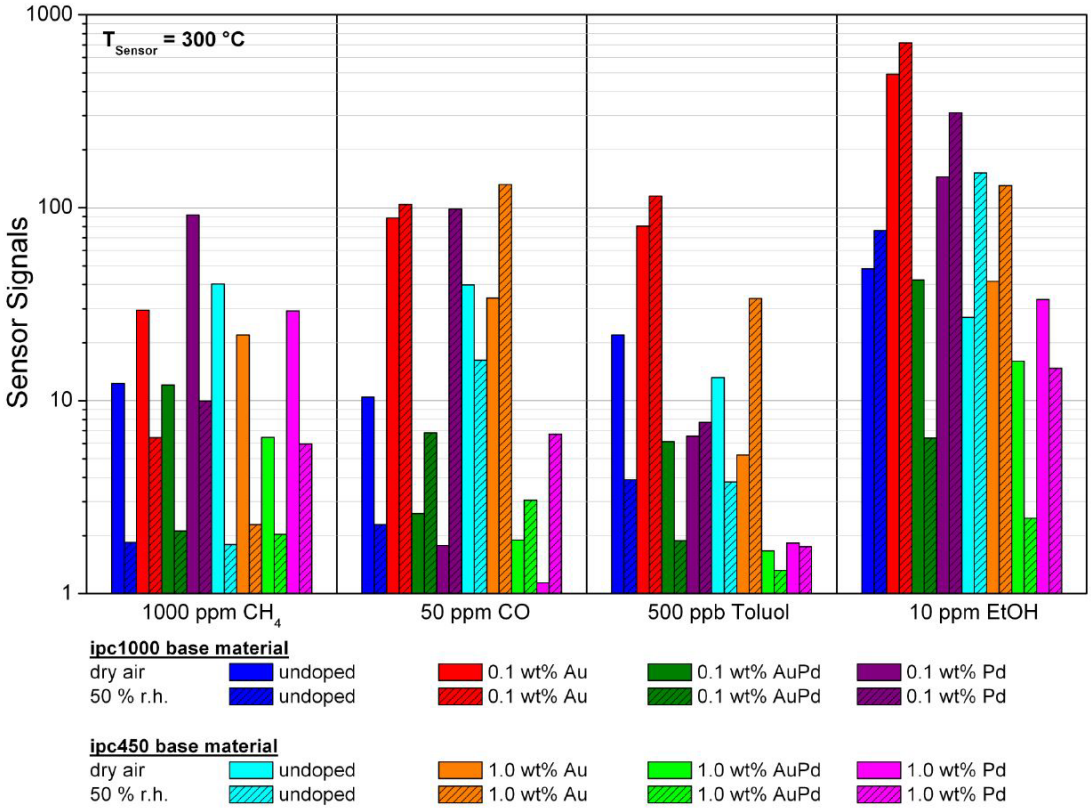

Fig. 47 Sensing performance of supported Au, Pd and AuPd on SnO_2-LS (1000) and SnO_2-HS (450).

In the case of Au NPs produced in the batch reactor with 0.25 and 1.0 wt.% loading on SnO_2-HS and SnO_2-LS, the following results were obtained (Fig. 48):

Au NPs enhanced the CO sensing for both SnO_2 materials and suppressed the performance of both SnO_2 materials in NO_2 sensing. In the case of VOCs, a distinct role of the SnO_2 material was observed: For SnO_2-HS, Au enhanced the signals of ethanol and acetone sensing, whereas for SnO_2-LS, Au had no positive impact on acetone sensing (decreased in dry air, similar in humid air). For SnO_2-LS, Au enhanced the ethanol signals in humid air, but had no significant effect on sensing in dry air.

Generally, it can be stated, that there is a difference between the based materials, either due to (1) different properties originating from surface termination by hydroxyl groups or oxygen vacancy concentration and (2) different specific surface areas leading to a different Au concentration per surface area unit of the samples.

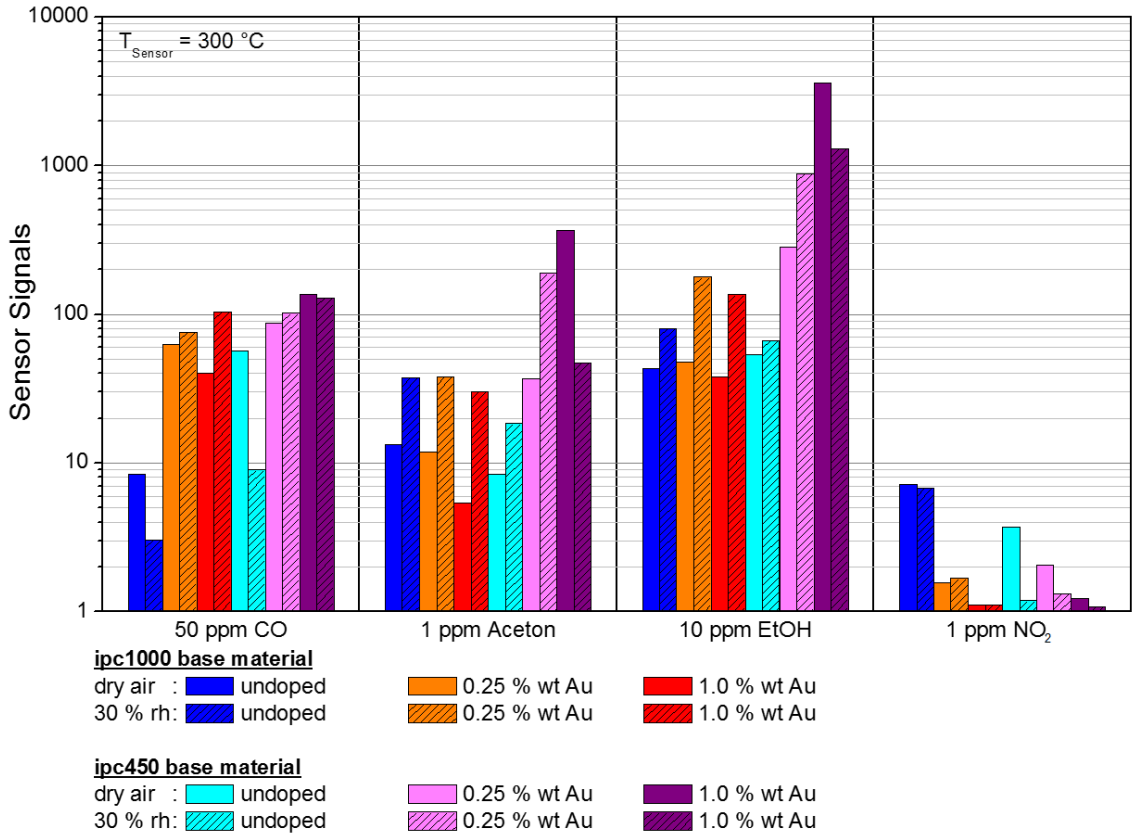

Fig. 48 Gas sensing performance of undoped and Au-doped SnO_2 Materials (SnO_2-LS (1000) and SnO_2-HS (450)).

5.8. Conclusion and Outlook

Au, Pd and AuPd NPs synthesized using a microfluidic reactor were (cf. previous chapters) deposited on SnO_2 (with two different specific surface areas 32.7 and 3.6 $m^2 g^{-1}$) as potential gas sensor materials for detection of CO, CH_4 and VOCs such as toluene and ethanol. The testing conditions were performed in humid and dry air at 300 °C. Compared to undoped SnO_2, Au and Pd NPs increased the sensor signal. However, the AuPd alloy was not successful in the sensor signal enhancement.

During another series of measurements, Au/SnO_2 with different gold loading (0.25 and 1.0 wt.%) and two different specific surface areas of the base SnO_2 materials were tested for CO, NO_2, acetone and ethanol sensing. In most cases, the sensing performance of SnO_2 was improved by doping gold, except for NO_2 detection.

In all the cases above, clearly the composition of the material, metal loading, the test conditions (humid or dry air) and the specific surface area of SnO_2 played important roles

in the performance of the sensors. Overall, doping with monometallic NPs and lower metal loading (0.1 wt.%) on SnO_2-LS provided better results.

In a next step, it would be interesting to investigate the catalytic activity of the same samples used in CO sensing also in CO oxidation and to combine such experiments with *in situ* high-energy-resolution fluorescence detected XAS (HERFD-XAS)[110, 188] in order to identify a mechanism for a deeper interpretation of the sensing data. Moreover, an in-depth study on the particle size and the structure of the samples would be beneficial to draw final conclusions.

6. Microfluidic Synthesis of Cu/ZnO/(Al_2O_3) NPs in a Co-precipitation Reaction[4]

The previous chapters were focused on the microfluidic synthesis of noble metal NPs upon chemical reduction. In this chapter, co-precipitation is introduced as an additional type of reaction to further assess the versatility of the microfluidic chip for synthesis of non-noble based catalysts and, in more general, precipitation reactions. Cu/ZnO/Al_2O_3 nanoparticles, which are especially important for methanol synthesis, were prepared microfluidically and, for comparison, in a conventional way in a batch reactor. The resulting materials were compared with respect to their structural properties.

6.1. Introduction

Methanol (MeOH) is an important industrial bulk chemical which can be used as fuel additive or precursor for clean fuels. Due to its high energy density MeOH is attractive for chemical energy and hydrogen storage. Methanol synthesis has also attracted considerable attention in the context of fuel-cell applications. One important catalyst which has been used extensively for this purpose in the industry is Cu/ZnO/(Al_2O_3)[32, 189-195]. Many studies have been carried out to improve the catalytic activity of these catalysts by a rational design via the preparation method. One standard synthesis technique for the preparation of Cu/ZnO/(Al_2O_3) is co-precipitation of mixed copper, zinc and aluminum hydroxycarbonate (HC) precursor, i.e. introducing a solution containing Cu^{2+}, Zn^{2+} and Al^{3+} salts to a precipitating agent such as sodium carbonate (Na_2CO_3)[36].

Specific synthesis parameters such as pH, temperature, ageing time and mixing conditions play key roles in the resulting catalytic performance. Fundamental studies in this topic conducted by Behrens et al.[36] show that temperatures between 60 °C and 70 °C and pH values between 6-7 are essential to obtain optimum conditions for synthesis of Cu/ZnO/(Al_2O_3) via co-precipitation. Moreover, ageing of the initial precipitate between 30 min to 3 h is beneficial due to meso-structuring of the precipitate. These parameters have a direct influence on the phase formation of zincian malachite $(Cu, Zn)_2(OH)_2CO_3$ which is known to be a high-performance catalyst. Calcination at relatively mild temperatures (326 °C – 426 °C) promotes nano-structuring of the precipitate[31, 36].

[4] Part of this chapter will be submitted to a scientific journal for publication.

Furthermore, high catalytic activity of Cu/ZnO/(Al_2O_3) strongly depends on the surface area of copper (SA_{Cu}) and the amount of reactive interfaces with ZnO in a nanoparticulate and a porous structure[196]. It is worth mentioning that metallic Cu clusters represent the most active sites for methanol synthesis, however, the role of ZnO in this system is not limited to stabilization and distribution of Cu, but also responsible for synergistic effects[31, 197]. Al_2O_3 on the other hand acts as a structural promoter and prevents or slows down thermal sintering of Cu nanoparticles, thereby improving the catalytic activity and stability of the Cu/ZnO active sites[198]. An efficient and homogeneous mixing of metal HC precursor and precipitating agent is crucial to distribute cations uniformly in the primary mixed solution, i.e. a fast micromixing is required which is very difficult to achieve in conventional stirred batch reactors due to imperfect mixing conditions and low mass transfer; e.g. in the case of fast reactions, the reaction process could proceed or be completed before homogeneous mixing of reactants is achieved. Moreover, by applying a dropwise precipitation method in a traditional stirred batch reactor the chemical potential of the reactants cannot be controlled spatially or temporally, i.e. every single drop of reactants is added to a reactor containing a mixture of precipitates and dissolved/unreacted ions with different concentration during the entire process time. During ageing, washing and drying of the catalyst precursor, a variety of different processes such as redissolution, reprecipitation and ion exchange (particularly between the anions e.g. carbonate/hydroxide and hydroxide/nitrate) is possible resulting in deviations of the produced materials' properties from the desired ones. Therefore, co-precipitation in a continuous microflow with short mixing time is essential. In this case, the precipitates are formed in a small volume of solution flowing in a microchannel, and are then collected and post-treated by conventional methods regarding ageing, drying etc. This leads to higher reproducibility of specific properties of the produced catalysts. Advanced micromixing devices such as microfluidic reactors, T-mixers and confined impinging jets reactors have compensated the disadvantages of batch reactors in the recent few years. In order to achieve fast and homogeneous mixing of the reactants, the design of such setups is aimed at obtaining the required high mass transfer and short residence time[198-200].

However, in most reported studies on NP synthesis in microchannel reactors, the concentrations of the metal ions are kept low (< 0.2 mol L^{-1}) in order to avoid severe fouling issues occurring during particle precipitation in the microchannel. Moreover, fabrication of microreactors with complicated features are difficult and expensive[198].

There are only a few published studies on using microfluidic reactors for co-precipitation reactions. The experiments described in this chapter were carried out in order to investigate the performance of the microfluidic chip used in this PhD work with respect to co-precipitation reactions in Cu/ZnO/Al_2O_3 synthesis. However, in this case study syringe pumps were used instead of the fluid delivery rack (section 2) to inject two streams of the reactants separately into the micromixers integrated in the microfluidic chip. For comparison, Cu/ZnO and Cu/ZnO/Al_2O_3 were also produced in a conventional batch reactor under optimum conditions adopted from the literature.

6.2. Microfluidic and Batch Synthesis Procedure

6.2.1. Materials

Copper (II) nitrate trihydrate ($Cu(NO_3)_2 \cdot 3H_2O$, Sigma-Aldrich, >99% purity), zinc nitrate hexahydrate ($Zn(NO_3) \cdot 6H_2O$, Alfa Aesar, 99.99% purity), zinc oxide (ZnO, Fluka, >99% purity), aluminum nitrate nonahydrate ($Al(NO_3)_3 \cdot 9H_2O$, Sigma-Aldrich, >98% purity), sodium carbonate (Na_2CO_3, Sigma-Aldrich, >99.95% purity) and nitric acid (HNO_3, Merck, 65% solution) were used without further purification.

6.2.2. Batch Synthesis of Cu/ZnO and Cu/ZnO/Al_2O_3

Nitrate-derived Cu/ZnO and Cu/ZnO/Al_2O_3 catalysts were synthesized using a co-precipitation process in a batch reactor (Fig. 49). This method adopted from Behrens et al.[36] was applied at constant pH. For the metal nitrate solution 21.6 mmol $Cu(NO_3)_2 \cdot 3H_2O$, 9.6 mmol ZnO and 4.4 mmol were dissolved in 38 mL deionized water using 2.5 mL of concentrated nitric acid. The overall concentration [Cu^{2+}+Zn^{2+}+Al^{3+}] was about 1 M. As precipitating agent 23 mL of 1.6 M aqueous solution of Na_2CO_3 was used. The two solutions were injected dropwise into the batch rector using a syringe pump. The batch reactor is a round-bottom flask containing 100 mL deionized water stirring at ca. 65 °C. The flow rates for injecting metal precursor and precipitating agent solutions were 1 and 0.56 mL min^{-1}, respectively. The pH of the precipitate was kept constant at 6-7. Afterwards, the precipitate was aged for 3 h and filtered and washed several times. This process was followed by drying overnight at 70 °C and calcining at 330 °C for 3 h. One synthesis resulted in 2 g catalyst (in the case of Cu/ZnO the same procedure was applied, more details cf. Table 11).

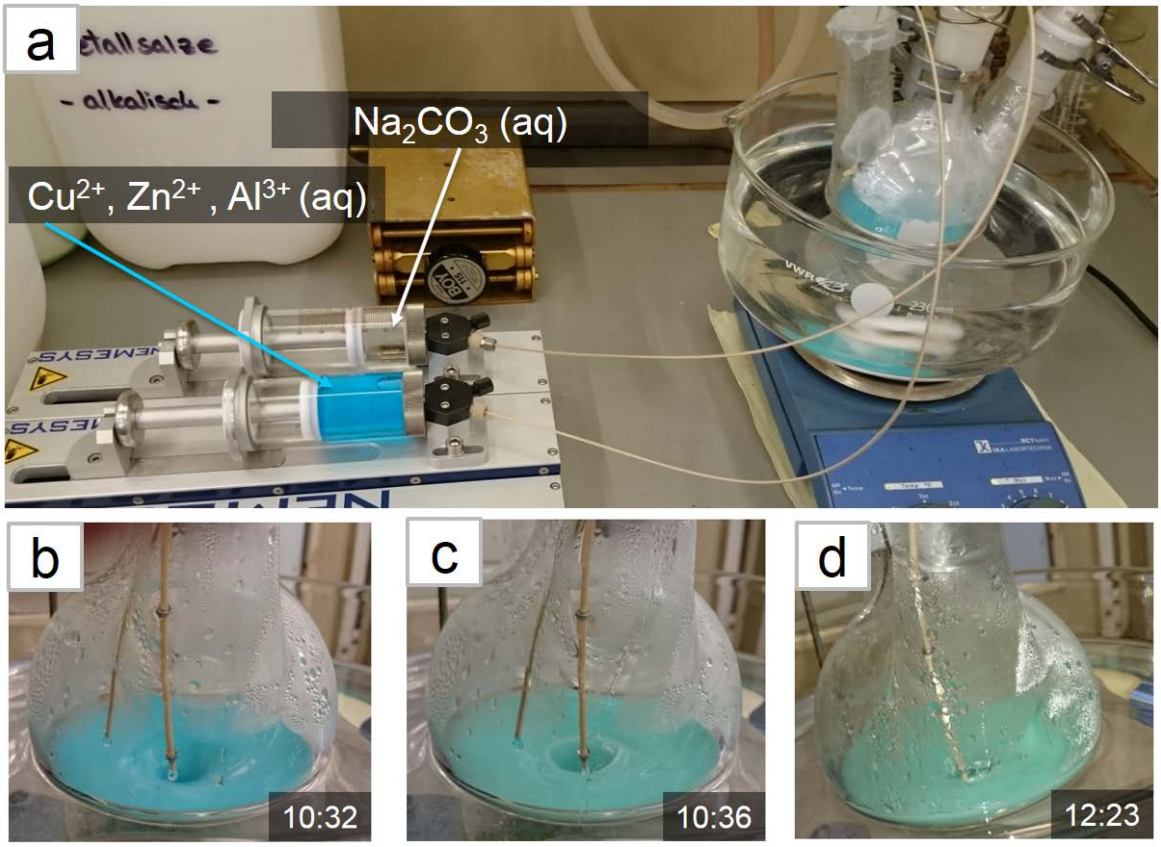

Fig. 49 a) Batch synthesis of Cu/ZnO/Al_2O_3 via co-precipitation at constant pH, b-d) color change during precipitation (the starting time of the reactant injection at 10:10).

6.2.3. Microfluidic Synthesis of Cu/ZnO/Al_2O_3

Nitrate-derived ternary Cu/ZnO/Al_2O_3 catalysts were prepared by co-precipitation of aqueous metal nitrates with Na_2CO_3 using the microfluidic chip (Fig. 50). A metal nitrate solution with a Cu:Zn:Al molar ratio of 60:30:10 was prepared by dissolving the precursors in 40 ml deionized water (total metal ion concentration 0.3 M). 1 ml concentrated nitric acid was added to the solution yielding pH 1. The sodium carbonate concentration was 0.36 M. Both reactant solutions (each 40 mL) were loaded in to separate syringes and then injected each at a flow rate of 22 mL min^{-1} into the microfluidic chip. The precipitate was then filled into a flask containing 100 mL deionized water stirring at 66 °C. After about 15 min, a color change from blue to green was observed (as seen during reactions in the batch reactor). The pH of the precipitate was constant at 6-7, and the same ageing, washing, drying and calcination conditions as in section 6.2.2 were applied. One synthesis resulted in 0.8 g catalyst.

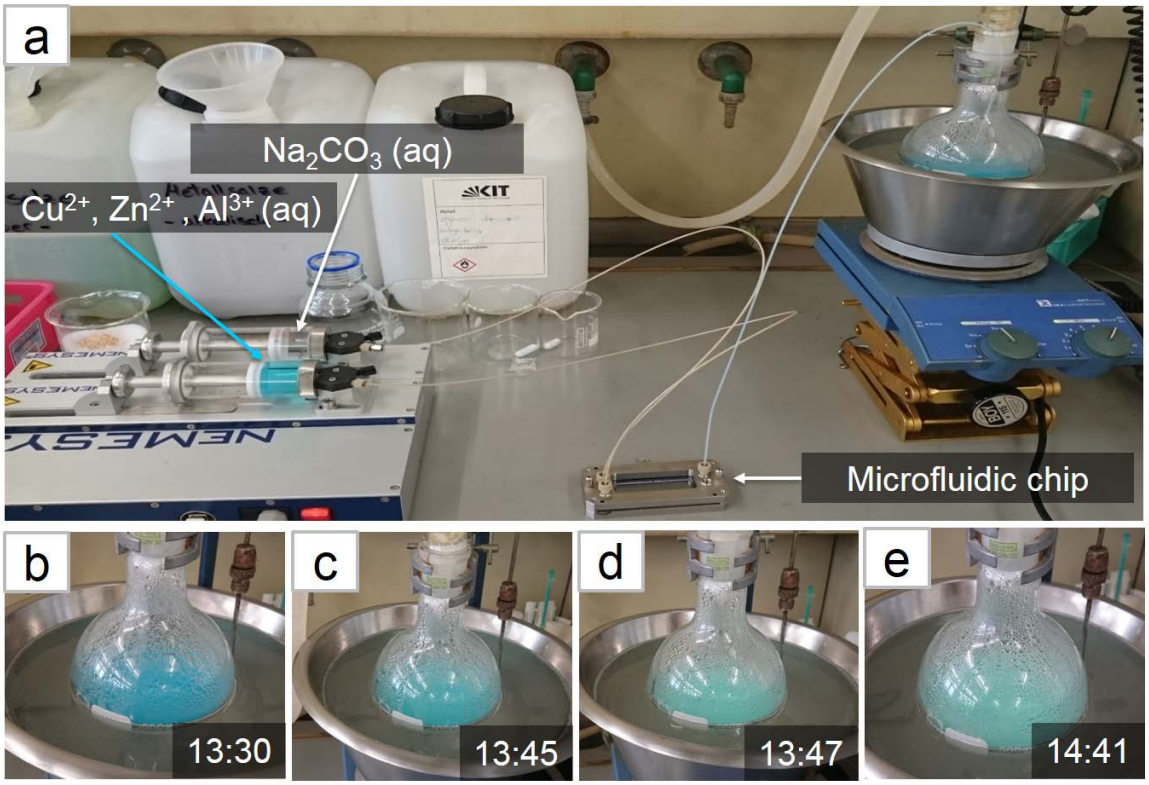

Fig. 50 a) Microfluidic synthesis of Cu/ZnO/Al_2O_3 via co-precipitation at constant pH and a flow rate of 44 mL min^{-1}, b-e) color change during precipitation (the starting time of the reactant injection at 13:20).

Table 11 Preparation of the reactants for co-precipitation of Cu/ZnO/(Al_2O_3)

Catalyst	Synthesis Technique	Metal precursor (mmol)			Na_2CO_3 (mmol)
		Cu^{2+}	Zn^{2+}	Al^{3+}	
Cu/ZnO	Batch reactor	21.6	9.6	-	36.8
Cu/ZnO/Al_2O_3	Batch reactor	21.6	9.6	4.4	36.8
Cu/ZnO/Al_2O_3	Microfluidic reactor	7.2	3.6	1.2	14.4

The amount of deionized water for dissolving the metal precursors and precipitating agent for batch reactor synthesis was 38 and 23 mL, and for microfluidic synthesis 40 and 40 mL, respectively.

6.3. Comparison of Cu/ZnO/(Al_2O_3) Produced in the Microfluidic and Batch Reactor

Hydrocarbonate precursors of ternary CuZnAl co-precipitated at constant pH in the magnetically stirred-batch reactor and the microfluidic reactor were analyzed by XRD after ageing in mother liquor, washing and drying (i.e. uncalcined). The resulting XRD patterns (Fig. 51) clearly show reflections of zincian malachite in both cases, however in the XRD data of the CuZnAl precipitates prepared in the batch reactor reflections of gerhardtite

$[Cu_2(OH)_3NO_3]$ was also observed[36]. In the XRD patterns of precipitates from microfluidic synthesis, the presence of rosasite with poor crystallinity was also detected[198]. The formation of different phases in batch and microreactor could be related to the micromixing effect (homogeneous mixing in short time) and the spatially controlled nucleation of the primary precipitates in small volumes flowing in the microchannel.

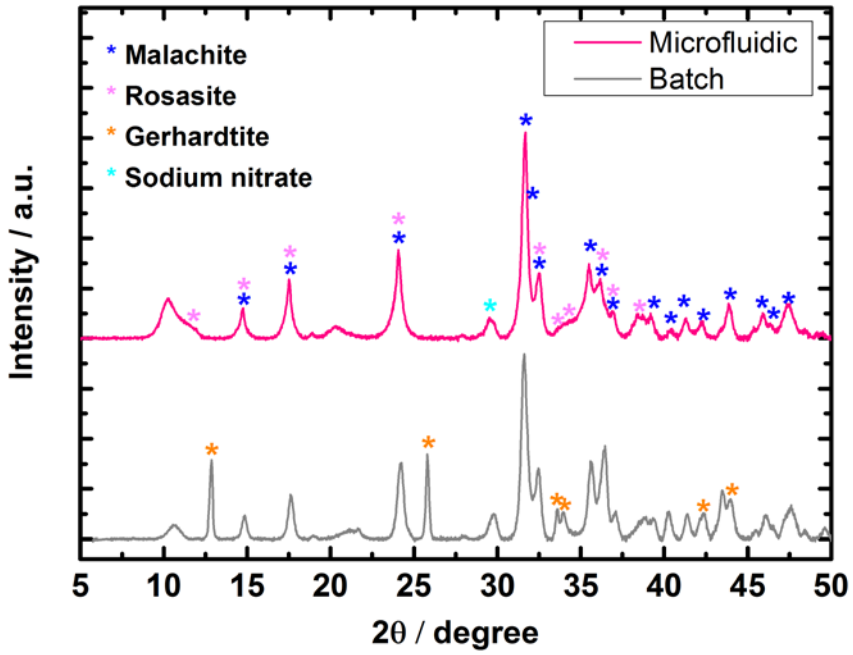

Fig. 51 XRD patterns of the uncalcined ternary CuZnAl precipitates prepared by different methods indicating formation of malachite/rosasite and malachite/gerhardtite phases in precipitates synthesized in microfluidic and batch reactor, respectively.

According to literature[31, 36, 198], the formation of phases during precursor co-precipitation is quite dynamic and during precipitation or even at the end of it other processes such as partial dissolution and reprecipitation reaction can occur. It was reported earlier that such exchange reactions between malachite $[Cu_2(OH)_2CO_3]$ and hydrozincite $[Zn_5(OH)_6(CO_3)_2]$ result in formation of rosasite $[(Cu,Zn)_2(OH)_2CO_3]$ and aurichalcite $[(Cu,Zn)_5(OH)_6(CO_3)_2]$[31, 201-203]. The main reactions occurring during the precipitation process are the following:

$$2Cu^{2+} + CO_3^{2-} + 2OH^- \rightarrow Cu_2(CO_3)(OH)_2$$

$$5Zn^{2+} + 2CO_3^{2-} + 6OH^- \rightarrow Zn_5(CO_3)_2(OH)_6$$

$$2Cu^{2+} + NO_3^- + 3OH^- \rightarrow Cu_2(NO_3)(OH)_3$$

During the ageing process, the following main reactions of exchange reactions, dissolution and reprecipitation proceed:

$Cu_2(NO_3)(OH)_3 + CO_3^{2-} \rightarrow Cu_2(CO_3)(OH)_2 + NO_3^- + OH^-$

$Cu_2(CO_3)(OH)_2 + xZn^{2+} \rightarrow (Cu_{2-x},Zn_x)(CO_3)(OH)_2 + xCu^{2+}$

$Zn_5(CO_3)_2(OH)_6 + xCu^{2+} \rightarrow (Zn_{5-x},Cu_x)(CO_3)_2(OH)_6 + xZn^{2+}$

During post-thermal treatment, rosasite and aurichalcite can decompose into materials with uniform distribution of Cu and Zn hydroxycarbonates and higher catalytic activity. Zhang et al.[190] produced different hydroxycarbonate precipitates containing rosasite and/or aurichalcite with various phase structures during co-precipitation using microimpinging stream reactors (MISR), which showed broader diffraction peaks of malachite or rosasite compared to samples produced in stirred batch reactors. Moreover, in the case of MISR-produced samples the reflection at $2\theta = 31.7°$ was slightly shifted to higher angles indicating contributions of higher amounts of Zn^{2+} to the malachite structure to form rosasite. In other studies it was reported that ZnO nanoparticles act as a stabilizing geometrical spacer between copper particles which inhibiting sintering of Cu particles which are the main catalytic active sites. This works fruitfully if the majority of the Zn atoms were contributing to the zincian malachite precursor phase[36].

In the next step, the ternary CuZnAl precipitates were calcined at 330 °C and investigated again with XRD. Additionally, the calcined Cu/ZnO material produced in the batch reactor was also analyzed. Reflections of Al_2O_3 (at $2\theta = 19°$ and 45°) were not observed due to its amorphous structure[35, 204]. The results in Fig. 52 shows the dominant CuO and ZnO phases in all three samples. In the case of the microfluidically synthesized catalyst, overall the reflections were broader and less intense. The CuO reflection at $2\theta = 38.8°$ in the XRD patterns of CuO/ZnO/Al_2O_3 produced in the microreactor was weaker compared to the sample from the batch reactor indicating smaller CuO crystallites according to the Scherrer equation. In the literature, it was repeatedly reported that small particle sizes and well-distributed copper clusters were important for the catalytic performance (activity and selectivity) in methanol synthesis via hydrogenation of CO/CO_2. Thus, better catalytic performance was expected from CuO/ZnO/Al_2O_3 produced in the microreactor.

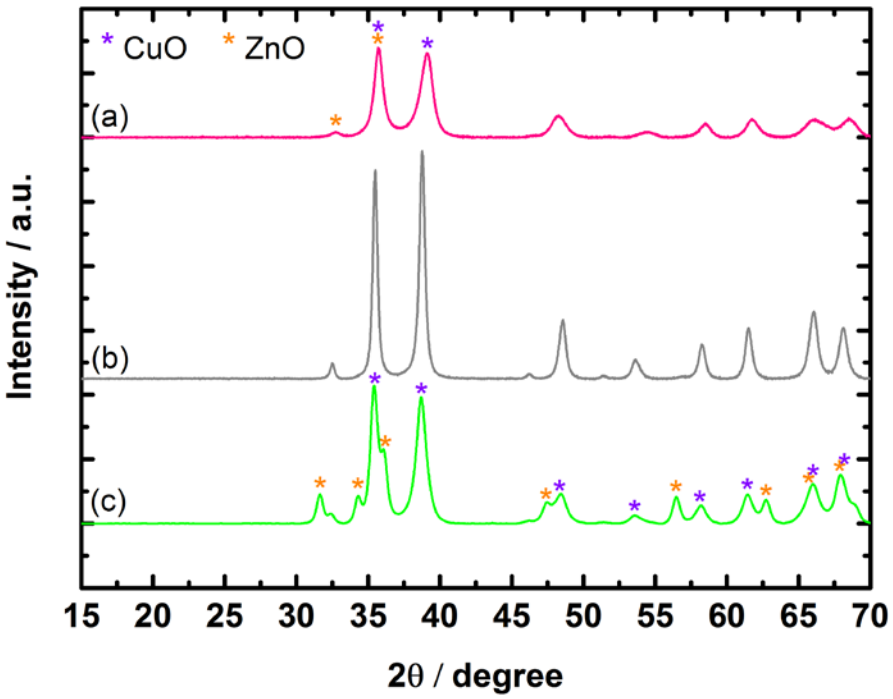

Fig. 52 XRD patterns of the calcined a) CuO/ZnO/Al_2O_3 produced in the microfluidic reactor, b) CuO/ZnO/Al_2O_3 and c) CuO/ZnO produced in a conventional stirred batch reactor.

Table 12 summarizes the main characteristics of the CuO/ZnO/(Al_2O_3) samples prepared by different methods obtained from ICP-OES, BET and chemisorption measurements. Based on the ICP-OES results, the molar Cu:Zn:Al ratios in CuO/ZnO/Al_2O_3 catalysts produced in the microfluidic and batch reactors are similar (77:6:17 and 76:8:16, respectively). This facilitates to compare their catalytic performance directly. In the case of CuO/ZnO catalyst produced from the batch reactor a molar Cu:Zn ratio of 77:23 was obtained.

The BET surface areas of CuO/ZnO/Al_2O_3 synthesized in the batch reactor and the microreactor were 36 $m^2\ g^{-1}$ and 49 $m^2\ g^{-1}$, respectively. Moreover, CuO/ZnO produced in batch reactor had the lowest BET surface area (29 $m^2\ g^{-1}$), which could be due to the absence of alumina.

Temperature programmed reduction (TPR) was applied at KIT-IKFT to study the reduction of copper entities in the three calcined catalysts (CuO/ZnO/Al_2O_3 produced in the microfluidic reactor, CuO/ZnO/Al_2O_3 and CuO/ZnO produced in batch reactor). For this purpose, reduction of the catalysts in N_2O gas, which does not reduce ZnO and Al_2O_3 at the applied temperatures was investigated. As shown in Fig. 53 and 54, in the case of

$CuO/ZnO/Al_2O_3$ catalyst obtained from the batch reactor, the reduction peak (convolution of two peaks at 202 °C and 223 °C) is slightly broader and at higher temperature compared to $CuO/ZnO/Al_2O_3$ catalyst obtained from the microreactor (convolution of two peaks at 196 °C and 215 °C). This indicates a narrower size distribution of CuO particles synthesized in the microreactor. Moreover, in the TPR data of the batch synthesized CuO/ZnO and $CuO/ZnO/Al_2O_3$ a strong shoulder at 136 °C and 164 °C, respectively, suggests various entities of CuO. The reduction temperatures and profiles are similar to those of Cu/Zn/Al systems reported in literature[198]. Table 12 also shows a smaller active particle diameter, higher metallic surface area and higher metal dispersion for $CuO/ZnO/Al_2O_3$ produced in the microreactor.

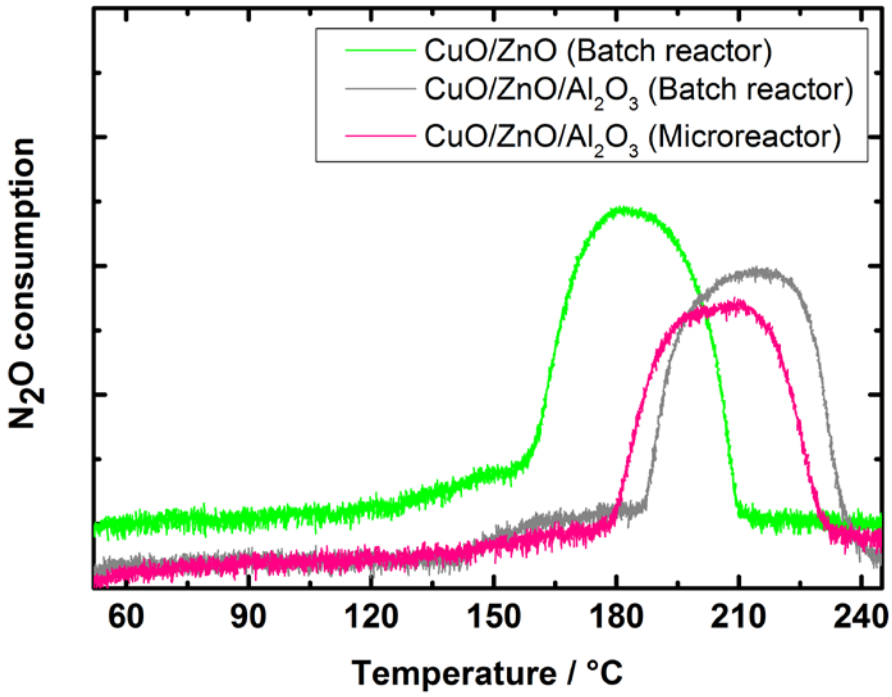

Fig. 53 TPR profiles of the calcined catalysts prepared in the batch and microfluidic reactor.

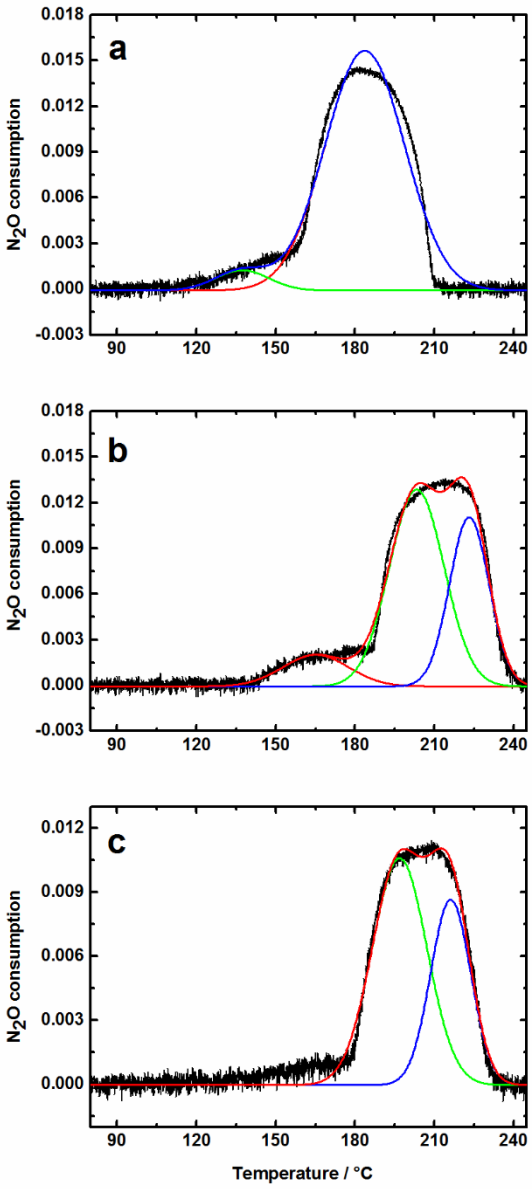

Fig. 54 TPR profiles including curve fittings for of the calcined a) CuO/ZnO and b) CuO/ZnO/Al_2O_3 catalysts produced in conventional stirred batch reactor and c) CuO/ZnO/Al_2O_3 produced in the microfluidic reactor.

Table 12 Characterization of calcined CuO/ZnO and CuO/ZnO/Al_2O_3 produced in the batch and microreactor.

Catalyst	Synthesis technique	ICP-OES (wt.%)			BET (m^2g^{-1})	TPR – N_2O gas		
		Cu	Zn	Al		Metal dispersion (%)	SA_{Cu} (m^2g^{-1})*	Active particle diameter (nm)
Cu/ZnO	Batch reactor	58.9	18.6	-	29	1.6	10.3	65
Cu/ZnO/Al_2O_3	Batch reactor	59.0	6.5	5.2	36	1.5	9.5	71
Cu/ZnO/Al_2O_3	Microreactor	59.2	4.5	5.2	49	2.6	17.0	39.5

*: per gram metal

Finally, the samples were studied by electron microscopy combined with EDX mapping (performed at KIT-INT). Fig. 55 shows STEM and TEM images of calcined CuO/ZnO produced in the batch reactor. TEM measurements combined with EDX mapping (Fig. 56 and Table 13) on several NPs indicated variations in the Cu:Zn ratio in the NPs and a non-uniform CuO and ZnO in the sample.

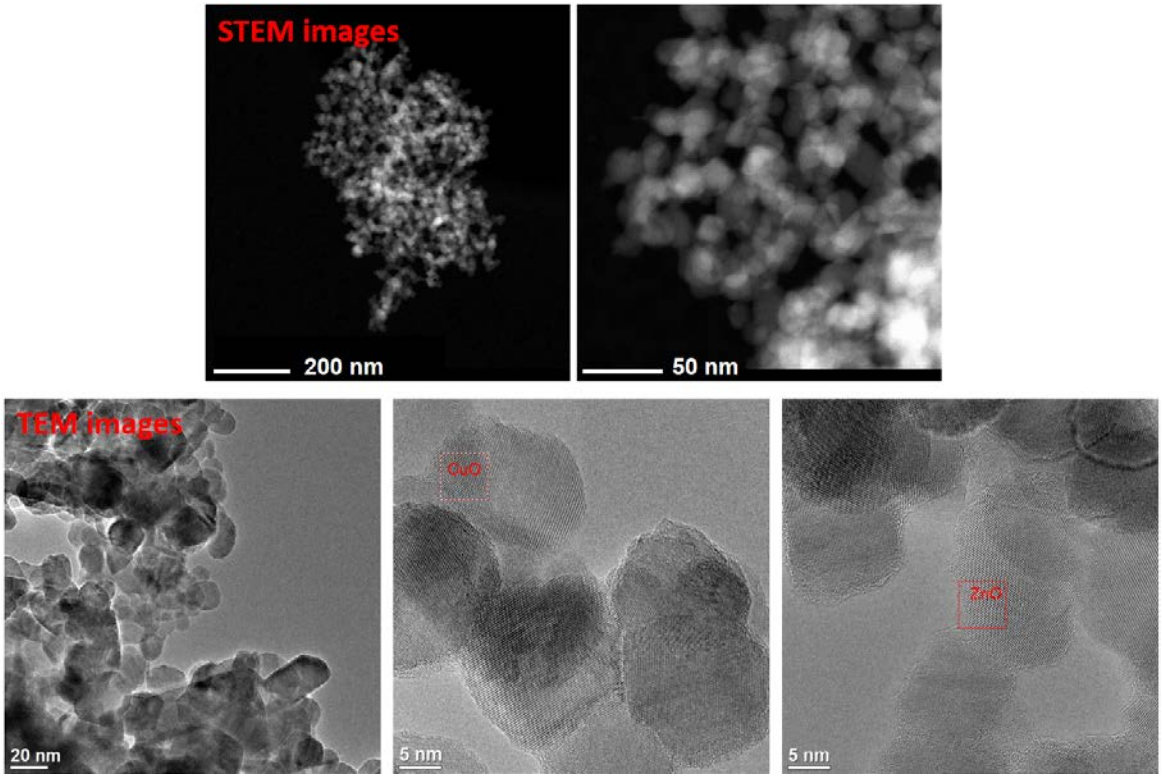

Fig. 55 STEM images (top) and TEM images (bottom) of calcined CuO/ZnO NPs produced in the batch reactor.

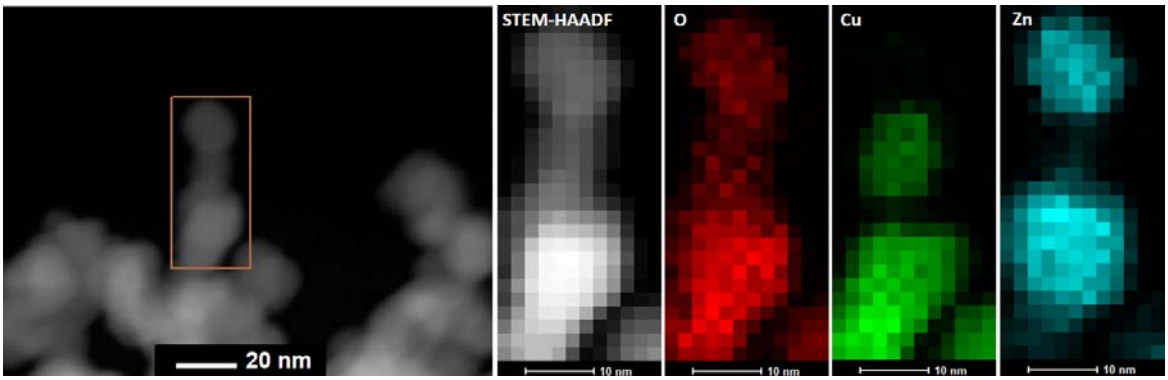

Fig. 56 STEM images and the corresponding elemental maps obtained from STEM-EDX spectrum imaging in the areas marked by the orange box of calcined CuO/ZnO NPs produced in the batch reactor.

Table 13 Quantified EDX results from different regions of the CuO/ZnO catalyst produced in the batch reactor.

Particle No.	O (at.%)	Cu (at.%)	Zn (at.%)	Cu:Zn ratio
1	41.5	47.1	11.4	4.1
2	56.9	23.6	19.4	1.2
3	59.8	22.2	17.9	1.2
4	43.9	33.1	22.9	1.4
5	58.5	30.2	11.3	2.7
6	49.0	37.7	13.3	2.8

The morphology of CuO/ZnO/Al_2O_3 produced in the batch reactor is shown in Fig. 57, while the quantified EDX results of different regions and EDX mappings of single CuO/ZnO/Al_2O_3 NPs produced in the batch reactor showed similar distributions of O, Cu and Zn in NPs of this catalyst, and the Cu:Zn ratio was also similar (Fig.58 and Table 14). The more uniform distribution of metals in this sample could be related to the presence of alumina preventing random sintering of NPs.

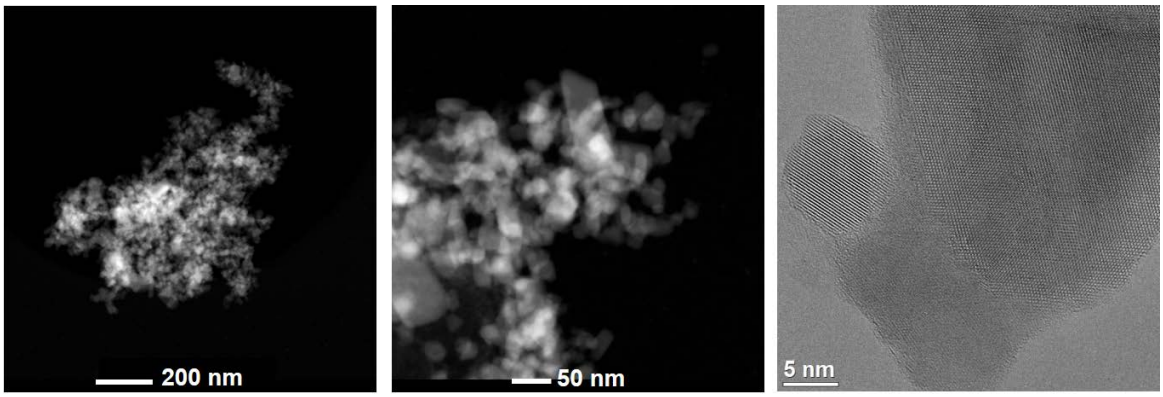

Fig. 57 Images obtained from electron microscopy of calcined CuO/ZnO/Al_2O_3 NPs produced in the batch reactor.

Table 14 Quantified EDX results from different regions of the CuO/ZnO/Al_2O_3 catalyst produced in the batch reactor.

No.	O (at.%)	Al (at.%)	Cu (at.%)	Zn (at.%)	Cu:Zn ratio
1	61.4	1.4	34.9	2.2	15.9
2	58.3	1.0	39.2	1.6	24.5
3	54.3	0.6	43.2	1.8	24.0
4	53.1	0.8	43.9	2.2	20.0
5	57.9	1.4	39.6	2.0	19.8
6	58.6	2.2	36.9	2.2	16.8

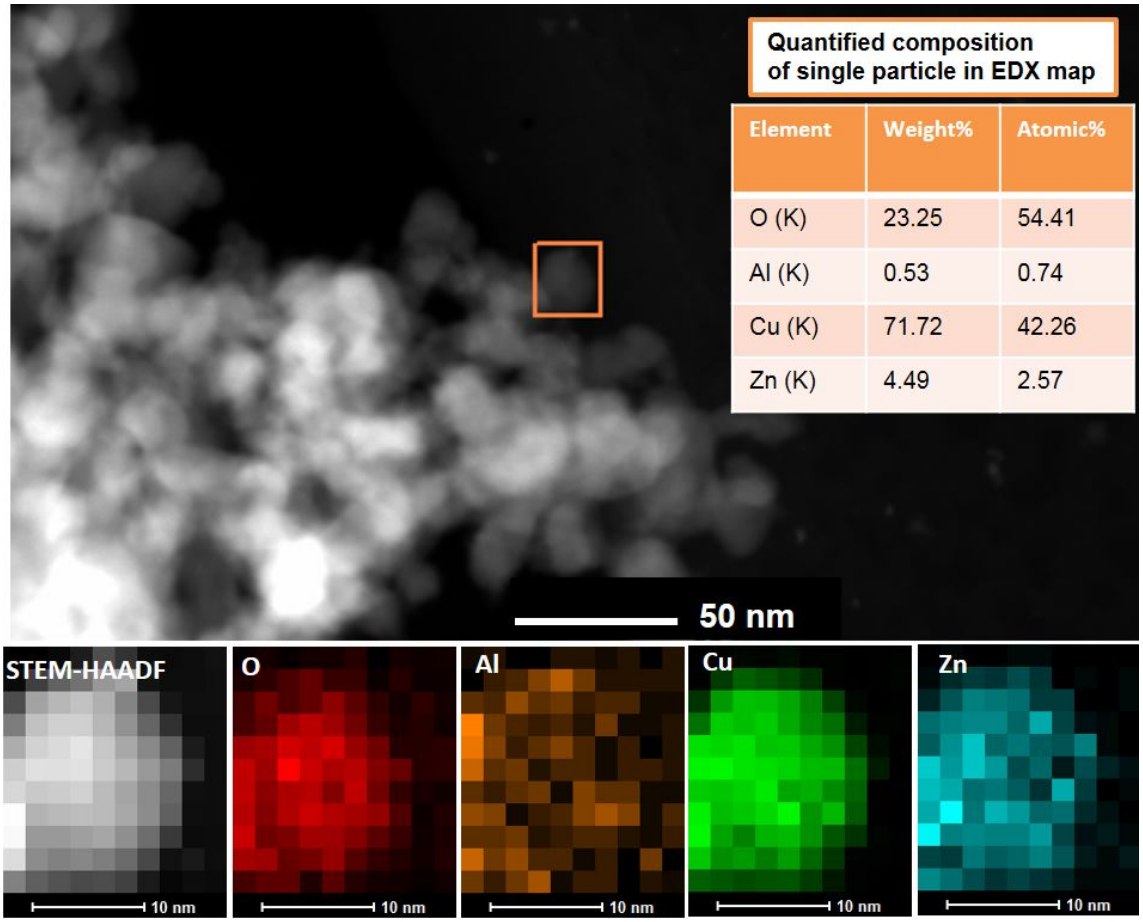

Fig. 58 STEM images and the corresponding elemental maps obtained from STEM-EDX spectrum imaging in the areas marked by orange box of calcined CuO/ZnO/Al_2O_3 NPs produced in the batch reactor.

Fig. 59 shows the morphology of the calcined CuO/ZnO/Al_2O_3 produced in the microfluidic reactor, which seems rather more uniform and fine structured compared to NPs produced in the batch reactor. From the quantified EDX results of different regions and EDX mappings across a single nanoparticle of this sample (Fig. 60 and Table 15), O, Cu and Zn were similarly distributed in the NPs and the Cu:Zn ratio was also similar, but different to the ratio in CuO/ZnO/Al_2O_3 produced in the batch reactor, i.e. the sample produced from microfluidic reactor showed a higher amount of Zn and a lower amount of Cu respectively to those produced in batch reactor. This is slightly different from ICP-OES results, which showed almost the same Cu:Zn ratio in both samples.

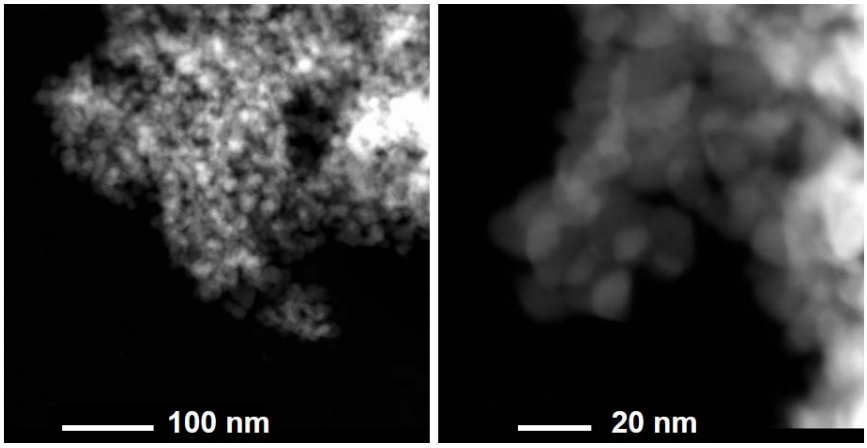

Fig. 59 Images obtained from electron microscopy of calcined CuO/ZnO/Al_2O_3 NPs produced in the microfluidic reactor.

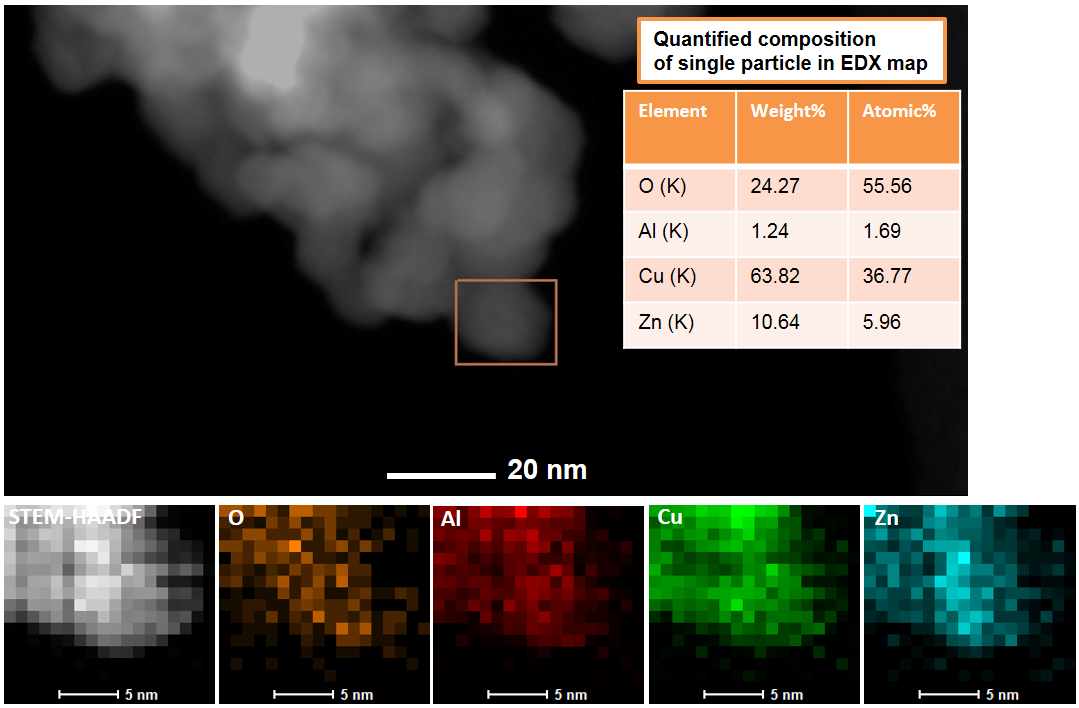

Fig. 60 STEM images and the corresponding elemental maps obtained from STEM-EDX spectrum imaging in the area marked by the orange box of calcined CuO/ZnO/Al_2O_3 NPs produced in the microfluidic reactor.

Table 15 Quantified EDX results from different regions of the CuO/ZnO/Al_2O_3 catalyst produced in the microfluidic reactor.

No.	O (at.%)	Al (at.%)	Cu (at.%)	Zn (at.%)	Cu:Zn ratio
1	67.2	1.7	28.0	3.1	9.0
2	57.8	2.4	36.7	3.2	11.5
3	62.1	9.4	23.9	4.6	5.2
4	52.3	5.9	36.5	5.4	6.8
5	59.3	1.1	35.2	4.4	8.0
6	59.3	3.2	33.6	3.8	8.8

6.4. Conclusion and Outlook

In this study, nitrate-derived CuO/ZnO/(Al_2O_3) catalysts were synthesized using a co-precipitation process in a conventional stirred batch reactor and in a continuously operated microreactor. XRD measurements revealed that, in both materials zincian malachite was the main phase of the precipitated precursor. However, gerhardtite and rosasite phases were also observed in CuO/ZnO/Al_2O_3 synthesized in the batch reactor and microreactor, respectively. After calcination, the sample made in the microreactor showed broader XRD reflections with lower intensity e.g. the reflection of CuO at $2\theta = 38.8°$ was weaker compared to the XRD patterns of the sample from batch reactor indicating smaller CuO crystallites according to the Scherrer equation.

To avoid the heavy deposition of precipitates in the channel and clogging, the precursors were diluted. However, the metal ratio was kept at the same level as for batch synthesis. ICP-OES results indicated similar Cu:Zn:Al ratios for both CuO/ZnO/Al_2O_3 samples, making it easier to compare the results of the catalytic tests directly. TPR studies suggested lower active particle size and higher metal dispersion in the case of the sample produced by microreactor. In this case, the reduction peak was also narrower and showed a maximum at lower temperatures compared to CuO/ZnO/Al_2O_3 produced in the batch reactor. According to standard BET measurements CuO/ZnO/Al_2O_3 produced in the microreactor showed the largest surface area.

Electron microscopy showed a uniform and fine structured morphology for the calcined CuO/ZnO/Al_2O_3 NPs produced in the microfluidic reactor compared to those produced in the batch reactor. EDX mapping and quantified results for the Cu:Zn ratio in the samples showed a homogeneous distribution of metals when Al_2O_3 was present in the samples, and this effect was even more obvious in the case of CuO/ZnO/Al_2O_3 produced in the microfluidic reactor.

As an outlook based on these results, it is also beneficial to study the catalysts by *in situ* XAS during TPR in order to record dynamic reduction/oxidation behaviors of Cu and Zn. Finally, it is planned for the near future to test the catalysts with respect to methanol synthesis to investigate their catalytic performance.

7. Final Remarks – Summary and Outlook

The objective of this work was to explore the potential of a novel microfluidic reactor for advanced synthesis of highly monodisperse nanoparticles (NPs) in a continuous plug-flow at high flow rates, while simultaneously characterizing the particles during formation by *in situ* x-ray absorption spectroscopy. A fluid delivery rack injected the reactants into a microfluidic chip with three integrated cyclone micromixers for efficient mixing of the reactants within a short time (<2 ms), followed by a meandering microchannel. The total residence time of the flow in the microchannel was about 20 ms. In this process, Au and Pd as well as alloyed Au_xPd_y NPs were produced via a fast reduction reaction using $NaBH_4$ in the presence of PVP. A unique feature of the microfluidic setup lies in its suitability for *in situ* spatially and time resolved studies of early stage kinetics of Au NP formation in fast reduction reactions. *In situ* XAS was used to explore NP formation during Au^{3+} reduction to Au^0 by $NaBH_4$ in the presence of PVP. The reaction progress under continuous flow conditions was monitored by recording XAS spectra at different positions along the microchannel with a focused X-ray beam. The results revealed that up to 6 ms there was still a significant contribution of oxidized Au. The reduction to Au^0 was complete within the first 10 ms of this fast reduction reaction and remained unchanged at 18 ms. The role of PVP was to protect the NPs against further growth, and to increase the electrostatic repulsion between metal NPs and the silicon-based channel walls in order to avoid blockage of the channel. Moreover, the channel walls were coated with Ombrello, a commercially available hydrophobic material in order to repel the PVP-stabilized metal particles. The structural and physical properties of the materials thus obtained were compared with NPs produced from the same reactants and surfactant in a conventional stirred batch reactor.

STEM images showed the formation of ultrasmall Au, Pd and Au_xPd_y NPs with average diameters of ca. 1 nm and very narrow size distributions. In the case of NPs produced in the batch reactor, the size distribution was broader. UV-vis spectra showed a strong suppression of the surface resonance band of Au nanoparticles. In the case of Pd containing nanoalloys a Pd chloride peak, indicating unreacted Pd in the reduction process, did not appear in the spectra. XPS data of PVP-stabilized NPs indicated negatively charged Au NPs due to electron transfer from PVP to Au surfaces. High resolution TEM investigations of the AuPd bimetallic samples showed the presence of a single crystal structure in a single Au_xPd_y NP with lattice spacings between those of pure Au and pure Pd, whereas EDX

mapping showed a uniform distribution of Au and Pd in one selected particle, i.e. evidence of AuPd nanoalloys.

As a next step, ultrasmall Au, Pd and Au_xPd_y NPs were deposited on TiO_2 supports with high (370 m^2 g^{-1}/TiO_2-G5) and low (50 m^2 g^{-1}/TiO_2-P25) surface areas for further investigation. It was observed that after deposition on TiO_2 and calcination the colloidal NPs aggregated. Among these samples, Au-rich AuPd alloys on TiO_2 exhibited smaller average nanoparticle sizes (ca. 5 nm) with a narrower size distribution compared to monometallic Au NPs on TiO_2. Obviously alloying with Pd prevents aggregation. In the case of Pd/TiO_2, it was difficult to observe NPs by STEM presumably because they were oxidized during calcination. Furthermore, in the Pd-rich alloy (Au_3Pd_7/TiO_2) a segregated contiguous Pd layer around the NPs was detected by combined STEM and EDX mapping.

Au L_3-edge XANES and EXAFS data obtained from Au/TiO_2 and Au_xPd_y/TiO_2 pellet samples exhibited variations in the white line intensity which could be correlated to the degree of alloying between Au and Pd in these NPs. Apparently, Au–Pd alloying caused a decrease in white line intensity. The shape and amplitude of the EXAFS oscillations in Au L_3- and Pd K-edge XAS spectra varied with increasing concentration of the second metal. In the case of bimetallic NPs, the peaks in the Fourier-transformed EXAFS data were shifted, indicating a change in the lattice constant due to alloy formation. The ratio of the Au-Au and Au-Pd coordination numbers extracted from Au L_3 EXAFS spectra indicated formation of a homogeneous alloy. Moreover, coordination numbers obtained from Pd K-EXAFS data analysis revealed the formation of a homogeneous mixture of Au and Pd in these AuPd NPs with either Pd dominating at the NP surface or segregated on the titania support.

In situ XAS data of the calcined Pd/TiO_2 and AuPd/TiO_2 proved the presence of oxidized Pd in a temperature range between 25-400 °C under inert conditions. By employing a novel UHV-FTIR apparatus, the surface of the materials was analyzed using CO as probe molecule at specific temperatures in order to identify different surface entities such as Ti^{4+}, Au^0, Pd^{2+}, atop Pd^0 and bridge Pd^0 (in alloyed or monometallic structures). In the case of monometallic Au and Pd NPs, Au^0 and Pd^{2+} cations were identified as most abundant species. Bimetallic Au_xPd_y NPs however behaved differently compared to the monometallic particles. In bimetallic Au_xPd_y NPs, Au^0, atop Pd^0 and bridge Pd^0 dominated, depending on the Au:Pd ratio. Moreover, a shift in the CO stretching frequencies indicated

a charge transfer from Au to Pd^{2+} and reduction to Pd^0 on the catalyst surface. In the case of Au_3Pd_7, also some Pd^{2+} was observed which could be related to the lower amount of Au in the NPs or attributed to the segregated Pd layer around the nanoparticles on the support.

Catalytic tests of the samples with respect to CO oxidation showed that Au/TiO_2 was the most active catalyst, especially at room temperature. Pd/TiO_2 as the least active catalyst and Au_xPd_y/TiO_2 in between, showing some synergistic effects at higher temperatures (Au_3Pd_7/TiO_2 exhibited the highest catalytic activity for CO oxidation and synergistic effects). Nevertheless, these results could be beneficial for fine-tuning the catalytic of these materials.

Furthemore microfluidically synthesized Au, Pd and AuPd alloy NPs were supported on SnO_2 for potential application in sensing CO, CH_4 and VOCs such as toluene and ethanol. The sensing behavior was affected by the metal loading, the surface area of the support, the NP material and humidity. Compared to undoped SnO_2, Au and Pd NPs increased the sensor signal. However, unlike the monometallics, the AuPd alloy could not enhance the sensor signal. Overall, doping SnO_2 with monometallic NPs, lower metal loading (0.1 wt.%) and low surface area (3.6 $m^2\ g^{-1}$) provided better results.

Synthesis of $CuO/ZnO/Al_2O_3$ in the microfluidic chip (with syringe pumps) demonstrated efficient mixing of the reactants in this device in a co-precipitation process. In parallel, $CuO/ZnO/(Al_2O_3)$ materials were prepared in a conventional batch reactor without micromixers. XRD measurements revealed that in the materials obtained from both the batch and the microreactor, the main phase of the precipitated precursor was zincian malachite. However, gerhardtite and rosasite phases were also observed. After calcination, the sample prepared in the microreactor showed broader XRD reflections with lower intensity compared to the XRD patterns of the sample from the batch reactor, indicating smaller CuO crystallites. TPR studies suggested smaller active particle size and higher metal dispersion in the case of the sample produced in the microreactor. STEM images combined with EDX showed a uniform morphology and a homogeneous distribution of Cu/Zn/Al in the calcined $CuO/ZnO/Al_2O_3$ NPs produced in the microfluidic reactor compared to those obtained from the batch reactor.

As a final conclusion, the microfluidic setup developed for this study was successfully used to produce small NPs with uniform structure and narrow size distribution in reduction and co-precipitation reactions, and also contributed to a mechanistic understanding of the

nanoparticle formation in reduction reactions allowing for future optimization of advanced microfluidically synthesized materials. Furthermore, this study shows the high potential of synchrotron-based techniques, providing unique insights into materials at work in the field of chemistry, physics, materials science and engineering. The reported experimental procedures allow obtaining new data on the advanced materials technologies and chemical reactions and are not only limited to heterogeneous catalysis. The results of this work are of high relevance for research at the interface of chemistry and engineering.

The experimental results reported here provide a solid basis for further studies which can be highly beneficial in nanomaterials research. As a first step, the nanoparticles produced so far in the microfluidic reactor could be tested with respect to diverse applications, e.g. AuPd/TiO_2 for direct H_2O_2 synthesis, AuPd/SnO_2 as sensing materials and Cu/ZnO_2/Al_2O_3 for synthesis of methanol and dimethylether (DME). These activity and performance studies would provide valuable information, especially in combination with *in situ* and *operando* X-ray absorption spectroscopic studies to derive further information about the influence of the preparation parameters. An important prerequisite in the case of small noble metal nanoparticles is their fixation on supports without further aggregation.

The versatility of the microfluidic setup used for this dissertation allows variations of different synthesis parameters such as reactant concentrations and flow rates, pH values and the use of different surfactants. The potential of this setup could be further exploited by preparing a variety of metallic nanoparticles with different chemical compositions and structures, including e.g. core-shell catalysts. Furthermore, apart from the first *in situ* XAS measurements reported in this thesis, a more detailed EXAFS investigation, small angle X-ray scattering measurements and related characterization studies would be helpful to gain an insight into the different stages of particle growth.

As a future upgrade of the microfluidic apparatus the integration of a heating element in the microfluidic chip would be a highly interesting option opening new perspectives for experiments using this unique device.

Bibliography

1. I. Chorkendorff and J. W. Niemantsverdriet, *Concepts of modern catalysis and kinetics*, John Wiley & Sons, 2017.
2. M. Haruta, Size-and support-dependency in the catalysis of gold, *Catal. Today*, 1997, **36**, 153-166.
3. J.-D. Grunwaldt, C. Kiener, C. Wögerbauer and A. Baiker, Preparation of supported gold catalysts for low-temperature CO oxidation via "size-controlled" gold colloids, *J. Catal.*, 1999, **181**, 223-232.
4. M. Okumura, T. Fujitani, J. Huang and T. Ishida, A career in catalysis: Masatake Haruta, *ACS Catal.*, 2015, **5**, 4699-4707.
5. A. Roucoux, J. Schulz and H. Patin, Reduced transition metal colloids: a novel family of reusable catalysts?, *Chem. Rev.*, 2002, **102**, 3757-3778.
6. C.-J. Jia and F. Schüth, Colloidal metal nanoparticles as a component of designed catalyst, *Phys. Chem. Chem. Phys.*, 2011, **13**, 2457-2487.
7. M. Haruta, A. Ueda, S. Tsubota and R. T. Sanchez, Low-temperature catalytic combustion of methanol and its decomposed derivatives over supported gold catalysts, *Catal. Today*, 1996, **29**, 443-447.
8. A. Zwijnenburg, A. Goossens, W. G. Sloof, M. W. Crajé, A. M. van der Kraan, L. Jos de Jongh, M. Makkee and J. A. Moulijn, XPS and Mössbauer characterization of Au/TiO_2 propene epoxidation catalysts, *J. Phys. Chem. B*, 2002, **106**, 9853-9862.
9. Q. Yao, C. Wang, H. Wang, H. Yan and J. Lu, Revisiting the Au particle size effect on TiO_2-coated Au/TiO_2 catalysts in CO oxidation reaction, *J. Phys. Chem. C*, 2016, **120**, 9174-9183.
10. B. Hammer and J. Nørskov, Why gold is the noblest of all the metals, *Nature*, 1995, **376**, 238-240.
11. R. Meyer, C. Lemire, S. K. Shaikhutdinov and H.-J. Freund, Surface chemistry of catalysis by gold, *Gold Bull.*, 2004, **37**, 72-124.
12. S. Tsubota, T. Nakamura, K. Tanaka and M. Haruta, Effect of calcination temperature on the catalytic activity of Au colloids mechanically mixed with TiO_2 powder for CO oxidation, *Catal. Lett.*, 1998, **56**, 131-135.
13. M. Haruta, Novel catalysis of gold deposited on metal oxides, *Catal. Surv. Jpn*, 1997, **1**, 61-73.
14. A. Corma and H. Garcia, Supported gold nanoparticles as catalysts for organic reactions, *Chem. Soc. Rev.*, 2008, **37**, 2096-2126.
15. G. J. Hutchings and M. Haruta, A golden age of catalysis: A perspective, *Appl. Catal. A: Gen.*, 2005, **291**, 2-5.
16. A. S. K. Hashmi and G. J. Hutchings, Gold catalysis, *Angew. Chem. Int. Ed.*, 2006, **45**, 7896-7936.
17. A. Villa, D. Wang, D. S. Su and L. Prati, New challenges in gold catalysis: bimetallic systems, *Catal. Sci. Technol.*, 2015, **5**, 55-68.
18. R. Ferrando, J. Jellinek and R. L. Johnston, Nanoalloys: from theory to applications of alloy clusters and nanoparticles, *Chem. Rev.*, 2008, **108**, 845-910.
19. K. Zarschler, L. Rocks, N. Licciardello, L. Boselli, E. Polo, K. P. Garcia, L. De Cola, H. Stephan and K. A. Dawson, Ultrasmall inorganic nanoparticles: State-of-the-art and perspectives for biomedical applications, *Nanomedicine*, 2016, **12**, 1663-1701.
20. B. H. Kim, M. J. Hackett, J. Park and T. Hyeon, Synthesis, characterization, and application of ultrasmall nanoparticles, *Chem. Mater.*, 2013, **26**, 59-71.

21. J. R. McBride, A. D. Dukes, M. A. Schreuder and S. J. Rosenthal, On ultrasmall nanocrystals, *Chem. Phys. Lett.*, 2010, **498**, 1-9.
22. P. Zhao, N. Li and D. Astruc, State of the art in gold nanoparticle synthesis, *Coord. Chem. Rev.*, 2013, **257**, 638-665.
23. H. Bönnemann and R. M. Richards, Nanoscopic metal particles − synthetic methods and potential applications, *Eur. J. Inorg. Chem.*, 2001, **2001**, 2455-2480.
24. S. Wang, Copper colloid-based catalysts for methanol synthesis, Disseration, Ruhr Universität Bochum, 2013.
25. M. Luty-Błocho, K. Fitzner, V. Hessel, P. Löb, M. Maskos, D. Metzke, K. Pacławski and M. Wojnicki, Synthesis of gold nanoparticles in an interdigital micromixer using ascorbic acid and sodium borohydride as reducers, *Chem. Eng. J.*, 2011, **171**, 279-290.
26. J. Turkevich and G. Kim, Palladium: preparation and catalytic properties of particles of uniform size, *Science*, 1970, **169**, 873-879.
27. J. Turkevich, P. C. Stevenson and J. Hillier, A study of the nucleation and growth processes in the synthesis of colloidal gold, *Discuss. Faraday Soc.*, 1951, **11**, 55-75.
28. T. Teranishi and M. Miyake, Size control of palladium nanoparticles and their crystal structures, *Chem. Mater.*, 1998, **10**, 594-600.
29. H. Tsunoyama, N. Ichikuni and T. Tsukuda, Microfluidic synthesis and catalytic application of pvp-stabilized,~ 1 nm gold clusters, *Langmuir*, 2008, **24**, 11327-11330.
30. H. Tsunoyama, H. Sakurai, Y. Negishi and T. Tsukuda, Size-specific catalytic activity of polymer-stabilized gold nanoclusters for aerobic alcohol oxidation in water, *J. Am. Chem. Soc.*, 2005, **127**, 9374-9375.
31. M. Behrens and R. Schlögl, How to prepare a good Cu/ZnO catalyst or the role of solid state chemistry for the synthesis of nanostructured catalysts, *Z. Anorg. Allg. Chem.*, 2013, **639**, 2683-2695.
32. C. Kiener, M. Kurtz, H. Wilmer, C. Hoffmann, H.-W. Schmidt, J.-D. Grunwaldt, M. Muhler and F. Schüth, High-throughput screening under demanding conditions: Cu/ZnO catalysts in high pressure methanol synthesis as an example, *J. Catal.*, 2003, **216**, 110-119.
33. C. Baltes, S. Vukojević and F. Schüth, Correlations between synthesis, precursor, and catalyst structure and activity of a large set of $CuO/ZnO/Al_2O_3$ catalysts for methanol synthesis, *J. Catal.*, 2008, **258**, 334-344.
34. G. Chinchen, P. Denny, J. Jennings, M. Spencer and K. Waugh, Synthesis of methanol: part 1. Catalysts and kinetics, *Appl. Catal.*, 1988, **36**, 1-65.
35. M. Behrens, Meso-and nano-structuring of industrial $Cu/ZnO/(Al_2O_3)$ catalysts, *J. Catal.*, 2009, **267**, 24-29.
36. M. Behrens, D. Brennecke, F. Girgsdies, S. Kißner, A. Trunschke, N. Nasrudin, S. Zakaria, N. F. Idris, S. B. A. Hamid and B. Kniep, Understanding the complexity of a catalyst synthesis: co-precipitation of mixed Cu, Zn, Al hydroxycarbonate precursors for $Cu/ZnO/Al_2O_3$ catalysts investigated by titration experiments, *Appl. Catal. A: Gen.*, 2011, **392**, 93-102.
37. M. Behrens, Coprecipitation: An excellent tool for the synthesis of supported metal catalysts–From the understanding of the well known recipes to new materials, *Catal. Today*, 2015, **246**, 46-54.
38. J.-L. Li and T. Inui, Characterization of precursors of methanol synthesis catalysts, copper/zinc/aluminum oxides, precipitated at different pHs and temperatures, *Appl. Catal. A: Gen.*, 1996, **137**, 105-117.

39. G. Tofighi, H. Lichtenberg, J. Pesek, T. L. Sheppard, W. Wang, L. Schöttner, G. Rinke, R. Dittmeyer and J.-D. Grunwaldt, Continuous microfluidic synthesis of colloidal ultrasmall gold nanoparticles: in situ study of the early reaction stages and application for catalysis, *React. Chem. Eng.*, 2017, **2**, 876-884.
40. J. Wagner, T. Kirner, G. Mayer, J. Albert and J. Köhler, Generation of metal nanoparticles in a microchannel reactor, *Chem. Eng. J.*, 2004, **101**, 251-260.
41. T. Ishizaka, A. Ishigaki, H. Kawanami, A. Suzuki and T. M. Suzuki, Dynamic control of gold nanoparticle morphology in a microchannel flow reactor by glucose reduction in aqueous sodium hydroxide solution, *J. Colloid Interface Sci.*, 2012, **367**, 135-138.
42. J.-Y. Ruzicka, F. Abu Bakar, C. Hoeck, R. Adnan, C. McNicoll, T. Kemmitt, B. C. Cowie, G. F. Metha, G. G. Andersson and V. B. Golovko, Toward control of gold cluster aggregation on TiO_2 via surface treatments, *J. Phys. Chem. C*, 2015, **119**, 24465-24474.
43. J.-D. Grunwaldt and C. G. Schroer, Hard and soft X-ray microscopy and tomography in catalysis: bridging the different time and length scales, *Chem. Soc. Rev.*, 2010, **39**, 4741-4753.
44. H. Jun, T. Fabienne, M. Florent, P.-E. Coulon, M. Nicolas and S. Olivier, Understanding of the size control of biocompatible gold nanoparticles in millifluidic channels, *Langmuir*, 2012, **28**, 15966-15974.
45. J. Polte, R. Erler, A. F. Thunemann, S. Sokolov, T. T. Ahner, K. Rademann, F. Emmerling and R. Kraehnert, Nucleation and growth of gold nanoparticles studied via in situ small angle X-ray scattering at millisecond time resolution, *ACS Nano*, 2010, **4**, 1076-1082.
46. B. Abécassis, F. Testard, Q. Kong, B. Francois and O. Spalla, Influence of monomer feeding on a fast gold nanoparticles synthesis: time-resolved XANES and SAXS experiments, *Langmuir*, 2010, **26**, 13847-13854.
47. B. Abécassis, F. Testard, O. Spalla and P. Barboux, Probing in situ the nucleation and growth of gold nanoparticles by small-angle X-ray scattering, *Nano Lett.*, 2007, **7**, 1723-1727.
48. J. Bolze, B. Peng, N. Dingenouts, P. Panine, T. Narayanan and M. Ballauff, Formation and growth of amorphous colloidal $CaCO_3$ precursor particles as detected by time-resolved SAXS, *Langmuir*, 2002, **18**, 8364-8369.
49. T. Yao, Z. Sun, Y. Li, Z. Pan, H. Wei, Y. Xie, M. Nomura, Y. Niwa, W. Yan and Z. Wu, Insights into initial kinetic nucleation of gold nanocrystals, *J. Am. Chem. Soc.*, 2010, **132**, 7696-7701.
50. J. I. Park, A. Saffari, S. Kumar, A. Günther and E. Kumacheva, Microfluidic synthesis of polymer and inorganic particulate materials, *Annu. Rev. Mater. Res.*, 2010, **40**, 415-443.
51. M. T. Rahman and E. V. Rebrov, Microreactors for gold nanoparticles synthesis: from Faraday to flow, *Processes*, 2014, **2**, 466-493.
52. G. M. Whitesides, The origins and the future of microfluidics, *Nature*, 2006, **442**, 368-373.
53. M. Luty-Błocho, M. Wojnicki, K. Pacławski and K. Fitzner, The synthesis of platinum nanoparticles and their deposition on the active carbon fibers in one microreactor cycle, *Chem. Eng. J.*, 2013, **226**, 46-51.
54. K. Pacławski, B. Streszewski, W. Jaworski, M. Luty-Błocho and K. Fitzner, Gold nanoparticles formation via gold (III) chloride complex ions reduction with glucose in the batch and in the flow microreactor systems, *Colloids Surf. A*, 2012, **413**, 208-215.

55. J. Wagner and J. Köhler, Continuous synthesis of gold nanoparticles in a microreactor, *Nano Lett.*, 2005, **5**, 685-691.
56. A. Günther and K. F. Jensen, Multiphase microfluidics: from flow characteristics to chemical and materials synthesis, *Lab Chip*, 2006, **6**, 1487-1503.
57. J. Wagner, T. Tshikhudo and J. Köhler, Microfluidic generation of metal nanoparticles by borohydride reduction, *Chem. Eng. J.*, 2008, **135**, S104-S109.
58. T. Kirner, J. Albert, M. Günther, G. Mayer, K. Reinhäckel and J. Köhler, Static micromixers for modular chip reactor arrangements in two-step reactions and photochemical activated processes, *Chem. Eng. J.*, 2004, **101**, 65-74.
59. J. Köhler, L. Abahmane, J. Wagner, J. Albert and G. Mayer, Preparation of metal nanoparticles with varied composition for catalytical applications in microreactors, *Chem. Eng. Sci.*, 2008, **63**, 5048-5055.
60. A. Knauer, A. Thete, S. Li, H. Romanus, A. Csaki, W. Fritzsche and J. Köhler, Au/Ag/Au double shell nanoparticles with narrow size distribution obtained by continuous micro segmented flow synthesis, *Chem. Eng. J.*, 2011, **166**, 1164-1169.
61. H. Song, J. D. Tice and R. F. Ismagilov, A microfluidic system for controlling reaction networks in time, *Angew. Chem.*, 2003, **115**, 792-796.
62. A. Balerna and S. Mobilio, in *Synchrotron Radiation: Basics, Methods and Applications*, eds. S. Mobilio, F. Boscherini and C. Meneghini, Springer Berlin Heidelberg, Berlin, Heidelberg, 2015, DOI: 10.1007/978-3-642-55315-8_1, pp. 3-28.
63. G. Cheng, J. D. Carter and T. Guo, Investigation of Co nanoparticles with EXAFS and XANES, *Chem. Phys. Lett.*, 2004, **400**, 122-127.
64. A. M. Beale and B. M. Weckhuysen, EXAFS as a tool to interrogate the size and shape of mono and bimetallic catalyst nanoparticles, *Phys. Chem. Chem. Phys.*, 2010, **12**, 5562-5574.
65. A. I. Frenkel, Applications of extended X-ray absorption fine-structure spectroscopy to studies of bimetallic nanoparticle catalysts, *Chem. Soc. Rev.*, 2012, **41**, 8163-8178.
66. H. Modrow, Tuning nanoparticle properties—The X-ray absorption spectroscopic point of view, *Appl. Spectrosc. Rev.*, 2004, **39**, 183-290.
67. D. E. Sayers, E. A. Stern and F. W. Lytle, New technique for investigating noncrystalline structures: Fourier analysis of the extended X-ray absorption fine structure, *Phys. Rev. Lett.*, 1971, **27**, 1204-1207.
68. G. Hofmann, G. Tofighi, G. Rinke, S. Baier, A. Ewinger, A. Urban, A. Wenka, S. Heideker, A. Jahn, R. Dittmeyer and J.-D. Grunwaldt, A microfluidic device for the investigation of rapid gold nanoparticle formation in continuous turbulent flow, *J. Phys.: Conf. Ser.*, 2016, **712**, 012072.
69. A. Kölbl, M. Kraut and A. Wenka, Design parameter studies on cyclone type mixers, *Chem. Eng. J.*, 2011, **167**, 444-454.
70. J. Thiele, M. Windbergs, A. R. Abate, M. Trebbin, H. C. Shum, S. Förster and D. A. Weitz, Early development drug formulation on a chip: Fabrication of nanoparticles using a microfluidic spray dryer, *Lab chip*, 2011, **11**, 2362-2368.
71. L. Mazutis, J. Gilbert, W. L. Ung, D. A. Weitz, A. D. Griffiths and J. A. Heyman, Single-cell analysis and sorting using droplet-based microfluidics, *Nat. Protoc.*, 2013, **8**, 870-891.
72. G. H. Hofmann, Development of methods and devices for spatially and temporally resolved X-ray microscopy for characterization in heterogeneous catalysis, *Dissertation, Karlsruhe Institute of Technology*, 2015.

73. C. A. Schneider, W. S. Rasband and K. W. Eliceiri, NIH Image to ImageJ: 25 years of image analysis, *Nat. Methods*, 2012, **9**, 671-675.
74. O. Müller, M. Nachtegaal, J. Just, D. Luetzenkirchen-Hecht and R. Frahm, Quick-EXAFS setup at the SuperXAS beamline for in situ X-ray absorption spectroscopy with 10 ms time resolution, *J. Synchrotron Radiat.*, 2016, **23**, 260-266.
75. B. Ravel and M. Newville, ATHENA, ARTEMIS, HEPHAESTUS: data analysis for X-ray absorption spectroscopy using IFEFFIT, *J. Synchrotron Radiat.*, 2005, **12**, 537-541.
76. N. K. Chaki, H. Tsunoyama, Y. Negishi, H. Sakurai and T. Tsukuda, Effect of Ag-doping on the catalytic activity of polymer-stabilized Au clusters in aerobic oxidation of alcohol, *J. Phys. Chem. C*, 2007, **111**, 4885-4888.
77. N. Fairley, *CasaXPS Manual 2.3. 15: Introduction to XPS and AES*, Casa Software, 2009.
78. Y. Wang and C. Wöll, IR spectroscopic investigations of chemical and photochemical reactions on metal oxides: bridging the materials gap, *Chem. Soc. Rev.*, 2017, **46**, 1875-1932.
79. J. Ftouni, M. Penhoat, A. Addad, E. Payen, C. Rolando and J.-S. Girardon, Highly controlled synthesis of nanometric gold particles by citrate reduction using the short mixing, heating and quenching times achievable in a microfluidic device, *Nanoscale*, 2012, **4**, 4450-4454.
80. S. Wang, Y. Zhao, J. Huang, Y. Wang, F. Kong, S. Wu, S. Zhang and W. Huang, Preparation and CO gas-sensing behavior of Au-doped SnO_2 sensors, *Vacuum*, 2006, **81**, 394-397.
81. N. Tahmasebi and S. M. Mahdavi, Synthesis and optical properties of Au decorated colloidal tungsten oxide nanoparticles, *Appl. Surf. Sci.*, 2015, **355**, 884-890.
82. L. Abahmane, A. Knauer, J. M. Köhler and G. A. Groß, Synthesis of polypyridine derivatives using alumina supported gold nanoparticles under micro continuous flow conditions, *Chem. Eng. J.*, 2011, **167**, 519-526.
83. X.-Q. Deng, B. Zhu, X.-S. Li, J.-L. Liu, X. Zhu and A.-M. Zhu, Visible-light photocatalytic oxidation of CO over plasmonic Au/TiO_2: Unusual features of oxygen plasma activation, *Appl. Catal. B: Environ.*, 2016, **188**, 48-55.
84. F. Xu, Y. Yao, D. Bai, R. Xu, J. Mei, D. Wu, Z. Gao and K. Jiang, A significant cathodic shift in the onset potential and enhanced photoelectrochemical water splitting using Au nanoparticles decorated WO_3 nanorod array, *J. Colloid Interface Sci.*, 2015, **458**, 194-199.
85. M. Azubel, J. Koivisto, S. Malola, D. Bushnell, G. L. Hura, A. L. Koh, H. Tsunoyama, T. Tsukuda, M. Pettersson and H. Häkkinen, Electron microscopy of gold nanoparticles at atomic resolution, *Science*, 2014, **345**, 909-912.
86. I. Ojea-Jiménez, F. M. Romero, N. G. Bastús and V. Puntes, Small gold nanoparticles synthesized with sodium citrate and heavy water: insights into the reaction mechanism, *J. Phys. Chem. C*, 2010, **114**, 1800-1804.
87. J. Tschopp, E. R. Podack and H. J. Müller-Eberhard, Ultrastructure of the membrane attack complex of complement: detection of the tetramolecular C9-polymerizing complex C5b-8, *Proc. Natl. Acad. Sci.*, 1982, **79**, 7474-7478.
88. M. Brust, M. Walker, D. Bethell, D. J. Schiffrin and R. Whyman, Synthesis of thiol-derivatised gold nanoparticles in a two-phase liquid–liquid system, *J. Chem. Soc., Chem. Commun.*, 1994, 801-802.
89. J. Wilcoxon, R. Williamson and R. Baughman, Optical properties of gold colloids formed in inverse micelles, *J. Chem. Phys.*, 1993, **98**, 9933-9950.

90. D. G. Duff, A. Baiker and P. P. Edwards, A new hydrosol of gold clusters, *J. Chem. Soc., Chem. Commun.*, 1993, 96-98.
91. D. G. Duff, A. Baiker and P. P. Edwards, A new hydrosol of gold clusters. 1. Formation and particle size variation, *Langmuir*, 1993, **9**, 2301-2309.
92. K. Sai Krishna, C. V. Navin, S. Biswas, V. Singh, K. Ham, G. L. Bovenkamp, C. S. Theegala, J. T. Miller, J. J. Spivey and C. S. Kumar, Millifluidics for time-resolved mapping of the growth of gold nanostructures, *J. Am. Chem. Soc.*, 2013, **135**, 5450-5456.
93. R. Ishida, S. Hayashi, S. Yamazoe, K. Kato and T. Tsukuda, Hydrogen-mediated electron doping of gold clusters as revealed by in Situ X-ray and UV–vis absorption spectroscopy, *J. Phys. Chem. Lett.*, 2017, **8**, 2368-2372.
94. C. Liu, Recent developments in polymer MEMS, *Adv. Mater.*, 2007, **19**, 3783-3790.
95. C. Hu, S. Lin, W. Li, H. Sun, Y. Chen, C.-W. Chan, C.-H. Leung, D.-L. Ma, H. Wu and K. Ren, A one-step strategy for ultra-fast and low-cost mass production of plastic membrane microfluidic chips, *Lab Chip*, 2016, **16**, 3909-3918.
96. M. Trebbin, K. Krüger, D. DePonte, S. V. Roth, H. N. Chapman and S. Förster, Microfluidic liquid jet system with compatibility for atmospheric and high-vacuum conditions, *Lab Chip*, 2014, **14**, 1733-1745.
97. S. Watanabe, T. Hiratsuka, Y. Asahi, A. Tanaka, K. Mae and M. T. Miyahara, Flow synthesis of plasmonic gold nanoshells via a microreactor, *Part. Part. Syst. Charact.*, 2015, **32**, 234-242.
98. N. D. Loh, S. Sen, M. Bosman, S. F. Tan, J. Zhong, C. A. Nijhuis, P. Král, P. Matsudaira and U. Mirsaidov, Multi-step nucleation of nanocrystals in aqueous solution, *Nat. Chem.*, 2016, **9**,77-82.
99. J. L. Hueso, V. Sebastián, Á. Mayoral, L. Usón, M. Arruebo and J. Santamaría, Beyond gold: rediscovering tetrakis-(hydroxymethyl)-phosphonium chloride (THPC) as an effective agent for the synthesis of ultra-small noble metal nanoparticles and Pt-containing nanoalloys, *RSC Adv.*, 2013, **3**, 10427-10433.
100. K. Schubert, J. Brandner, M. Fichtner, G. Linder, U. Schygulla and A. Wenka, Microstructure devices for applications in thermal and chemical process engineering, *Microscale Thermophys. Eng.*, 2001, **5**, 17-39.
101. C. Rands, B. Webb and D. Maynes, Characterization of transition to turbulence in microchannels, *Int. J. Heat Mass Tran.*, 2006, **49**, 2924-2930.
102. H. Tsunoyama, H. Sakurai, N. Ichikuni, Y. Negishi and T. Tsukuda, Colloidal gold nanoparticles as catalyst for carbon-carbon bond formation: application to aerobic homocoupling of phenylboronic acid in water, *Langmuir*, 2004, **20**, 11293-11296.
103. H. Tsunoyama, N. Ichikuni, H. Sakurai and T. Tsukuda, Effect of electronic structures of Au clusters stabilized by poly (N-vinyl-2-pyrrolidone) on aerobic oxidation catalysis, *J. Am. Chem. Soc.*, 2009, **131**, 7086-7093.
104. X. Zhang, L. Yu, J. Tie and X. Dong, Gas sensitivity and sensing mechanism studies on Au-doped TiO_2 nanotube arrays for detecting SF6 decomposed components, *Sensors*, 2014, **14**, 19517-19532.
105. M. Chen, Y. Cai, Z. Yan, K. Gath, S. Axnanda and D. W. Goodman, Highly active surfaces for CO oxidation on Rh, Pd, and Pt, *Surf. Sci.*, 2007, **601**, 5326-5331.
106. M. J. Hossain, H. Tsunoyama, M. Yamauchi, N. Ichikuni and T. Tsukuda, High-yield synthesis of PVP-stabilized small Pt clusters by microfluidic method, *Catal. Today*, 2012, **183**, 101-107.
107. Y. Zhang, X. Cui, F. Shi and Y. Deng, Nano-gold catalysis in fine chemical synthesis, *Chem. Rev*, 2012, **112**, 2467-2505.

108. D. Degler, H. W. P. de Carvalho, U. Weimar, N. Barsan, D. Pham, L. Maedler and J.-D. Grunwaldt, Structure–function relationships of conventionally and flame made Pd-doped sensors studied by X-ray absorption spectroscopy and DC-resistance, *Sens. Actuators B*, 2015, **219**, 315-323.
109. D. Degler, H. W. P. de Carvalho, K. Kvashnina, J.-D. Grunwaldt, U. Weimar and N. Barsan, Structure and chemistry of surface-doped Pt: SnO_2 gas sensing materials, *RSC Adv.*, 2016, **6**, 28149-28155.
110. D. Degler, S. Rank, S. Mueller, H. W. Pereira de Carvalho, J.-D. Grunwaldt, U. Weimar and N. Barsan, Gold-loaded tin dioxide gas sensing materials: Mechanistic insights and the role of gold dispersion, *ACS Sens.*, 2016, **1**, 1322-1329.
111. M. A. El-Sayed, Some interesting properties of metals confined in time and nanometer space of different shapes, *Acc. Chem. Res.*, 2001, **34**, 257-264.
112. A. N. Shipway, E. Katz and I. Willner, Nanoparticle arrays on surfaces for electronic, optical, and sensor applications, *ChemPhysChem*, 2000, **1**, 18-52.
113. S. Paul, C. Pearson, A. Molloy, M. Cousins, M. Green, S. Kolliopoulou, P. Dimitrakis, P. Normand, D. Tsoukalas and M. Petty, Langmuir−Blodgett film deposition of metallic nanoparticles and their application to electronic memory structures, *Nano Lett.*, 2003, **3**, 533-536.
114. M.-C. Daniel and D. Astruc, Gold nanoparticles: assembly, supramolecular chemistry, quantum-size-related properties, and applications toward biology, catalysis, and nanotechnology, *Chem. Rev.*, 2004, **104**, 293-346.
115. P. K. Jain, K. S. Lee, I. H. El-Sayed and M. A. El-Sayed, Calculated absorption and scattering properties of gold nanoparticles of different size, shape, and composition: applications in biological imaging and biomedicine, *J. Phys. Chem. B*, 2006, **110**, 7238-7248.
116. P. K. Jain, I. H. El-Sayed and M. A. El-Sayed, Au nanoparticles target cancer, *Nano Today*, 2007, **2**, 18-29.
117. N. Hayashi, Y. Sakai, H. Tsunoyama and A. Nakajima, Development of ultrafine multichannel microfluidic mixer for synthesis of bimetallic nanoclusters: catalytic application of highly monodisperse AuPd nanoclusters stabilized by poly (N-vinylpyrrolidone), *Langmuir*, 2014, **30**, 10539-10547.
118. F. Liu, D. Wechsler and P. Zhang, Alloy-structure-dependent electronic behavior and surface properties of Au–Pd nanoparticles, *Chem. Phys. Lett.*, 2008, **461**, 254-259.
119. A. Knauer, A. Eisenhardt, S. Krischok and J. M. Koehler, Nanometer precise adjustment of the silver shell thickness during automated Au–Ag core–shell nanoparticle synthesis in micro fluid segment sequences, *Nanoscale*, 2014, **6**, 5230-5238.
120. J. K. Edwards, S. J. Freakley, A. F. Carley, C. J. Kiely and G. J. Hutchings, Strategies for designing supported gold–palladium bimetallic catalysts for the direct synthesis of hydrogen peroxide, *Acc. Chem. Res.*, 2013, **47**, 845-854.
121. J. K. Edwards, B. Solsona, E. Ntainjua, A. F. Carley, A. A. Herzing, C. J. Kiely and G. J. Hutchings, Switching off hydrogen peroxide hydrogenation in the direct synthesis process, *Science*, 2009, **323**, 1037-1041.
122. J. K. Edwards, B. E. Solsona, P. Landon, A. F. Carley, A. Herzing, C. J. Kiely and G. J. Hutchings, Direct synthesis of hydrogen peroxide from H_2 and O_2 using TiO_2-supported Au–Pd catalysts, *J. Catal.*, 2005, **236**, 69-79.
123. N. Dimitratos, J. A. Lopez-Sanchez and G. J. Hutchings, Selective liquid phase oxidation with supported metal nanoparticles, *Chem. Sci.*, 2012, **3**, 20-44.

124. M. B. Griffin, A. A. Rodriguez, M. M. Montemore, J. R. Monnier, C. T. Williams and J. W. Medlin, The selective oxidation of ethylene glycol and 1, 2-propanediol on Au, Pd, and Au–Pd bimetallic catalysts, *J. Catal.*, 2013, **307**, 111-120.
125. S. E. Davis, M. S. Ide and R. J. Davis, Selective oxidation of alcohols and aldehydes over supported metal nanoparticles, *Green Chem.*, 2013, **15**, 17-45.
126. L. Kesavan, R. Tiruvalam, M. H. Ab Rahim, M. I. bin Saiman, D. I. Enache, R. L. Jenkins, N. Dimitratos, J. A. Lopez-Sanchez, S. H. Taylor and D. W. Knight, Solvent-free oxidation of primary carbon-hydrogen bonds in toluene using Au-Pd alloy nanoparticles, *Science*, 2011, **331**, 195-199.
127. L. Guczi, A. Beck, A. Horváth, Z. Koppány, G. Stefler, K. Frey, I. Sajó, O. Geszti, D. Bazin and J. Lynch, AuPd bimetallic nanoparticles on TiO_2: XRD, TEM, in situ EXAFS studies and catalytic activity in CO oxidation, *J. Mol. Catal. A: Chem.*, 2003, **204–205**, 545-552.
128. K. Qian and W. Huang, Au–Pd alloying-promoted thermal decomposition of PdO supported on SiO_2 and its effect on the catalytic performance in CO oxidation, *Catal. Today*, 2011, **164**, 320-324.
129. J. Xu, T. White, P. Li, C. He, J. Yu, W. Yuan and Y.-F. Han, Biphasic Pd− Au alloy catalyst for low-temperature CO oxidation, *J. Am. Chem. Soc.*, 2010, **132**, 10398-10406.
130. S.-C. Tsen, P. Crozier and J. Liu, Lattice measurement and alloy compositions in metal and bimetallic nanoparticles, *Ultramicroscopy*, 2003, **98**, 63-72.
131. S. Marx and A. Baiker, Beneficial interaction of gold and palladium in bimetallic catalysts for the selective oxidation of benzyl alcohol, *J. Phys. Chem. C*, 2009, **113**, 6191-6201.
132. G. Tofighi, A. Gaur, D. E. Doronkin, H. Lichtenberg, W. Wang, D. Wang, G. Rinke, A. Ewinger, R. Dittmeyer and J.-D. Grunwaldt, Microfluidic synthesis of ultrasmall AuPd nanoparticles with a homogeneously mixed alloy structure in fast continuous flow for catalytic applications, *J. Phys. Chem. C*, 2018, **122**, 1721-1731.
133. A. M. Karim, N. Al Hasan, S. Ivanov, S. Siefert, R. T. Kelly, N. G. Hallfors, A. Benavidez, L. Kovarik, A. Jenkins and R. E. Winans, Synthesis of 1 nm Pd nanoparticles in a microfluidic reactor: Insights from in situ X-ray absorption fine structure spectroscopy and small-angle X-ray scattering, *J. Phys. Chem. C*, 2015, **119**, 13257-13267.
134. A. Maeland and T. B. Flanagan, Lattice spacings of gold–palladium alloys, *Can. J. Phys.*, 1964, **42**, 2364-2366.
135. H. King and F. Manchester, A low-temperature X-ray diffraction study of Pd and some Pd-H alloys, *J. Phys. F: Met. Phys.*, 1978, **8**, 15.
136. C. Kuhrt and M. Harsdorff, Photoemission and electron microscopy of small supported palladium clusters, *Surf. Sci.*, 1991, **245**, 173-179.
137. D. R. Kumar, B. Prasad and A. Kulkarni, Segmented flow synthesis of Ag nanoparticles in spiral microreactor: role of continuous and dispersed phase, *Chem. Eng. J.*, 2012, **192**, 357-368.
138. O. Lopez-Acevedo, H. Tsunoyama, T. Tsukuda and C. M. Aikens, Chirality and electronic structure of the thiolate-protected Au_{38} nanocluster, *J. Am. Chem. Soc.*, 2010, **132**, 8210-8218.
139. M. Zhu, C. M. Aikens, F. J. Hollander, G. C. Schatz and R. Jin, Correlating the crystal structure of a thiol-protected Au_{25} cluster and optical properties, *J. Am. Chem. Soc.*, 2008, **130**, 5883-5885.
140. T. Iwasa and K. Nobusada, Gold-thiolate core-in-cage cluster $Au_{25}(SCH_3)_{18}$ shows localized spins in charged states, *Chem. Phys. Lett.*, 2007, **441**, 268-272.

141. F. Krumeich, S. Marx, A. Baiker and R. Nesper, Characterization of AuPd nanoparticles by probe-corrected scanning transmission electron microscopy and X-ray absorption spectroscopy, *Z. Anorg. Allg. Chem.*, 2011, **637**, 875-881.
142. X. Teng, Q. Wang, P. Liu, W. Han, A. I. Frenkel, W. Wen, N. Marinkovic, J. C. Hanson and J. A. Rodriguez, Formation of Pd/Au nanostructures from Pd nanowires via galvanic replacement reaction, *J. Am. Chem. Soc.*, 2008, **130**, 1093-1101.
143. J. Kaiser, W. Szczerba, H. Riesemeier, U. Reinholz, M. Radtke, M. Albrecht, Y. Lu and M. Ballauff, The structure of AuPd nanoalloys anchored on spherical polyelectrolyte brushes determined by X-ray absorption spectroscopy, *Faraday Discuss.*, 2013, **162**, 45-55.
144. E. K. Gibson, A. M. Beale, C. R. A. Catlow, A. Chutia, D. Gianolio, A. Gould, A. Kroner, K. M. Mohammed, M. Perdjon and S. M. Rogers, Restructuring of AuPd nanoparticles studied by a combined XAFS/DRIFTS approach, *Chem. Mater.*, 2015, **27**, 3714-3720.
145. T. Ishida, H. Koga, M. Okumura and M. Haruta, Advances in gold catalysis and understanding the catalytic mechanism, *Chem. Rec.*, 2016, **16**, 2278-2293.
146. F. Gao, Y. Wang and D. W. Goodman, CO oxidation over AuPd (100) from ultrahigh vacuum to near-atmospheric pressures: CO adsorption-induced surface segregation and reaction kinetics, *J. Phys. Chem. C*, 2009, **113**, 14993-15000.
147. T. V. Janssens, A. Carlsson, A. Puig-Molina and B. S. Clausen, Relation between nanoscale Au particle structure and activity for CO oxidation on supported gold catalysts, *J. Catal.*, 2006, **240**, 108-113.
148. I. X. Green, W. Tang, M. Neurock and J. T. Yates, Spectroscopic observation of dual catalytic sites during oxidation of CO on a Au/TiO_2 catalyst, *Science*, 2011, **333**, 736-739.
149. F. Gao, Y. Wang and D. W. Goodman, CO oxidation over AuPd (100) from ultrahigh vacuum to near-atmospheric pressures: the critical role of contiguous Pd atoms, *J. Am. Chem. Soc.*, 2009, **131**, 5734-5735.
150. T. Engel and G. Ertl, Elementary steps in the catalytic oxidation of carbon monoxide on platinum metals, *Adv. Catal.*, 1979, **28**, 1-78.
151. J. Kim, E. Samano and B. E. Koel, CO adsorption and reaction on clean and oxygen-covered Au (211) surfaces, *J. Phys. Chem. B*, 2006, **110**, 17512-17517.
152. M. Chen and D. Goodman, The structure of catalytically active gold on titania, *Science*, 2004, **306**, 252-255.
153. F. Gao, S. McClure, Y. Cai, K. Gath, Y. Wang, M. Chen, Q. Guo and D. Goodman, CO oxidation trends on Pt-group metals from ultrahigh vacuum to near atmospheric pressures: A combined in situ PM-IRAS and reaction kinetics study, *Surf. Sci.*, 2009, **603**, 65-70.
154. F. Gao, Y. Wang, Y. Cai and D. Goodman, CO oxidation on Pt-group metals from ultrahigh vacuum to near atmospheric pressures. 2. Palladium and platinum, *J. Phys. Chem. C*, 2008, **113**, 174-181.
155. R. Arrigo, M. E. Schuster, S. Abate, S. Wrabetz, K. Amakawa, D. Teschner, M. Freni, G. Centi, S. Perathoner and M. Hävecker, Dynamics of palladium on nanocarbon in the direct synthesis of H_2O_2, *ChemSusChem*, 2014, **7**, 179-194.
156. H.-F. Wang, W. E. Kaden, R. Dowler, M. Sterrer and H.-J. Freund, Model oxide-supported metal catalysts–comparison of ultrahigh vacuum and solution based preparation of Pd nanoparticles on a single-crystalline oxide substrate, *Phys. Chem. Chem. Phys.*, 2012, **14**, 11525-11533.
157. D. Zemlyanov, B. Aszalos-Kiss, E. Kleimenov, D. Teschner, S. Zafeiratos, M. Hävecker, A. Knop-Gericke, R. Schlögl, H. Gabasch and W. Unterberger, In situ

XPS study of Pd (111) oxidation. Part 1: 2D oxide formation in 10− 3 mbar O_2, *Surf. Sci.*, 2006, **600**, 983-994.
158. M. Buchholz, X. Yu, C. Yang, S. Heißler, A. Nefedov, Y. Wang and C. Wöll, IR-spectroscopy of CO adsorption on mixed-terminated ZnO surfaces, *Surf. Sci.*, 2016, **652**, 247-252.
159. E. K. Hanrieder, A. Jentys and J. A. Lercher, Atomistic engineering of catalyst precursors: dynamic reordering of PdAu nanoparticles during vinyl acetate synthesis enhanced by potassium acetate, *ACS Catal.*, 2015, **5**, 5776-5786.
160. W. K. Kuhn, J. Szanyi and D. W. Goodman, CO adsorption on Pd(111): the effects of temperature and pressure, *Surf. Sci.*, 1992, **274**, L611-L618.
161. R. Eischens, S. Francis and W. Pliskin, The Effect of surface coverage on the spectra of chemisorbed CO, *J. Phys. Chem.*, 1956, **60**, 194-201.
162. M. A. Vannice and S. Wang, Determination of IR extinction coefficients for linear- and bridged-bonded carbon monoxide on supported palladium, *J. Phys. Chem.*, 1981, **85**, 2543-2546.
163. C. Yang, X. Yu, S. Heißler, A. Nefedov, S. Colussi, J. Llorca, A. Trovarelli, Y. Wang and C. Wöll, Surface faceting and reconstruction of ceria nanoparticles, *Angew. Chem. Int. Ed.*, 2017, **56**, 375-379.
164. J.-D. Grunwaldt, M. Maciejewski, O. S. Becker, P. Fabrizioli and A. Baiker, Comparative study of Au/TiO_2 and Au/ZrO_2 catalysts for low-temperature CO oxidation, *J. Catal.*, 1999, **186**, 458-469.
165. F. Boccuzzi, A. Chiorino and M. Manzoli, FTIR study of the electronic effects of CO adsorbed on gold nanoparticles supported on titania, *Surf. Sci.*, 2000, **454**, 942-946.
166. H. Hartshorn, C. J. Pursell and B. D. Chandler, Adsorption of CO on supported gold nanoparticle catalysts: a comparative study. *J. Phys. Chem. C*, 2009, **113** (24), 10718-10725.
167. M. Xu, H. Noei, K. Fink, M. Muhler, Y. Wang and C. Wöll, The surface science approach for understanding reactions on oxide powders: the importance of IR spectroscopy, *Angew. Chem. Int. Ed.*, 2012, **51**, 4731-4734.
168. H. L. Abbott, A. Aumer, Y. Lei, C. Asokan, R. J. Meyer, M. Sterrer, S. Shaikhutdinov and H.-J. Freund, CO adsorption on monometallic and bimetallic Au− Pd nanoparticles supported on oxide thin films, *J. Phys. Chem. C*, 2010, **114**, 17099-17104.
169. A. Crossley and D. A. King, Infrared spectra for co isotopes chemisorbed on Pt "111": Evidence for strong absorbate coupling interactions, *Surf. Sci.*, 1977, **68**, 528-538.
170. B. Persson and R. Ryberg, Vibrational interaction between molecules adsorbed on a metal surface: The dipole-dipole interaction, *Phys. Rev. B*, 1981, **24**, 6954.
171. J. RODRIGUEZ and D. W. Goodman, The nature of the metal-metal bond in bimetallic surfaces, *Science*, 1992, **257**, 897-903.
172. J. Rodriguez, Physical and chemical properties of bimetallic surfaces, *Surf. Sci. Rep.*, 1996, **24**, 223-287.
173. F. Gao and D. W. Goodman, Pd–Au bimetallic catalysts: understanding alloy effects from planar models and (supported) nanoparticles, *Chem. Soc. Rev.*, 2012, **41**, 8009-8020.
174. X. Weng, X. Yuan, H. Li, X. Li, M. Chen and H. Wan, The study of the active surface for CO oxidation over supported Pd catalysts, *Sci. China Chem.*, 2015, **58**, 174-179.

175. A. Gurlo, Interplay between O_2 and SnO_2: oxygen ionosorption and spectroscopic evidence for adsorbed oxygen, *ChemPhysChem*, 2006, **7**, 2041-2052.
176. R. Jaaniso and O. K. Tan, *Semiconductor gas sensors*, Elsevier, 2013.
177. S. Wang, J. Huang, Y. Zhao, S. Wang, X. Wang, T. Zhang, S. Wu, S. Zhang and W. Huang, Preparation, characterization and catalytic behavior of SnO_2 supported Au catalysts for low-temperature CO oxidation, *J. Mol. Catal. A: Chem.*, 2006, **259**, 245-252.
178. S. Wang, J. Huang, Y. Zhao, S. Wang, S. Wu, S. Zhang and W. Huang, Nanostructure SnO_2 and supported Au catalysts: Synthesis, characterization, and catalytic oxidation of CO, *Mater. Lett.*, 2006, **60**, 1706-1709.
179. A. Cabot, A. Dieguez, A. Romano-Rodrıguez, J. Morante and N. Barsan, Influence of the catalytic introduction procedure on the nano-SnO_2 gas sensor performances: Where and how stay the catalytic atoms?, *Sens. Actuators B*, 2001, **79**, 98-106.
180. A. Dieguez, A. Vila, A. Cabot, A. Romano-Rodrıguez, J. Morante, J. Kappler, N. Barsan, U. Weimar and W. Göpel, Influence on the gas sensor performances of the metal chemical states introduced by impregnation of calcinated SnO_2 sol–gel nanocrystals, *Sens. Actuators B*, 2000, **68**, 94-99.
181. K. Großmann, S. Wicker, U. Weimar and N. Barsan, Impact of Pt additives on the surface reactions between SnO_2, water vapour, CO and H_2; an operando investigation, *Phys. Chem. Chem.Phys.*, 2013, **15**, 19151-19158.
182. N. Yamazoe, New approaches for improving semiconductor gas sensors, *Sens. Actuators B*, 1991, **5**, 7-19.
183. N. Yamazoe, Y. Kurokawa and T. Seiyama, Effects of additives on semiconductor gas sensors, *Sens. Actuators B*, 1983, **4**, 283-289.
184. E. Ogel, S. A. Müller, A. Sackmann, F. Gyger, P. Bockstaller, E. Brose, M. Casapu, L. Schöttner, D. Gerthsen and C. Feldmann, Comparison of the catalytic performance and carbon monoxide sensing behavior of Pd-SnO_2 core@shell nanocomposites, *ChemCatChem*, 2017, **9**, 407-413.
185. D. Koziej, M. Hübner, N. Barsan, U. Weimar, M. Sikora and J.-D. Grunwaldt, Operando X-ray absorption spectroscopy studies on Pd-SnO_2 based sensors, *Phys. Chem. Chem. Phys.*, 2009, **11**, 8620-8625.
186. J.-D. Grunwaldt, N. van Vegten and A. Baiker, Insight into the structure of supported palladium catalysts during the total oxidation of methane, *Chem. Commun.*, 2007, 4635-4637.
187. N. Barsan and U. Weimar, Understanding the fundamental principles of metal oxide based gas sensors; the example of CO sensing with SnO_2 sensors in the presence of humidity, *J. Phys.: Condens. Matter*, 2003, **15**, R813.
188. M. Hübner, D. Koziej, J.-D. Grunwaldt, U. Weimar and N. Barsan, An Au clusters related spill-over sensitization mechanism in SnO_2-based gas sensors identified by operando HERFD-XAS, work function changes, DC resistance and catalytic conversion studies, *Phys. Chem. Chem. Phys.*, 2012, **14**, 13249-13254.
189. S. Vukojević, O. Trapp, J. D. Grunwaldt, C. Kiener and F. Schüth, Quasi-homogeneous methanol synthesis over highly active copper nanoparticles, *Angew. Chem.*, 2005, **117**, 8192-8195.
190. Q.-C. Zhang, Z.-W. Liu, X.-H. Zhu, L.-X. Wen, Q.-F. Zhu, K. Guo and J.-F. Chen, Application of microimpinging stream reactors in the preparation of $CuO/ZnO/Al_2O_3$ catalysts for methanol synthesis, *Ind. Eng. Chem. Res.*, 2015, **54**, 8874-8882.

191. J. Schumann, T. Lunkenbein, A. Tarasov, N. Thomas, R. Schlögl and M. Behrens, Synthesis and characterisation of a highly active Cu/ZnO: Al catalyst, *ChemCatChem*, 2014, **6**, 2889-2897.
192. T. Lunkenbein, J. Schumann, M. Behrens, R. Schlögl and M. G. Willinger, Formation of a ZnO overlayer in industrial $Cu/ZnO/Al_2O_3$ catalysts induced by strong metal–support interactions, *Angew. Chem.*, 2015, **127**, 4627-4631.
193. B. L. Kniep, T. Ressler, A. Rabis, F. Girgsdies, M. Baenitz, F. Steglich and R. Schlögl, Rational design of nanostructured copper–zinc oxide catalysts for the steam reforming of methanol, *Angew. Chem. Int. Ed.*, 2004, **43**, 112-115.
194. Y. Zhang, Q. Sun, J. Deng, D. Wu and S. Chen, A high activity $Cu/ZnO/Al_2O_3$ catalyst for methanol synthesis: Preparation and catalytic properties, *Appl. Catal. A: Gen.*, 1997, **158**, 105-120.
195. Z. Chu, H. Chen, Y. Yu, Q. Wang and D. Fang, Surfactant-assisted preparation of $Cu/ZnO/Al_2O_3$ catalyst for methanol synthesis from syngas, *J. Mol. Catal. A: Chem.*, 2013, **366**, 48-53.
196. M. M. Günter, B. Bems, R. Schlöegl and T. Ressler, In situ studies on the structure of copper oxide/zinc oxide catalysts, *J. Synchrotron Radiat.*, 2001, **8**, 619-621.
197. M. Behrens, F. Studt, I. Kasatkin, S. Kühl, M. Hävecker, F. Abild-Pedersen, S. Zander, F. Girgsdies, P. Kurr and B.-L. Kniep, The active site of methanol synthesis over $Cu/ZnO/Al_2O_3$ industrial catalysts, *Science*, 2012, **336**, 893-897.
198. Q.-C. Zhang, K.-P. Cheng, L.-X. Wen, K. Guo and J.-F. Chen, A study on the precipitating and aging processes of $CuO/ZnO/Al_2O_3$ catalysts synthesized in micro-impinging stream reactors, *RSC Adv.*, 2016, **6**, 33611-33621.
199. L. Angelo, M. Girleanu, O. Ersen, C. Serra, K. Parkhomenko and A.-C. Roger, Catalyst synthesis by continuous coprecipitation under micro-fluidic conditions: Application to the preparation of catalysts for methanol synthesis from CO_2/H_2, *Catal. Today*, 2016, **270**, 59-67.
200. M. Schur, B. Bems, A. Dassenoy, I. Kassatkine, J. Urban, H. Wilmes, O. Hinrichsen, M. Muhler and R. Schlögl, Continuous coprecipitation of catalysts in a micromixer: Nanostructured Cu/ZnO composite for the synthesis of methanol, *Angew. Chem. Int. Ed.*, 2003, **42**, 3815-3817.
201. B. Zhang and N. Yan, Towards rational design of nanoparticle catalysis in ionic liquids, *Catalysts*, 2013, **3**, 543-562.
202. B. Bems, M. Schur, A. Dassenoy, H. Junkes, D. Herein and R. Schlögl, Relations between synthesis and microstructural properties of copper/zinc hydroxycarbonates, *Chem. Eur. J.*, 2003, **9**, 2039-2052.
203. Z. Li, S. Yan and H. Fan, Enhancement of stability and activity of $Cu/ZnO/Al_2O_3$ catalysts by microwave irradiation for liquid phase methanol synthesis, *Fuel*, 2013, **106**, 178-186.
204. P. Gao, F. Li, F. Xiao, N. Zhao, W. Wei, L. Zhong and Y. Sun, Effect of hydrotalcite-containing precursors on the performance of Cu/Zn/Al/Zr catalysts for CO_2 hydrogenation: Introduction of Cu^{2+} at different formation stages of precursors, *Catal. Today*, 2012, **194**, 9-15.

Acknowledgements

This work would not have been possible without the support of my advisors, colleagues and friends to whom I would like to express my sincere gratitude.

First of all, I am grateful to my supervisor Prof. Dr. Jan-Dierk Grunwaldt for offering me a PhD position in his team along with a fascinating and highly relevant research topic. I also thank him for his constant support and valuable advice during the last three years while giving me freedom for independent self-motivated research endeavors. I could not have imagined having a better advisor and mentor for my PhD study.

Furthermore, I wish to cordially thank Dr. Henning Lichtenberg for his continuous help during my PhD study and related research, his patience, motivation, and immense knowledge. His guidance helped me in all the time of research and writing of this thesis.

My sincere thanks also goes to Dr. Dmitry Doronkin for sharing his expertise especially in catalysis with me. Dr. Abhijeet Gaur is acknowledged for contributing to this work with respect to XAS data analysis. Without Jan Pesek building up and operating the microfluidic setup used in this work would not have been possible. I also would like to show my gratitude to Dr. Sabrina Müller for her support during experiments at the beamline and also for the gas sensing project, Dr. Gülperi Cavusoglu for technical support during XRD measurements and Angela Beilmann for BET measurements and analysis.

Many thanks to the members of the X-ray Microscopy team in our group, Dr. Thomas Sheppard, Dr. Sina Baier, Dr. Federico Benzi and especially Dr. Georg Hofmann for providing a solid basis for my thesis work and giving his detailed and helpful answers to my many questions. I thank my fellow office mates Elen Ogel and Yakub Fam for the stimulating discussions and for their company during the sleepless nights before deadlines.

Furthermore, I sincerely appreciate the fruitful collaboration with the following scientists outside our research group:

- Dr. Günter Rinke, Dr. Angela Ewinger and Prof. Dr. Roland Dittmeyer (KIT-IMVT) for contributing expertise in the field of microreactor technology
- Wu Wang (KIT-INT) for excellent electron microscopic images
- Dr. Yuemin Wang, Xiaojuan Yu, Ludger Schöttner and Prof. Dr. Christof Wöll (KIT-IFG) for top quality UHV-FTIR and XPS data

- Dr. Stephan Pitter, Dr. Karla Herrera Delgado, Sabrina Polierer and Simon Wodarz (KIT-IKFT) for catalytic testing of the methanol catalysts
- Sheng Wang and PD Dr. Silke Behrens (KIT-IKFT) for showing me future perspectives for applications of the nanomaterials produced during this thesis work
- Dr. Nicolae Barsan, Dr. David Degler and Benjamin Junker (University of Tübingen) for introducing me to the world of chemical sensing
- Dr. Thomas Bergfeldt (KIT-IAM & KNMF) for precious ICP-OES measurements
- The beamline scientists at synchrotron light sources Dr. Maarten Nachtegaal (SLS), Dr. Stefan Mangold, Dr. Anna Zimina, Dr. Tim Prüßmann (ANKA), Dr. Roman Chernikov and Dr. Vadim Murzin (DESY) for technical support during beamtimes
- Dr. Andreas Jahn (TUD-IHM) and Dr. Steffen Howitz (GeSiM) for constructing the microfluidic chips
- Dr. Maria Casapu and Angela Beilmann for analyzing my samples using a thermogravimetry apparatus (DFG grant no. INST 121384/70-1).

Special thanks to Mohammad Vakili (University of Hamburg) for valuable advice on hydrophobic channel coating with Ombrello, and to Dr. Michael Hirtz (KIT-INT) for his support regarding functionalization of microchannel walls.

It also means a lot to me that my former colleagues and dear friends from TU Chemnitz, Saeed Jafarpour, Prof. Raul D. Rodriguez and Dr. Falko Seidel stayed in contact and inspiring me scientifically and personally.

The Virtual Institute VI-403 "*In-situ* Nano Imaging of Biological and Chemical Processes", the Helmholtz research programs "Storage and Cross-linked Infrastructures" (SCI) and "Science and Technology of Nanosystems" (STN) along with the BMBF projects "X-ray microscopy" (05K10VK1) and "Nanoscopy" (05K13VK2) as well as KIT are gratefully acknowledged for financial support. I furthermore wish to thank the KIT synchrotron, PETRA III (DESY) and the Swiss Light Source (SLS) for providing beamtime.

Many thanks also to the Helmholtz Research School "Energy Related Catalysis", especially Dr. Steffen Tischer, for organizing a number of courses, summer and winter schools, which helped me to develop further, acquire new skills and extend my collaboration network.

Last but not least, a big Merci to my family, especially my parents and my sister for being a guiding light in my life. Without you I could not have come so far.

Scientific Contributions

Publications related to this thesis:

A Microfluidic Device for the Investigation of Rapid Gold Nanoparticle Formation in Continuous Turbulent Flow
G. Hofmann, G. Tofighi, G. Rinke, S. Baier, A. Ewinger, A. Urban, A. Wenka, S. Heideker, A. Jahn, R. Dittmeyer and J.-D. Grunwaldt
Journal of Physics: Conference Series, 2016, **712**, 012072.

Continuous Microfluidic Synthesis of Colloidal Ultrasmall Gold Nanoparticles: *In situ* Study of the Early Reaction Stages and Application for Catalysis
G. Tofighi, H. Lichtenberg, J. Pesek, T. L. Sheppard, W. Wang, L. Schöttner, G. Rinke, R. Dittmeyer and J.–D. Grunwaldt
Reaction Chemistry & Engineering, 2017, **2**, 876-884.
Results from this publication are presented in chapter 2 & 3; reprinted with permission from The Royal Society of Chemistry.

Microfluidic Synthesis of Ultrasmall AuPd Nanoparticles with a Homogeneously Mixed Alloy structure in Fast Continuous Flow for Catalytic Applications
G. Tofighi, A. Gaur, D. E. Doronkin, H. Lichtenberg, W. Wang, D. Wang, G. Rinke, A. Ewinger, R. Dittmeyer and J.-D. Grunwaldt
Journal of Physical Chemistry C, 2018, **122**, 1721-1731.
Results from this publication are presented in chapter 4; reprinted with permission from American Chemical Society.

Chemical Nature of Microfluidically Synthesized AuPd Nanoalloys Supported on TiO_2
G. Tofighi, X.Yu, H. Lichtenberg, D. E. Doronkin, W. Wang, C. Wöll, Y. Wang, and J.-D. Grunwaldt (submitted)
Results from this upcoming publication are presented in chapter 5.

Microfluidically Synthesized Au, Pd and AuPd Nanoparticles Supported on SnO_2 for Gas Sensing Application
G. Tofighi, D. Degler, B. Junker, S. Müller, H. Lichtenberg, W. Wang, U. Weimar, N. Barsan and J.-D. Grunwaldt (submitted)
Results from this upcoming publication are presented in chapter 5.

Microfluidic Synthesis of $Cu/ZnO/Al_2O_3$ NPs in a Co-precipitation Reaction for Methanol Synthesis
G. Tofighi et al. (in preparation)
Results from this upcoming publication are presented in chapter 6.

Poster presentation:

Investigation of Rapid Gold Nanoparticle Formation in Continuous Flow by XAS
G. Hofmann, G. Tofighi, G. Rinke, S. Baier, A. Ewinger, A. Urban, A.Wenka, S. Heideker, A. Jahn, R. Dittmeyer and J.-D. Grunwaldt
16th International Conference on X-ray Absorption Fine Structure (XAFS16)
23-28 August 2015
Karlsruhe, Germany

***In Situ* Studies of Gold Nanoparticle Formation in Microfluidic Reactors**
G. Tofighi, T. Sheppard, G. Hofmann, G. Rinke, R. Dittmeyer and J.-D. Grunwaldt
115th General Assembly of the German Bunsen Society for Physical Chemistry
5-7 May 2016
Rostock, Germany

Microfluidic Synthesis of Ultrasmall AuPd Nanoalloys in Continuous Turbulent Flow
G. Tofighi, A. Gaur, D. E. Doronkin, H. Lichtenberg, W. Wang, T. Sheppard, G.Rinke and J.-D. Grunwaldt
25th Annual Meeting of the German Crystallographic Society (DGK)
27-30. March 2017
Karlsruhe, Germany

***In situ* XAS at the Early Stages of Au Nanoparticle Formation in a Turbulent Microflow**
G. Tofighi, H. Lichtenberg, T. Sheppard, J. Pesek, G. Rinke, W. Wang, L. Schöttner and J.-D. Grunwaldt
13th European Congress on Catalysis (EUROPACAT 2017)
27-31 August 2017
Florence, Italy

Erklärung

Hiermit versichere ich, die vorliegende Doktorarbeit selbstständig angefertigt und keine anderen als die von mir angegebenen Quellen und Hilfsmittel verwendet, sowie wörtliche und sinngemäße Zitate als solche gekennzeichnet zu haben. Weiterhin habe ich die Satzung des Karlsruher Instituts für Technologie (KIT) zur Sicherung guter wissenschaftlicher Praxis in der gültigen Fassung beachtet. Die Arbeit wurde in gleicher oder anderer Form keiner anderen Prüfungsbehörde zur Erlangung eines akademischen Grades vorgelegt. Die elektronische Version der Arbeit stimmt mit der schriftlichen überein und die Primärdaten sind beim Institut gesichert.

Karlsruhe, den 1. Oktober 2017